NUMERICAL STUDY OF THE EFFECT OF SEISMIC IN-PLANE DAMAGE ON OUT-OF-PLANE PERFORMANCE OF UNREINFORCED MASONRY WALLS

MSc Thesis

TU Delft

NUMERICAL STUDY OF THE EFFECT OF SEISMIC IN-PLANE DAMAGE ON OUT-OF-PLANE PERFORMANCE OF UNREINFORCED MASONRY WALLS

MSc Thesis

By

Sudaya Sharma

In partial fulfilment of the requirements for the degree of

Master of Science in Structural Engineering,

At the Faculty of Civil Engineering and Geosciences,

Delft University of Technology

To be defended publicly on Tuesday August 22, 2023, at 11:30 AM

Student number: 4308875

Thesis committee members:

Prof.dr.ir. J.G. Rots	TU Delft, chairman
Prof.dr.ir. M.A.N. Hendriks	TU Delft, supervisor
Dr. F. Messali	TU Delft, supervisor
PhD student A. Ghezelbash	TU Delft, daily supervisor

TU Delft

Acknowledgements

This thesis is written to fulfil the requirements for my MSc Degree in Structural Engineering at the Delft University of Technology. I would like to express my sincere gratitude to everyone who has provided their support during this academic journey.

I would like to begin by expressing my deepest gratitude to Dr. Francesco Messali, my supervisor, for his invaluable assistance in identifying this interesting research topic. The discussions we had at the start of this thesis played a crucial role in setting me on the right path from the very beginning. Moreover, I extend my thanks for his continuous guidance, providing constructive feedback on my report, and offering valuable insights during our meetings throughout the entire thesis period.

I am extremely grateful to my daily supervisor, Amirhossein Ghezelbash, for his patient guidance during the thesis period. Your constant support, availability for questions, and encouragement during challenging times have been invaluable to me. I truly appreciate the time you dedicated to engaging in our lengthy discussions. Thank you for being an excellent mentor and providing me with the necessary assistance to complete this thesis successfully.

I extend my heartfelt appreciation to Prof. Jan Rots and Prof. Max Hendriks for their valuable advice and insightful comments during the committee meetings. These meetings were incredibly productive and inspiring, and I thoroughly enjoyed every minute of our engaging discussions. I am truly grateful for your contributions to my academic journey.

Lastly, I wish to express my gratitude to my family and friends for their support and encouragement throughout my study. Your presence during the challenging times has been a tremendous source of strength. Additionally, I extend my thanks to the committee members for their understanding of the circumstances.

Sudaya Sharma

Summary

Previous earthquake reports have highlighted the high vulnerability of masonry walls to failure when subjected to the out-of-plane (OOP) loading. Particularly, this OOP failure is a significant cause of collapse in unreinforced masonry (URM) buildings, especially those with slender walls and large openings. Moreover, in the past they were designed with minor regard to seismic design concepts. In Groningen, the Netherlands, where the majority of houses are constructed using unreinforced masonry, there have been frequent occurrences of low-intensity seismic activity, causing pre-damage to the walls. Typically, the walls get pre-damaged in the in-plane (IP) direction due to low-intensity shakes and settlements, since the box-like behaviour is established when the forces are low. Box-behaviour refers to the case where there is a strong connection between orthogonal walls and a stiff rigid floor diaphragm. As a consequence, the walls experience the desired IP shear failure during seismic loading. However, research regarding the OOP performance of pre-damaged URM walls is limited, and existing studies have shown that IP pre-damage decreases the ultimate OOP load-bearing capacity of the walls. To address this gap, this report aims to conduct a preliminary investigation on the OOP strength of pre-damaged URM walls, considering both walls without and with openings. Notably, there is no existing evidence in the literature regarding walls with openings on this specific topic. The primary research question can be stated as follows:

How does the in-plane pre-damage affect the out-of-plane load-bearing strength of URM walls?

This thesis employs a numerical modelling approach to address the research question. The software package DIANA 10.5 is used, adopting a simplified micro modelling method with shell elements to simulate the behaviour of masonry. Bricks are modelled with continuum shell elements, while the mortar joints are modelled using zero-thickness interface elements. Also, the potential vertical crack in the bricks is considered using the interface elements. The validation of the numerical modelling approach is performed in two steps. Firstly, the mechanical properties of the numerical model are calibrated using small-scale material tests. In the second step, the calibrated parameters are directly applied to the numerical monotonic analyses of full-scale walls, and the results are then compared to experimental test results. The calcium silicate (CS) brick masonry tests, from material to structural levels, conducted at the Delft University of Technology are selected as benchmarks for the calibration and validation of the numerical model. A good agreement is observed between the numerical and experimental results for the IP walls in terms of initial stiffness, peak shear force, and crack patterns. However, the results for the OOP walls are significantly overestimated, with an average overestimation of 35% for the peak force. This is attributed to the differences in boundary conditions (full or partial rotation restriction), type of tests (cyclic or monotonic) and loading conditions (displacement control or load control) between the numerical simulation and experimental tests. Nevertheless, the crack patterns are in good agreement with the experiments.

The validated model is used to investigate the OOP performance of pre-damaged walls, including both solid wall (without opening) and wall with an asymmetric opening. Two distinct approaches are considered to simulate the response of the pre-damaged walls. In the first approach, known as the reduced-parameters approach, a model is created with varying properties: reduced stiffness and strengths are assigned to locations where cracks were observed during the IP tests, while regular properties are maintained in other locations. Subsequently, the model is subjected to OOP analyses. In the second approach, known as the sequential loading approach, the wall is initially monotonically loaded in the IP direction that represents the pre-damage of the wall. Then, the OOP load is applied while maintaining the IP pre-deformation until the wall experiences failure. The study considers four different states of pre-damage, ranging from minor to extensive damage. For the solid wall, the damage levels are based on the observed damage during the IP tests up to the maximum drift of 0.2%.

On the other hand, the damage levels for the wall with opening are derived from the damage observed during the IP monotonic pushover numerical simulation up to the maximum drift of 0.14%.

For the solid wall, it is found that both approaches give same results for low pre-applied IP damages, up to 0.06% drift. The reduction of the OOP peak strength is almost negligible until this drift level. As the damage increases, the reduction of the strength also sharply increases. At the maximum of 0.2% IP-drift, 40% reduction of the OOP peak strength of the wall is observed in the reduced-parameters approach, while in sequential loading approach, the wall immediately failed resulting in negligible OOP strength because of the severe IP damage. For the wall with opening, similar to the solid wall, no measurable influence of the OOP strength due to minor IP damages, up to 0.06% drift, could be observed in both approaches. The maximum reduction that could be observed is approximately 15% at maximum of 0.14% pre-applied IP drift. In the sequential loading approach, as the level of pre-damage is increased, the pre-peak stiffness of the force-displacement curve decreases, as expected for a pre-damaged wall. However, the reduced-parameters approach does not show this reduction, which could be attributed to the pre-damage applied only at specific locations. For both types of walls, there is no significant difference in the crack pattern of the undamaged and pre-damaged wall. The well-known envelope crack pattern is obtained in both cases.

To conclude, the out-of-plane load-bearing strength of URM walls is significantly affected by the presence of in-plane damages. The impact is minimal under minor in-plane damages but increases rapidly as the damage becomes more severe.

This thesis limits the numerical analyses to monotonic loading. However, for future research, it would be beneficial to extend the analyses to include cyclic or dynamic loads, as they provide a more realistic representation of seismic loading conditions. Moreover, it is recommended to incorporate various boundary conditions for the OOP loading. For instance, the research could be expanded to include a C-shaped wall configuration, where the lateral edges are supported by return walls, a scenario commonly encountered in practice.

Table of Contents

Chapter 1: Introduction

1.1 Problem statement

In low-rise unreinforced masonry (URM) buildings, the walls are the primary load-bearing elements that should withstand the vertical loads, such as gravity load, as well as the horizontal loads, such as seismic load and wind load. However, in the past, most of the URM structures were designed with minor consideration for seismic design concepts. Masonry is characterized by its high compressive strength and low tensile strength, because of this, URM walls perform better under vertical loads than when subjected to horizontal loading. Figure 1(a) shows the deformation of the building and typical damages to the walls under seismic loading. The wall perpendicular to the direction of seismic action is loaded in out-of-plane (OOP) direction, referred as OOP wall, whereas the wall parallel to the direction of seismic action is loaded in in-plane (IP) direction, referred as IP wall. It can be observed that IP walls fail in shear and flexure, while the OOP wall is characterized by bending failure. OOP walls can be very weak and flexible, especially when they are slender and contain large openings. For OOP walls, a distinction between one-way bending and two-way bending is made depending on the boundary conditions. The wall supported at two parallel edges or only at the bottom edge undergoes one-way bending, while for the two-way bending at least two adjacent edges are supported.

Several past earthquake reports have identified high vulnerability of URM walls to the OOP loading resulting in failure of the URM walls and at times leading to partial to complete collapse of the building (Kaiser et al., 2013; Penna et al., 2014; Dizhur et al., 2016). For instance, the OOP failure of URM walls that occurred during the 2015 earthquake in Nepal can be observed in Figure 1(c). With the aim to better understand the OOP response of URM walls, experimental, numerical and analytical studies have been conducted frequently (Ravenshorst & Messali, 2016b; Graziotti et al., 2019; D'Altri et al., 2019; Chang, 2022; Padalu et al., 2020a). In those studies, different factors that affects the OOP behaviour of URM walls are included, such as boundary conditions, vertical pre-compression, aspect ratio and presence of openings. However, there are hardly any studies that have focused on the effect of pre-damage on the OOP response of URM walls. Hence, there is a gap in the knowledge on the OOP behaviour of masonry walls with IP pre-damage, which could result in inaccurate design and assessment of current and future masonry buildings.

The possible sources of pre-damage of the walls could be settlements and past seismic hazards. For instance, in the region of Groningen, the presence of soft topsoil has caused settlement-induced damages to the buildings. In addition, the houses in Groningen have repeatedly been exposed to low magnitude seismic loading, Figure 1(b), resulting in light damages to the walls. Considering the essence of investigating the influence of pre-damage in unreinforced masonry, Korswagen et al. (2019) showed through experimental tests and numerical simulations that walls with settlement induced pre-damages are more susceptible to experiencing increased damage when subject to in-plane lateral drift. Hence, it is of interest to investigate the performance of URM walls under pre-damaged conditions. Again, not much similar studies have been done for the changes in OOP behaviour due to pre-damage.

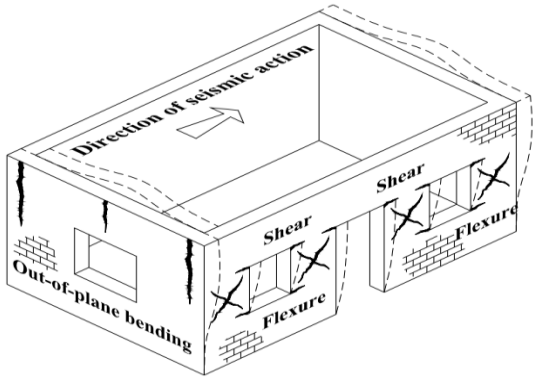

(a)

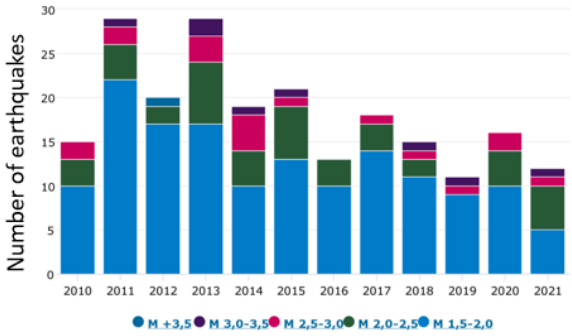

(b)

(c)

Figure 1. (a) Deformation of the building and typical damage on the structural walls (Alejo et al., 2017); (b) Number of earthquakes in the region Groningen, The Netherlands (Staatstoezicht op de Mijnen, 2022); (c) Out-of-plane failure of URM walls in 2015 Earthquake, Nepal (Dizhur et al., 2016)

1.2 Context of present study and research gaps

Few studies in the existing literature have considered the effect of pre-damage on the performance of URM walls. These studies have explored the significant importance of the presence of pre-damage on the OOP capacity of load-bearing masonry walls. For instance, Agnihotri et al. (2013) reported by means of numerical static analyses an OOP capacity reduction of the URM wall to about one-third of its undamaged capacity due to in-plane displacements. An interaction curve was developed making use of finite element simulations. The curve showing the effect of IP damage on the OOP capacity of the wall with slenderness ratio (height-to-thickness ratio) of 16 and aspect ratio (height-to-length ratio) of 1.2 can be observed in Figure 2. Similarly, Dolatshahi et al. (2014) performed a numerical study on the bidirectional behaviour of the URM walls and showed that under uniform OOP pressure the capacity of the wall could decrease by 60% due to IP damages. In another research by Dolatshahi and Yekrangnia (2015), the numerical results indicated that the effect of IP damages on the OOP capacity of URM walls varies from negligible to very high depending on boundary conditions, IP failure mode and IP damage severity. For instance, for the wall with aspect ratio of 2 and rocking/toe crushing failure mode, the reduction could be up to 72% of OOP strength.

As regards of the aforementioned research studies, the capacity of pre-damaged URM walls is focused on walls without openings, and there is lack of data for walls with openings. In principle, almost every URM structure built of masonry walls contains openings in the form of doors and windows. Besides, either 3D micro modelling or 2D continuum-based macro modelling strategies for masonry are applied in the previous studies. With continuum-based macro modelling, the masonry is modelled as a continuum deformable body, whereas in the micro modelling, bricks and mortar layers are separately

modelled considering the actual texture of the masonry. The 2D micro modelling, which in general represents a good balance between the desired level of accuracy in results and the required computational effort, is missing in the previous analyses of pre-damaged walls.

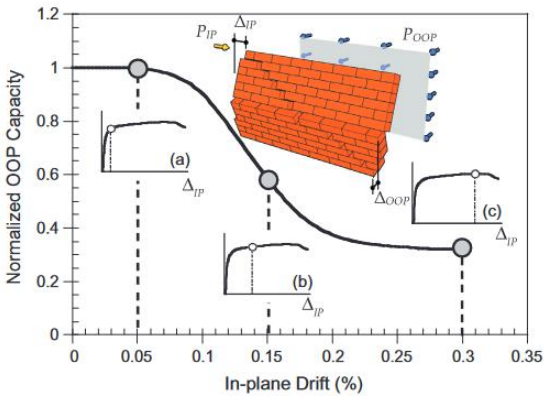

Figure 2. Typical interaction curve showing the effect of IP damage on the OOP capacity of URM wall (Agnihotri et al., 2013)

1.3 Research objective, limitation and questions

The previous discussions indicate the essence of further exploration in the field of understanding the behaviour of URM walls in the presence of pre-damage. Considering the aforementioned research gaps, the main objective of this thesis is to investigate the OOP performance of pre-damaged URM walls, without and with openings. The investigation is performed through numerical simulations adopting 2D micro-modelling approach in the Diana finite element analysis software package, since experimental study is out of the scope of this thesis. As discussed earlier, the possible sources of pre-damage are settlement and past seismic hazards. This study focuses only on the pre-damage that could arise from an equivalent in-plane seismic loading. With reference to the objective and the limitations of this thesis, the main research question is formulated as following:

- ***"How does the in-plane pre-damage affect the out-of-plane load-bearing strength of URM walls?***

The answer to the main research question can be accomplished through answering the sub-questions as stated below:

1. *What modelling approaches, based on finite element method, can be applied to masonry?*
2. *What are the steps for the validation of the applied modelling approach?*
3. *How to identify the IP damages and apply this in the numerical analysis?*
4. *How does the effect of pre-damage differentiate between walls, without and with an opening?*

1.4 Research methodology

This thesis, as already stated, adopts the numerical modelling approach to answer the research question. For this purpose, the research starts with literature review on different modelling strategies that are used to simulate the behaviour of masonry under combined loading. Subsequently, the suitable modelling approach for this thesis is selected i.e., the simplified micro-modelling where bricks are modelled with continuum shell elements and the mortar joints are modelled with zero-thickness interface elements. Also, the potential vertical crack in bricks is considered making use of interface element in the middle of the brick providing an explicit path for the cracks to extend through the bricks.

The calibration and validation of the numerical model is based on the experimental benchmarks on calcium silicate (CS) masonry performed at the TU Delft. Particularly, the mechanical parameters of the numerical model are derived from tests at material level by Esposito et al. (2016) and Jafari & Esposito

(2016), whereas the validation is based on tests of IP and OOP walls by Ravenshorst & Messali (2016a) and Ravenshorst & Messali (2016b), respectively. At first, the mechanical parameters of the numerical model are calibrated based on small scale material characterization tests. Subsequently, the calibrated parameters are directly implemented in the numerical simulation of full-scale CS walls. The numerical results are then validated against tests at structural level. Since there is no evidence of any experimental investigation that resembles the phenomenon addressed in this research, the walls are validated separately for the IP and OOP loading.

At last, the validated model is applied for the simulation of pre-damaged walls. Two different approaches are considered to apply in-plane pre-damage to the wall. In the first approach, the method of reducing material input parameters (both stiffness and strength parameters) is applied at the pre-defined locations of the walls that are considered to be damaged from previous in-plane loadings. The second approach is characterized by the sequential loading process. The wall is loaded in IP direction, which represents the pre-damage of the wall, followed by the OOP load in the same run of the analysis. Further, the simulations are monotonic pushover analyses and performed under four different states of damage. The aforementioned approaches are used to represent four states of pre-damage based on the damages observed during the tests of IP walls. Considering the objective of this thesis, two types of walls, one without opening (hereinafter referred as solid wall) and the other with an eccentric large opening are selected, which were also used for the validation of the model.

A flow-chart illustrating the major aspects of the research methodology can be observed in Figure 3.

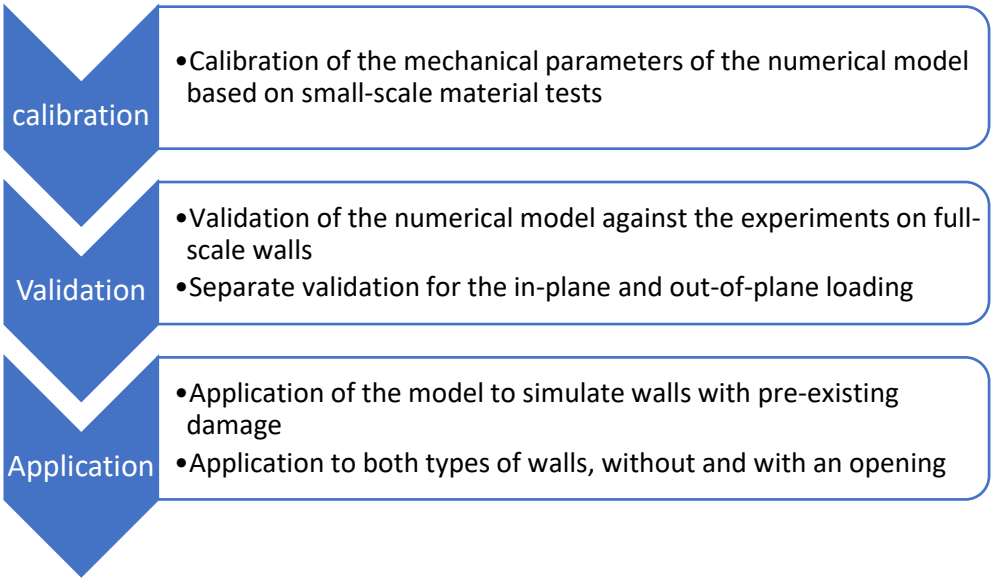

Figure 3. The major aspects of research methodology of this thesis

1.5 Thesis outline

The graphical outline of the thesis is presented below in Figure 4.

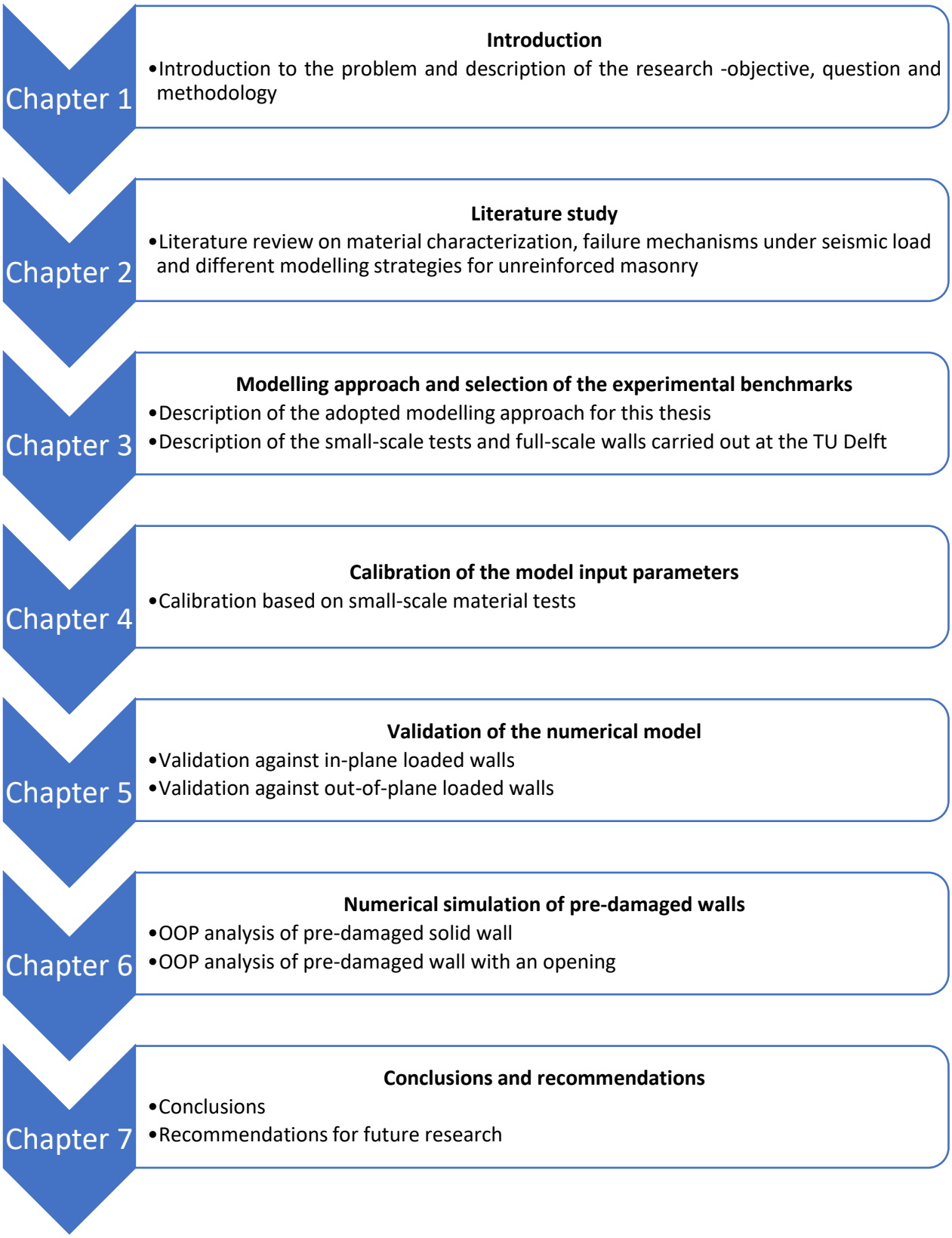

Figure 4. Graphical representation of thesis outline

Chapter 2: Literature study

Literature review is an important part of research. It helps to obtain a better understanding of the topic and provides an overview of existing knowledge on that field to identify the potential knowledge gaps that could be of interest for future research. This chapter starts with understanding the behaviour of masonry at material level. Several tests in the literature have been conducted to characterize the material properties of masonry. Section 2.1 provides a short introduction to the mechanical behaviour of masonry under tension, shear and compression. The review on the response of masonry at structural level, with respect to the seismic loading, is presented in section 2.2. This section particularly gains insight into the failure mechanisms of URM walls under seismic loading and the interaction between IP and OOP loading. Section 2.3 provides an overview of the modelling strategies for the computational analysis of URM structures.

2.1 Material characterization of masonry

Since masonry is a composite material consisted of units (blocks) glued together with mortar, it is important to first identify the mechanical properties of its components and small masonry samples to understand the structural behaviour of masonry structures. The properties of masonry such as strength, stiffness and toughness are governed by the material properties of its components and the interaction between them, also known as the unit-mortar interface.

2.1.1 Properties of unit and mortar

The commonly technique performed to determine the material properties of the masonry components, particularly the compressive strength, is the compression test on single components. For the units, the test is performed on cubic specimens, whereas for the mortar joints, the test is performed on mortar cubes or cylindrical blocks. These specimens should be tested according to the guidelines of the available standards e.g., the European Standards, EN 772-1(CEN 2011) for the units and EN 1015-11(CEN 1999) for the mortar joints. The reader is referred to these standards for more information about the testing procedures. The range of the values associated to these properties is too wide and depends on different factors such as workmanship, quality of the raw material, baking procedure (for baked bricks), etc.

For the determination of the tensile properties of the masonry components, it is not common to perform a direct tension test since it has practical difficulties such as gripping problem resulting in stress concentration. Furthermore, due to differences in type of unit, shape, manufacturing process and degree of perforation, it is also difficult to find the relationship between the tensile strength and compressive strength of the units. Schubert (1988a) performed experiments on clay, calcium-silicate and concrete units to relate the longitudinal tensile strength of the units to its compressive strength and found the ratio to be in the range 0.03 to 0.10. Similarly, Van der Pluijm (1992) reported fracture energy of solid clay and calcium silicate units ranging from 0.06 to 0.13 N/mm for tensile strength values ranging from 1.3 to 3.5 N/mm^2.

2.1.2 Properties of unit-mortar interface

The most important aspect of masonry is the bond between unit and mortar, since often this is considered to be the weakest link in masonry construction. Depending on the mechanical and physical characteristics of the units and the mortar joints, it is possible to have two modes of failure in the unit-mortar interface. Mode I is related to tensile failure, whereas Mode II is related to shear failure.

Mode I failure

Since masonry is a quasi-brittle material, it undergoes the process of progressive crack growths resulting in a nonlinear post-peak behaviour for tensile failure. To understand this behaviour for the

unit-mortar interface under tension, Van der Pluijm (1992) conducted displacement-controlled tests on small specimen of solid clay- and calcium-silicate masonry. As it can be observed in Figure 5, the tests resulted in an exponential tension softening curve with a fracture energy ranging from 0.005 to 0.02 N/mm for a bond strength ranging from 0.3 to 0.9 N/mm^2. The dissipated energy, the area underneath the tensile softening curve, is known as the Mode I (tensile) fracture energy. It should be noted that the average net bond surface of the specimen was proven to be about 35% of the total area of the joint due to shrinkage of the mortar and the process of laying units in the mortar.

Mode II failure

As mentioned earlier, the mode II failure is associated with the shear-sliding behaviour along the unit-mortar bond interface. To capture this behaviour, several researchers performed different tests aiming to generate pure and uniform shear stresses along the interface (Atkinson et al., 1989; Van der Pluijm, 1993). The test performed by Van der Pluijm (1993) for this purpose is shown in Figure 6, where the specimen is loaded in shear under different levels of confining stresses. The response is an exponential shear softening curve with a residual dry frictional resistance, Figure 7(a). The area underneath the stress-displacement curve is denoted as Mode II fracture energy and is assumed to be a material property. This fracture energy is dependent on the level of confining stress, as it can be observed in Figure 7(b). From the experiment, additional parameters such as initial internal friction angle, residual internal friction angle and dilatancy angel can be obtained which are the important inputs in the micro-modelling strategy (Lourenco, 1996). The dilatancy angel measures the uplift of one unit over the other upon shearing and is dependent on the level of confining stress.

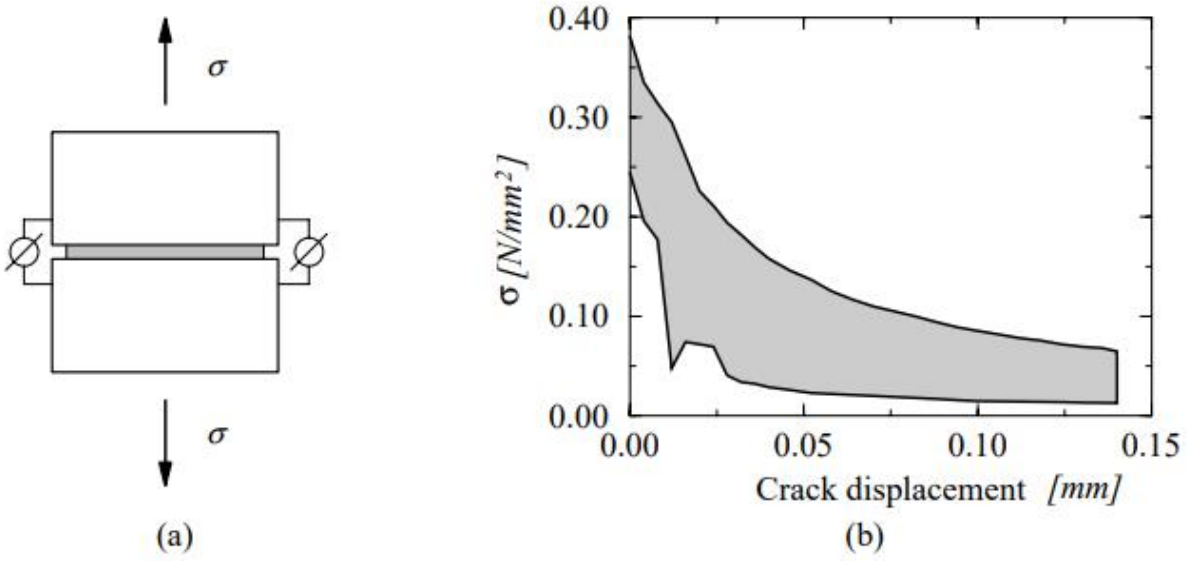

Figure 5. Unit-mortar interface behaviour under tension (a) test specimen; (b) tension-softening curve for solid clay brick masonry with shaded area representing the envelope of three tests (Van der Pluijm, 1992)

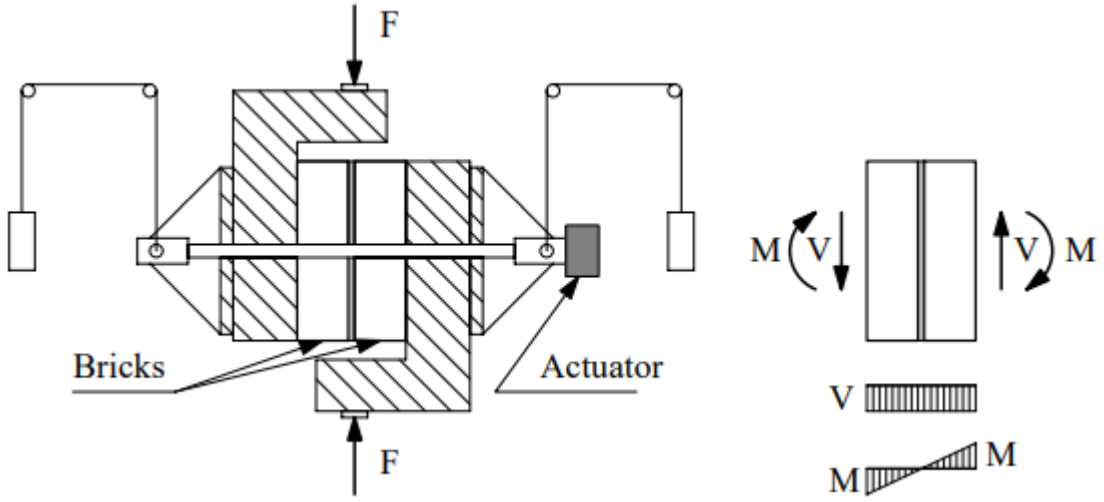

Figure 6. Testing of shear-sliding behaviour of unit-mortar interface (Van der Pluijm, 1993)

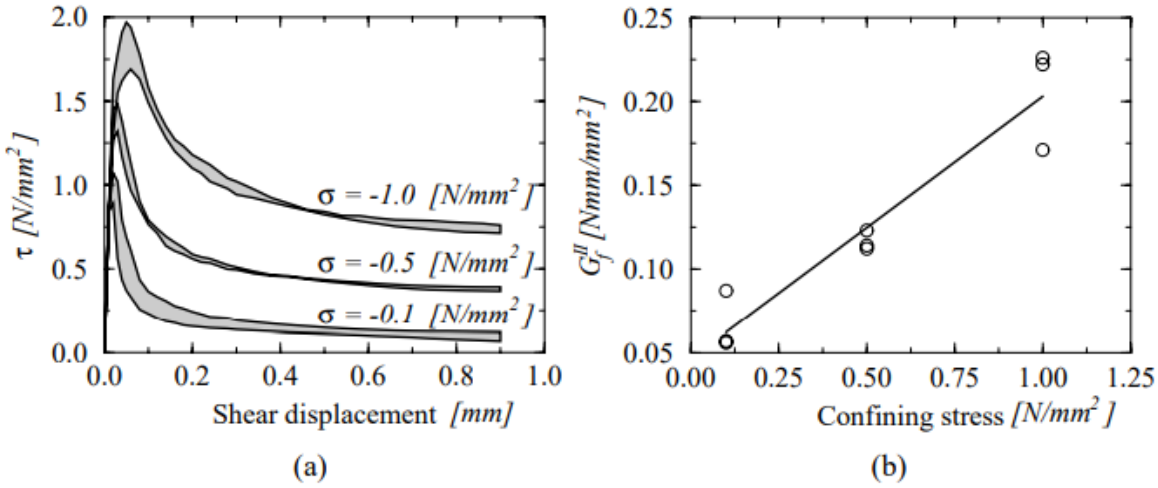

Figure 7. Shear-sliding behaviour of unit-mortar interface for solid clay units (a) stress-displacement curve for different confining stress levels; (b) mode II fracture energy as a function of the confining stress (Van der Pluijm, 1993)

2.1.3 Uniaxial compressive behaviour of masonry assemblage

The behaviour of masonry under compressive load is usually obtained from the stack-bond prism loaded in the direction perpendicular to the bed joints, as it can be observed in Figure 8(a). This method of determining the uniaxial compressive strength of the specimen is simple in construction and handling. However, the so-called RILEM test, shown in Figure 8(b), is also commonly accepted as it resembles the actual bond pattern, including the influence of the head joints. The applied uniaxial compressive loading of the stack-bond prism results in triaxial compression in the mortar and compression/biaxial tension in the unit. This effect initiates the vertical cracks in the units along the middle of the specimen. Failure occurs by vertical splitting of the specimen upon increasing deformation. An example of the experimental load-displacement diagrams of prisms of solid soft mud brick can be observed in Figure 9, (Lourenco, 1996). It can be seen that the failure of the specimen is more brittle with the increasing mortar compressive strength.

Since masonry is an anisotropic material, the uniaxial compression tests are performed along the two orthogonal directions. However, the compressive strength of masonry in the direction perpendicular to the bed joints is regarded as the sole relevant structural material property. Hoffmann and Schubert (1994) carried out the uniaxial compression tests along the two orthogonal directions on masonry

samples of solid and perforated clay units, calcium-silicate units, lightweight concrete units and aerated concrete units. They obtained the ratio ranging from 0.2 to 0.8 between the uniaxial compressive strength in the direction parallel and perpendicular to the bed joints.

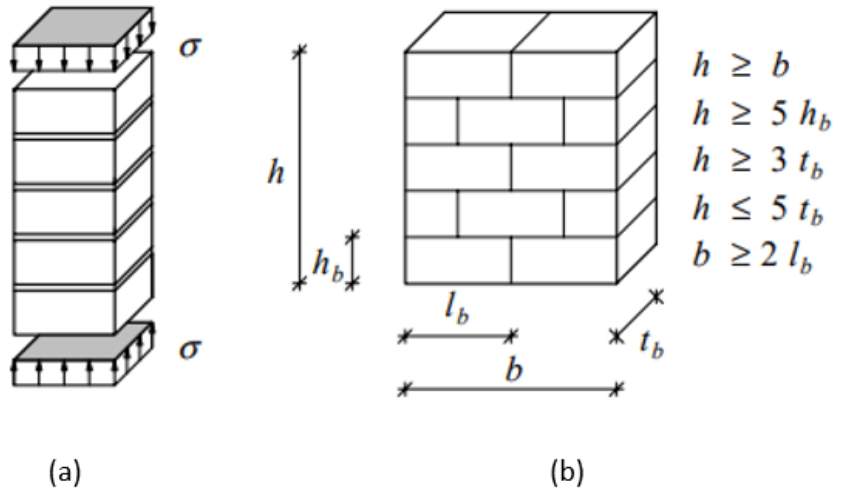

Figure 8. Uniaxial compression test (a) stack-bond prism; (b) RILEM test specimen (Lourenco, 1996)

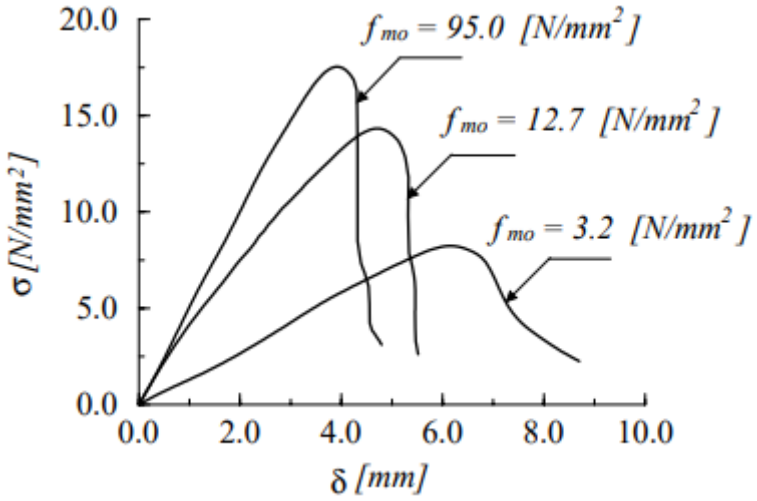

Figure 9. Experimental stress-displacement diagrams for 500x250x600 mm³ prisms of solid soft mud brick, where f_{mo} is the mortar compressive strength (Binda et al.,1988)

2.1.4 Uniaxial tensile behaviour of masonry assemblage

As in the case of compression tests, the masonry assemblage is experimented in two orthogonal directions for tensile loading. The failure mechanism of the specimen in tension is governed by the relative strength of the joints and the units. In the direction perpendicular to the bed joints, the failure generally occurs due to the low tensile bond strength between the bed joint and the unit and therefore this tensile bond strength is taken as rough approximation of the masonry tensile strength (Lourenco, 1996). However, it is also possible to have greater tensile bond strength between the bed joint and the unit than the tensile strength of the units. In that case, the cracks arise in the units and therefore the tensile strength of the units is considered as rough approximation of the masonry tensile strength.

For tensile loading parallel to the bed joints, Backes (1985) obtained through experiments the stress-displacement diagram as shown in Figure 10. Similar to the case of tensile loading perpendicular to the bed joints, the specimen failure type is dependent on the relative tensile strength of the joints and the units. For higher tensile strength of the units, the cracks develop through head and bed joints. In this situation, the post-peak response is governed by the fracture energy of head joints and shear-sliding behaviour (Mode II failure) of the bed joints (Lourenco, 1996). For lower tensile strength of the units, the cracks grow vertically through the units and head joints, and the post-peak response of the specimen is governed by the fracture energy of the units and head joints. This type of failure has less residual capacity upon increasing deformation than the other, as it can be observed in Figure 10(b) (Lourenco, 1996).

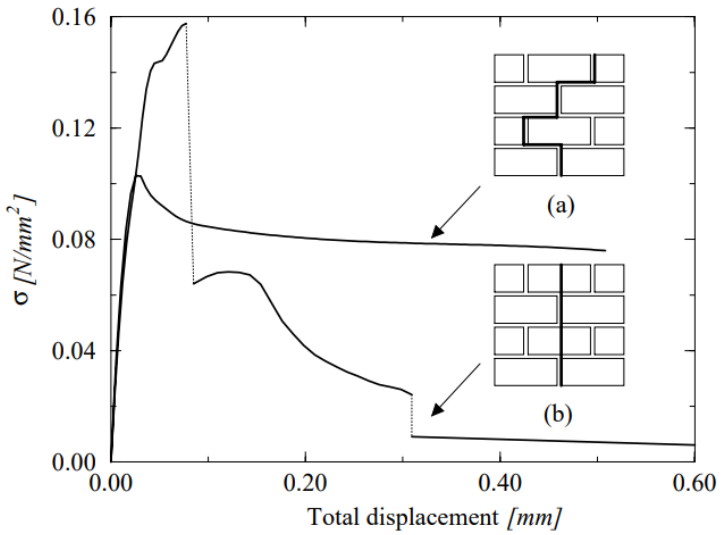

Figure 10. Experimental stress-displacement diagrams for tensile loading parallel to the bed joints (a) failure type for higher tensile strength units (b) failure type for lower tensile strength units (Backes, 1985)

2.1.5 Biaxial behaviour

Since masonry is an anisotropic material, its mechanical behaviour under biaxial states of stress is described in terms of principal stresses and the rotation angle between the principal stresses and the material axes (Lourenco, 1996). This rotation angle and the principal stress ratio considerably influence the failure mode and strength. The different failure modes of solid clay bricks masonry under biaxial loading can be observed in Figure 11. It can be seen that at 45° rotation angle the failure occurs mainly following the stepwise crack pattern along the head and bed joints. At other rotation angles the failure occurs either by cracking and sliding of the mortar joints or including both cracking and sliding of the mortar joints and cracking through bricks. It should be noted that the behaviour observed at different angles are not the same for all masonry and depend on the dimension of the bricks and their bond pattern.

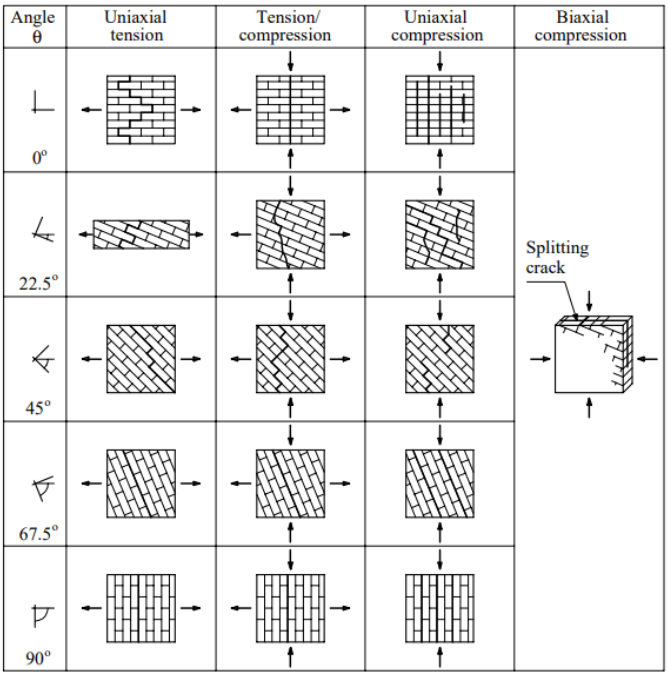

Figure 11: Different failure modes of solid clay masonry under biaxial loading (Dhanasekar et al.,1985)

2.2 Seismic behaviour of unreinforced masonry

During an earthquake, structural walls of masonry buildings are exposed to lateral loading from different directions. As mentioned earlier, a distinction is made between the IP loading and the OOP loading of the wall according to the direction of seismic action. The associated seismic behaviour of the wall to these loading directions are denoted as IP failure and OOP failure. Some typical damages on structural walls of the building due to seismic loading can be observed in Figure 1(b). The OOP bending of the wall causes vertical cracks at the corners and at the middle of the wall. In the IP direction of the walls, the damage consists of horizontal and diagonal cracks due to bending and shear respectively.

Whether the IP or OOP failure occurs, depends on several factors, such as the material properties, the geometry of the structure, the foundations, the loading direction, the connections between walls and floors, the connections between walls and roof and the stiffness of the horizontal diaphragms, Alejo et al. (2017). The so called 'box-behaviour' is of great importance for masonry structures to avoid OOP failure, since OOP failure of the wall might lead to partial or complete collapse of the building, Kaiser et al. (2013); Dizhur et al. (2016). Box-behaviour refers to the case where there is a strong connection between orthogonal walls and stiff rigid floor diaphragm, and therefore results in the desired IP shear failure under seismic loading.

2.2.1 In Plane failure of URM Wall

Observations from previous earthquakes such as in L'Aquila (Italy, 2009) and Canterbury (New Zealand, 2010 and 2011), and the experimental tests by Esposito & Ravenshorst (2017) have resulted in four possible types of IP failure mechanisms for the URM walls as shown in Figure 12: rocking, sliding shear, toe-crushing and diagonal tensile cracking. Rocking and toe-crushing are associated with flexural failure, whereas sliding shear and diagonal tensile cracking are shear failures. The different failure modes are usually characterized by the aspect ratio and vertical axial stress, Yi (2004). It should be noted, however, the behaviour of the walls also depends on other parameters such as boundary conditions and material properties (e.g., mortar quality).

For walls with high aspect ratio (e.g., slender walls), rocking and toe-crushing may occur for low and high vertical axial stresses, respectively, Yi (2004). When the vertical axial stress is low, flexure causes horizontal cracks in the mortar bed joints at the bottom of the wall leading to rocking failure. For increasing vertical axial stress and low compressive strength of the blocks, the wall becomes more susceptible to toe crushing.

Shear failure is governing in walls with low aspect ratio (for e.g., squat walls), Yi (2004). For low vertical axial stress, horizontal cracks are formed at the base of the wall due to the sliding on one of the horizontal mortar joints. This is known as sliding shear failure. For higher vertical axial stress, the diagonal cracks are formed from one of the top corners to the bottom corner at the other side of the wall dividing the wall into two parts, which is known as diagonal tension failure.

Flange effect: The in-plane behaviour of the wall can be affected by the presence of adjacent transverse walls, also known as 'flanges' in literature. This so-called flange effect may increase the stiffness and strength, as well ultimate displacement capacity of the in-plane wall, since the flanges contribute to increase the effective length of the wall. Patel & Dubey (2022) concluded through numerical analysis that the presence of flanges significantly increases the strength of the wall, when the wall fails by rocking/toe-crushing, diagonal tension cracking or a combination of both subjected to higher vertical axial stress. However, at low vertical axial stress, no significant influence of the flanges on the in-plane response of the wall was observed.

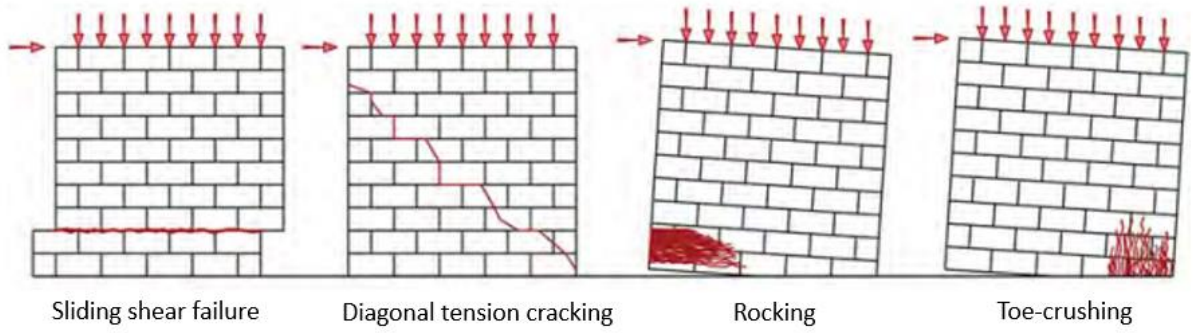

Figure 12: Typical in-plane failure modes of masonry walls (Oyguc & Oyguc, 2017)

2.2.2 Out of Plane failure of URM Wall

URM walls are very weak and prone to large deformations and collapse when loaded in the OOP direction of the wall. In general, the walls are not designed for the OOP loading. During an earthquake, the walls are subjected to OOP inertia forces, causing the walls to fail in one-way or two-way bending/flexure. A distinction is made between one-way spanning and two-way spanning walls depending on the support conditions. The OOP behaviour of the walls for various types of support conditions can be observed in Figure 13 and Figure 14. For one-way spanning walls, cracks running parallel to the supports (either horizontal or vertical) are formed, whereas for two-way spanning walls, a combination of horizontal, vertical and diagonal cracks can be observed. The two-way spanning walls are most commonly encountered in practice, hence the behaviour of URM walls in two-way bending is discussed in the following paragraph.

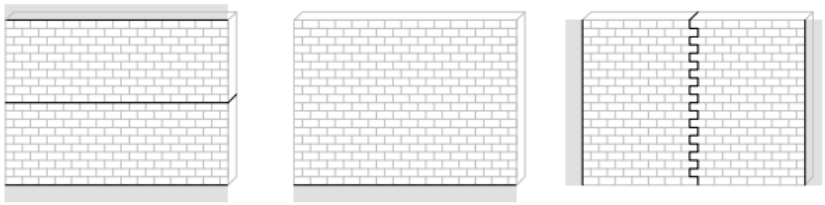

Figure 13. OOP flexure cracking patterns for one-way spanning walls (Vaculik, 2012)

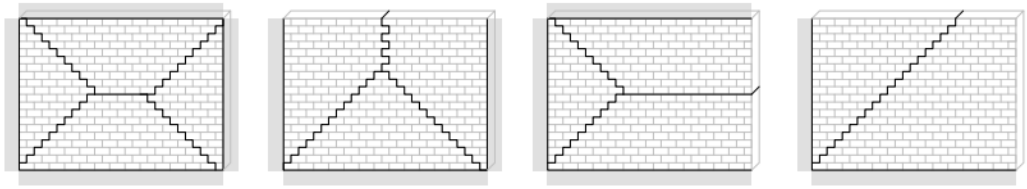

Figure 14. OOP flexure cracking patterns for two-way spanning walls (Vaculik, 2012)

In two-way spanning configuration, the wall is supported by return walls (also called flanges) along its vertical edges providing rotational restraints and the top edge is connected to a floor/roof system. During an earthquake, the integrity between these components plays significant role on the OOP behaviour of the wall. The structural integrity relies on the quality and strength of the connections between orthogonal walls and between walls and floor/roof system, and the stiffness of the horizontal diaphragm. Lack of integrity between walls and other elements may result in separation of the walls from returning elements at the corner of the building. The building then becomes vulnerable to (partial) overturning mechanisms (one-way bending). Figure 15(a) shows the schematics of different overturning mechanisms, and in Figure 15(b) the real damage of the masonry building precursor to partial overturning of the façade can be observed (Mechanism C). Further, the flexibility of the roof/floor diaphragm causes the OOP failure of masonry walls, especially if the diaphragm system is not properly connected to the walls. Some examples of OOP wall failures due to flexible roof diaphragm (timber floor diaphragm) are illustrated in Figure 1(c).

(a) (b)

Figure 15. (a) Schematics of different overturning mechanisms (D'Ayala & Speranza, 2003); (b) Initiation of partial overturning of the façade of masonry building (Dizhur et.al., 2016)

Another important parameter that may affect the OOP behaviour of masonry walls is the opening in the wall. In general, the presence of openings decreases the lateral force capacity of the wall. An overview of experimental studies on the influence of openings on two-way bending capacity of URM walls has been done considering two different arrangements of the opening area (Chang et.al., 2022). For non-covered and non-loaded opening area, the two-way bending capacity of the perforated wall (defined as the peak pressure applied to the wall net area) is higher than that of the corresponding wall without opening. However, for openings covered with timber or glass plates and loaded as the rest of the wall, the two-way bending capacity of the perforated wall is lower than that of its counterpart without opening.

2.2.3 Interaction between In Plane and Out of Plane behaviour

Typically, masonry walls are analysed either for their IP or OOP capacity independently. The mutual influence of one on the other is often disregarded in design. However, it is essential to recognize that the walls can be subjected to simultaneous and combined IP and OOP loading during an earthquake. Research has been conducted to investigate the bidirectional behaviour of URM walls and the interaction curves have been developed (Najafgholipour et al.,2013; Najafgholipour et al.,2014; Dolatshahi et al., 2015; Noor-E-Khuda & Dhanasekar, 2018). Najafgholipour et al. (2013) conducted experiments on 600 × 600 × 100 mm brick masonry panels under diagonal compression along with a central point load applied perpendicular to the plane of the wall. As a result, a circular interaction curve of the IP and OOP forces was obtained. Similar interaction curve was also developed in Noor-E-Khuda & Dhanasekar (2018). The numerical research involved subjecting URM walls to initial vertical compression and OOP loads. Subsequently, the IP displacements along the top edge of the wall were applied to simulate the multidirectional loading. Interaction curves were then generated considering both the effects of precompression and the aspect ratio of the wall. It was shown that the IP capacity significantly decreased with the increase in the OOP loading. Further, it could be observed that with the increase in vertical pre-compression, the IP and OOP capacities of the wall increased, but there were negligible changes in the shape of the interaction curve.

Furthermore, as mentioned in section 1.2, previous research has explored the influence of IP pre-damage on the OOP strength of URM walls. Dolatshahi et al. (2014) demonstrated through numerical investigation that when subjected to uniform OOP pressure, the wall's capacity could decrease by up to 60% due to IP damages. In another study by Dolatshahi and Yekrangnia (2015), the numerical findings revealed that the impact of IP damages on the OOP capacity of URM walls varied significantly based on factors such as boundary conditions, IP failure mode, and the severity of IP damage.

These findings highlight the significance of accounting for the interaction between the IP and OOP forces in the design of masonry walls.

2.3 Modelling strategies for unreinforced masonry structures

In the paper by D'Altri et al. (2019), a comprehensive review of the existing modelling strategies for the analysis of masonry structures is presented. According to this paper, the modelling strategies can be classified into four categories: block-based models, continuum models, macroelement models and geometry-based models. The aspects of these modelling strategies are discussed shortly in this section.

2.3.1 Block-based models

Block-based models are based on the actual texture of the masonry. The blocks and the mortar layers are modelled with linear elastic or non-linear continuum elements and the interface between the block and the mortar layer are represented by zero-thickness interface or contact elements. This type of modelling is also known as micro modelling. There exists a simplified version of this modelling type,

called simplified micro modelling, where the blocks are enlarged, and zero-thickness interface elements represent the mortar joints (mortar and block-mortar interface). The schematic representations of micro modelling and simplified micro modelling can be observed in Figure 16.

Since this type of modelling considers the actual texture of the masonry, it is able to reproduce the failure mechanisms of masonry structures in a detailed manner, Figure 17(a). Furthermore, it can be used to characterize the mechanical parameters of the numerical model at material level, which then can be applied directly to the analysis of full-scale walls, D'Altri et al. (2019). The main drawback of this modelling technique is its huge computational demand, especially when it is adopted in a 3D framework, which limits its applicability to small-scale tests and panel-scale structures. In general, it is observed that 2D plane stress elements for bricks and line interface elements for the mortar joints are sufficient to simulate the IP response of URM walls (Lourenco & Rots, 1997; Lee, 2022). The results are well predicted in terms of the force capacity and crack patterns. However, for the analysis of the OOP response of URM walls, mostly solid elements with plane interface or contact elements are used (D'Altri et al., 2018; D'Altri et al., 2019; Chang, 2022).

2.3.2 Continuum models

In continuum models, also known as macro modelling in the literature, the masonry is considered as a homogenized continuum deformable body, without any distinction between units and mortar joints, Figure 17(b). This has an advantage of possibility to have a large mesh size in the model, which reduces the computational time and, hence, is suitable for the analysis of masonry structures on a large-scale model. However, the definition of the appropriate homogenous constitutive law is a challenging task since masonry is a complex material and therefore the level of accuracy with this model is lower than the micro modelling approach. The mechanical characterization of the masonry for this modelling technique can be defined directly through experimental tests (van der Pluijm, 1999a; Jafari, 2022) or through homogenization procedures, Sacco (2018).

Compared to block-based models, this modelling technique is not capable of capturing the crack patterns in a detailed manner, for instance stepwise crack pattern, which is commonly observed in masonry. It requires some extra effort for the proper interpretation of the failure modes in the structure, such as the one shown in Figure 17(b). Continuum models mostly use 2D shell elements that can simulate both the IP and OOP response of URM walls (Agnihotri et al., 2013; Najafgholipour et al., 2014; Noor-E-Khuda, 2018).

2.3.3 Macroelement models

In macroelement models, the structure is divided into deformable panel-scale structural components (macro-elements), representative of piers and spandrels, linked by rigid links or non-linear interfaces, D'Altri et al. (2019). Piers are the vertical components, while spandrels are the horizontal components between two vertically aligned openings, Figure 17(c). This type of modelling approach is found to be effective for the analysis of global seismic response of the masonry, mostly relating to the IP behaviour of the masonry walls. Generally, the OOP response of masonry walls is not included in this model.

2.3.4 Geometry-based models

In geometry-based models, the structure is modelled as a rigid body defined by its geometry. The structural equilibrium and collapse mechanisms are based on limit-analysis solutions, derived from either static- or kinematic-theorem based approaches, D'Altri et al. (2019). This type of modelling is primarily applied for the investigation of equilibrium states and collapse mechanisms in complex masonry structures such as vaults and shells, Figure 17(d).

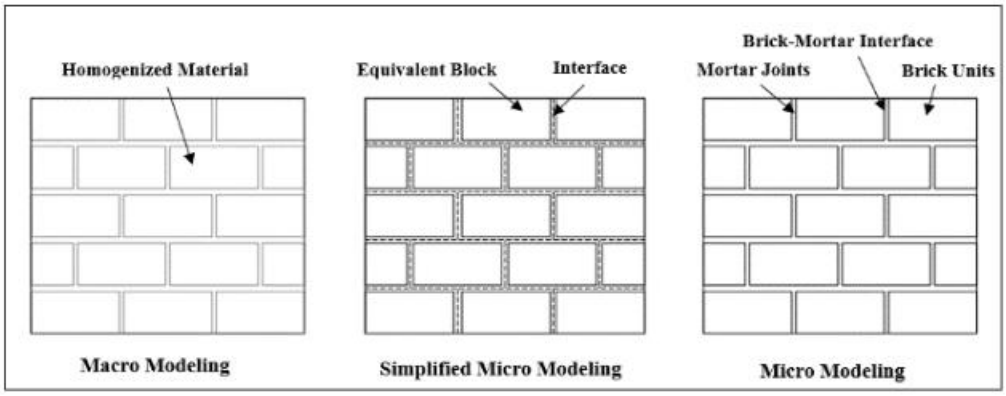

Figure 16. Schematic representation of micro and macro-modelling strategies for masonry (Najafgholipour, 2018)

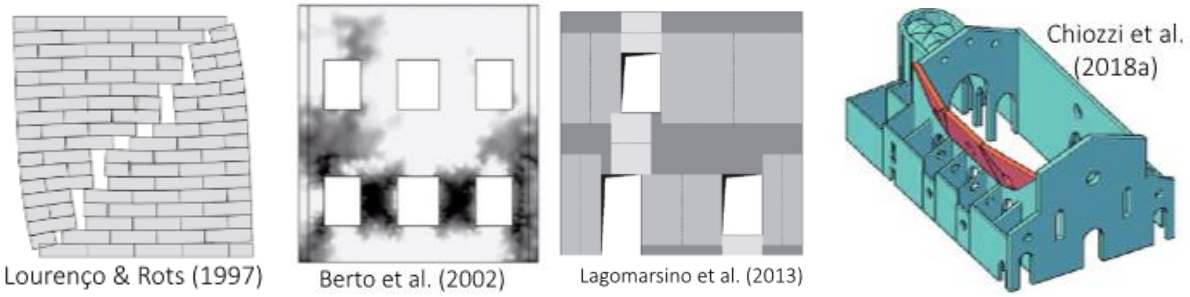

Figure 17. Examples of different modelling strategies for masonry structures (a) block-based model; (b) continuum model; (c) macroelement model; (d) geometry-based model

Chapter 3 Modelling approach and selection of the experimental benchmarks

3.1 Selection of the suitable modelling approach for this research

Referring to the section 2.3, block-based model is most suitable for this thesis research. Within the block-based model, the simplified micro modelling with shell elements is selected because of the following reasons:

- For the inclusion of the pre-damage, it is convenient to use micro-modelling approach compared to the continuum model. The pre-damage, mostly the diagonal stepwise crack patterns, due to the IP loading can be implemented in a detailed manner by reducing the mechanical parameters for the interfaces at certain locations. This is not possible in a continuum or macroelement model since they require extensive trial and error procedures to give close-to-reality results.
- For the scope of this thesis, which is a preliminary investigation, the simplified micro modelling finds an acceptable balance between the desired level of accuracy in results and the required computational effort.
- It is observed that, in general, plane stress elements are used for the IP loading and solid elements for the OOP and/or combined loading. However, Alex and Menon (2017) showed that the simplified micro modelling with shell element is also able to capture the interaction between IP and OOP responses in URM walls under seismic loads. The main advantage of using shell element is the reduction in the computational time as it contains fewer elements than solid elements.

3.2 Description of the adopted modelling approach

In this report, the simplified micro-modelling approach, as depicted in Figure 18, is adopted to simulate the behaviour of URM walls. The mortar joints are modelled with zero-thickness interface elements and the expanded bricks (expanded to account for the geometry of the mortar joints) are modelled as continuum shell elements with potential cracks within the bricks. The tensile failure of the bricks is represented by a vertical line interface in the middle of the brick and assumed to have a linear behaviour in compression. For the interface elements, the composite interface material model, also known as combined cracking-shearing crushing (CCSC) interface model, is applied. A brief description of the element types and the CCSC interface model used in this report is discussed in the following paragraphs.

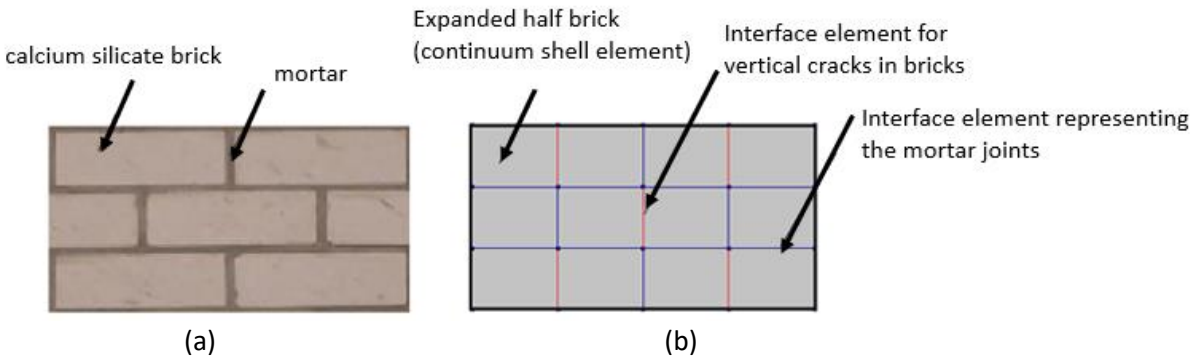

Figure 18. Numerical modelling of masonry (a) masonry sample; (b) adopted simplified micro-modelling strategy.

3.2.1 Element types

For half bricks, element type Q20SH is used which is a four-node quadrilateral isoparametric curved shell element based on linear interpolation. It has three translational- and two rotational degrees of

freedom at each node, as shown in Figure 19, and uses 2x2 Gauss integration scheme over the element area. In the thickness direction, 7-point Simpson integration method is used. The mortar joints and vertical cracks in the bricks are represented by L16IF, which is an interface element between two lines in a curved shell configuration. The basic variables of this interface element are three translational- and one rotational degrees of freedom at each node, as depicted in Figure 20. It is based on linear interpolation and uses 2-point Newton-Cotes integration scheme in the longitudinal direction and 7-point Simpson integration scheme in the thickness direction. It should be noted that the behaviour of interface elements is described in terms of a relation between the tractions and relative displacements across the interface.

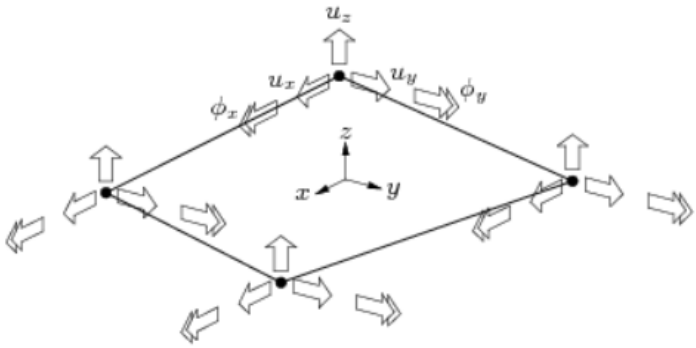

Figure 19: Variables of curved shell element Q20SH

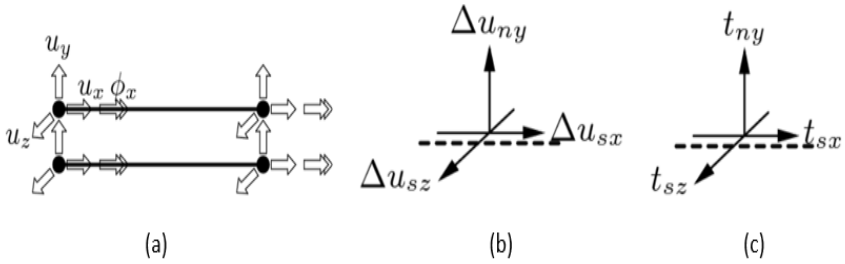

Figure 20: Variables of interface element L16IF (a) displacements; (b) relative displacements; (c) tractions (DIANA FEA BV., 2021)

3.2.2 Interface material model

The constitutive behaviour of the interface elements is described by combined cracking-shearing-crushing (CCSC) interface model, Figure 21. This model, developed by Lourenco & Rots (1997), is based on multi-surface plasticity, comprising a Coulomb friction model with tension cut-off and a compression cap. In the elastic regime the relation between the tractions and the relative displacements is described as follows.

$$\begin{Bmatrix} t_{ny} \\ t_{sx} \\ t_{sz} \end{Bmatrix} = \begin{bmatrix} k_{ny} & 0 & 0 \\ 0 & k_{sx} & 0 \\ 0 & 0 & k_{sz} \end{bmatrix} \begin{Bmatrix} \Delta u_{ny} \\ \Delta u_{sx} \\ \Delta u_{sz} \end{Bmatrix}$$

where, t_{ny} is the normal traction, t_{sx} & t_{sz} are the shear tractions, k_{ny} is the normal stiffness and k_{sx} & k_{sz} are the shear stiffnesses and Δu_{ny} is the normal relative displacement and Δu_{sx} & Δu_{sz} are the shear relative displacements of the interface elements. Beyond the elastic phase, softening is employed in all three modes and preceded by hardening for the compression cap. After reaching the tensile strength, the Mode-I softening is governed by the following exponential function.

$$\sigma_t = f_t e^{-\frac{f_t}{G_f^I} u_n}$$

where, u_n is the normal relative displacement and f_t and G_f^I are the bond strength and the Mode-I fracture energy of the masonry, respectively. The shear mode (Coulomb friction) of the interface elements is described by the following equation.

$$\tau = \sigma \, tan\varphi + c$$

where, c is the cohesion of the brick-mortar interface, φ is the friction angle and σ is the stress normal to the interface. The Mode-II softening is governed by the following equation.

$$c = c_0 e^{-\frac{c_0}{G_f^{II}} u_s}$$

where, u_s is the shear relative displacement and c_0 and G_f^{II} are the initial cohesion of the brick-mortar interface and the shear-slip fracture energy, respectively.

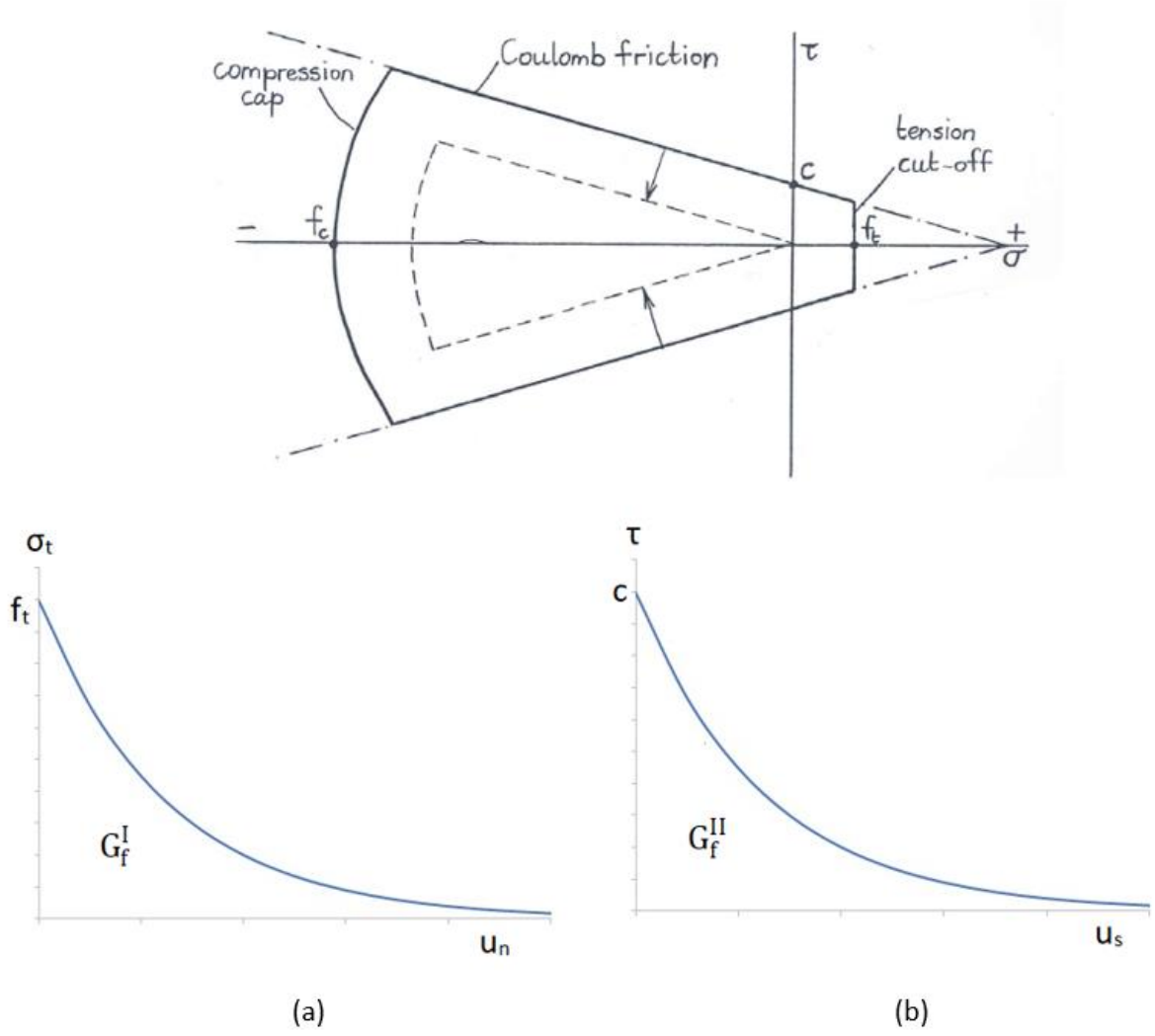

Figure 21: Combined Cracking-Shearing-Crushing (CCSC) Interface Model with (a) tensile softening (b) shear softening (Esposito, 2019)

For the interface compression cap, the compressive behaviour is described by a parabolic hardening rule, followed by exponential softening after reaching the peak strength, Figure 22. The vertical axis

exhibits the compressive stresses, whereas the horizontal axis represents the equivalent relative plastic displacements corresponding to the compressive stresses. The hardening-softening curve is divided into three regions as given by the following equations, with $\overline{\sigma_i} = \frac{f_c}{3}$, $\overline{\sigma_m} = \frac{f_c}{2}$ and $\overline{\sigma_r} = \frac{f_c}{7}$, where f_c is the peak compressive strength.

$$\bar{\sigma}_1(\kappa_3) = \bar{\sigma}_i + (f_c - \bar{\sigma}_i)\sqrt{\frac{2\kappa_3}{\kappa_p} - \frac{\kappa_3^2}{\kappa_p^2}}$$

$$\bar{\sigma}_2(\kappa_3) = f_c + (\bar{\sigma}_m - f_c)\left(\frac{\kappa_3 - \kappa_p}{\kappa_m - \kappa_p}\right)^2$$

$$\bar{\sigma}_3(\kappa_3) = \bar{\sigma}_r + (\bar{\sigma}_m - \bar{\sigma}_r)\exp\left(2\left(\frac{\bar{\sigma}_m - f_c}{\kappa_m - \kappa_p}\right)\left(\frac{\kappa_3 - \kappa_m}{\bar{\sigma}_m - \bar{\sigma}_r}\right)\right)$$

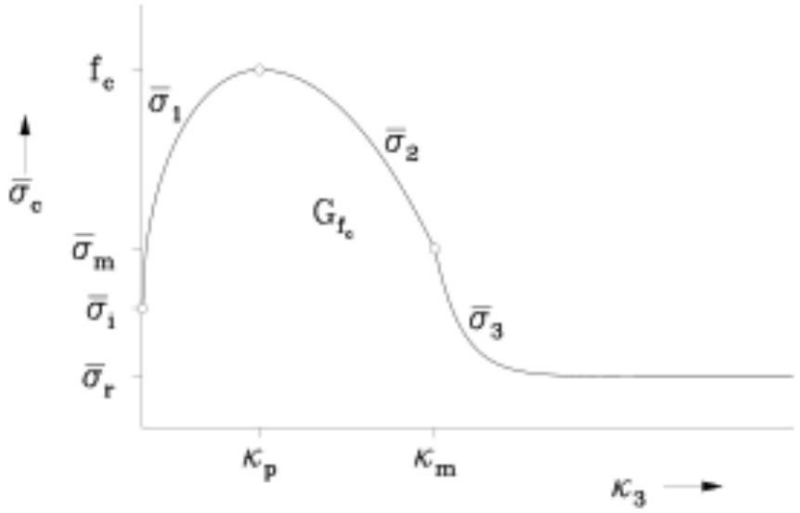

Figure 22: Hardening-softening law for interface compression cap (DIANA FEA BV., 2021)

The CCSC material model is appropriate to simulate the behaviour of masonry structures, since most sources of non-linearity (cracking, shearing and crushing) of the masonry is defined in the mortar joints. However, this model does not perform well under cyclic loading, since it assumes a purely plastic behaviour for the interfaces, which means elastic unloading/reloading. With this assumption, the actual cyclic behaviour of interfaces, as observed during the experiment, namely stiffness degradation and crack closing/reopening cannot be simulated accurately, Oliveira & Lourenço (2004). This was also observed in Lee (2022), where the cyclic analysis of IP wall with CCSC model resulted in overly stiff response under unloading and reloading showing overestimation of the dissipation energy.

3.3 Experimental benchmarks for the validation of the modelling approach

The validity of the numerical model is established by testing its performance against the experimental benchmarks. Extensive testing programmes have been conducted at the TU Delft aiming to understand the behaviour of masonry structures under seismic loading. From this series of tests, the tests performed on calcium silicate brick masonry, at material and structural levels are selected as benchmarks for the following reasons:

- Small-scale tests at material level can be used for the calibration of the model parameters.
- Tests on full-scale walls can be used for the validation of the model.
- Both the IP and OOP behaviour of URM walls have been tested.
- Easy access to the experimental data and its availability in detail

The calibration of the model is based on small-scale tests performed in Esposito et al. (2016) and Jafari & Esposito (2016), whereas the tests of IP walls in Ravenshorst & Messali (2016a) and OOP walls in Ravenshorst & Messali (2016b) are selected for the validation. The tests are shortly introduced in the following paragraphs. For more detailed description of the tests, the reader is referred to the cited references.

3.3.1 Small-scale tests

For the material characterization of CS brick masonry, many small-scale monotonic tests such as shear tests on masonry triplets, compression tests on masonry wallets, bond wrench tests on masonry couplets, bending tests on brick specimens and masonry wallets have been carried out at the Stevin II laboratory of the TU Delft. These tests are therefore selected for the calibration of the mechanical properties of the numerical model. Figure 23 provides an overview of the selected tests and their relation to the specific mechanical behaviour of the model, particularly tensile, shear and compression properties.

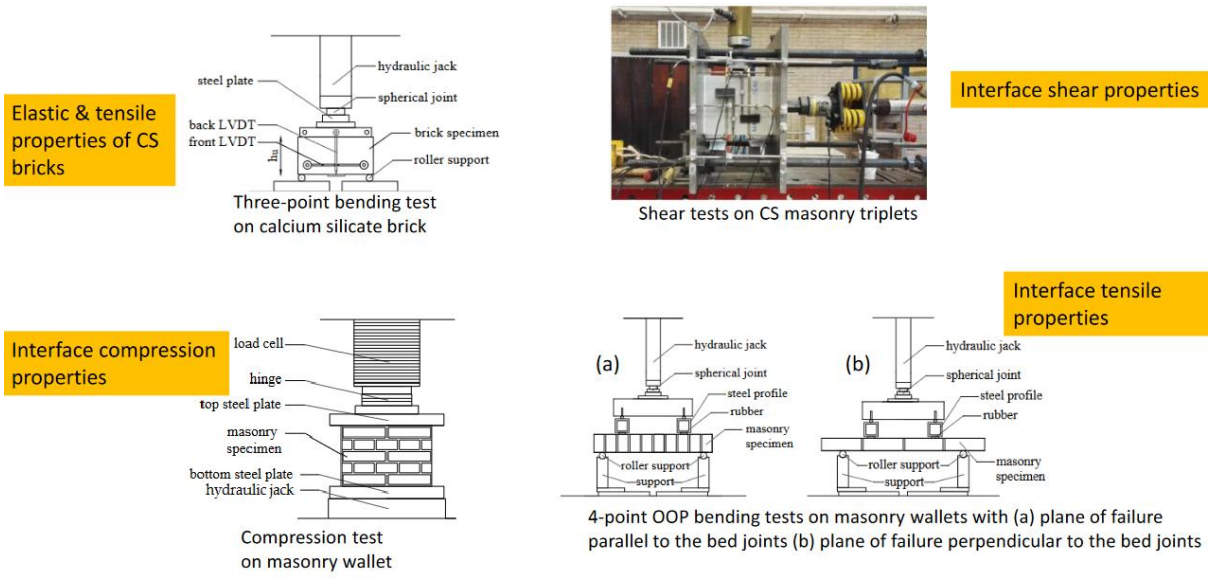

Figure 23. Small-scale tests for the calibration of the model parameters

3.3.2 Tests of IP and OOP URM walls

Quasi-static cyclic tests on single-wythe CS URM walls were conducted both in the IP and OOP direction. The characteristics of the selected tests for the validation of the numerical model can be found in Table 1. It can be observed that the IP walls were tested under different boundary conditions (double clamped or cantilever) and different magnitudes of initial vertical pressure was applied at their

top. However, the two tests performed in the OOP direction are only differentiated by the presence of an eccentric opening for TUD_COMP-12. The OOP walls were tested in two-way bending with clamped top and bottom edges and pinned vertical edges. The sketches of the test set-up used for the IP test and OOP tests can be observed in Figure 24 and Figure 25, respectively. Regarding the loading procedure for IP walls, initially a vertical pressure was applied followed by a horizontal imposed displacement at the top of the wall. In the case of OOP walls, a system of coupled airbags on both sides of the wall is used to provide a uniform lateral loading condition. Both tests were performed in displacement control. However, it should be noted that for the OOP walls, the amount of pressure was increased at each cycle until the target cycle displacement was reached. Further details of the IP tests and OOP tests can be found in Ravenshorst & Messali (2016a) and Ravenshorst & Messali (2016b), respectively.

Table 1. Characteristics of the IP and OOP tests of CS masonry walls

Wall	**Type of test**	**Dimensions (mm) L x H x t**	**Boundary conditions**	**Vertical pressure (MPa)**
TUD_COMP-4	IP cyclic	4000x2760x102	Double clamped	0.50
TUD_COMP-5	IP cyclic	4000x2760x102	Double clamped	0.30
TUD_COMP-6	IP cyclic	4000x2760x102	Cantilever	0.50
TUD_COMP-11	Two-way OOP cyclic	3874x2765x102	top & bottom edges: clamped vertical edges: pinned	0.05
TUD_COMP-12 (with opening)	Two-way OOP cyclic	3986x2764x102	top & bottom edges: clamped vertical edges: pinned	0.05

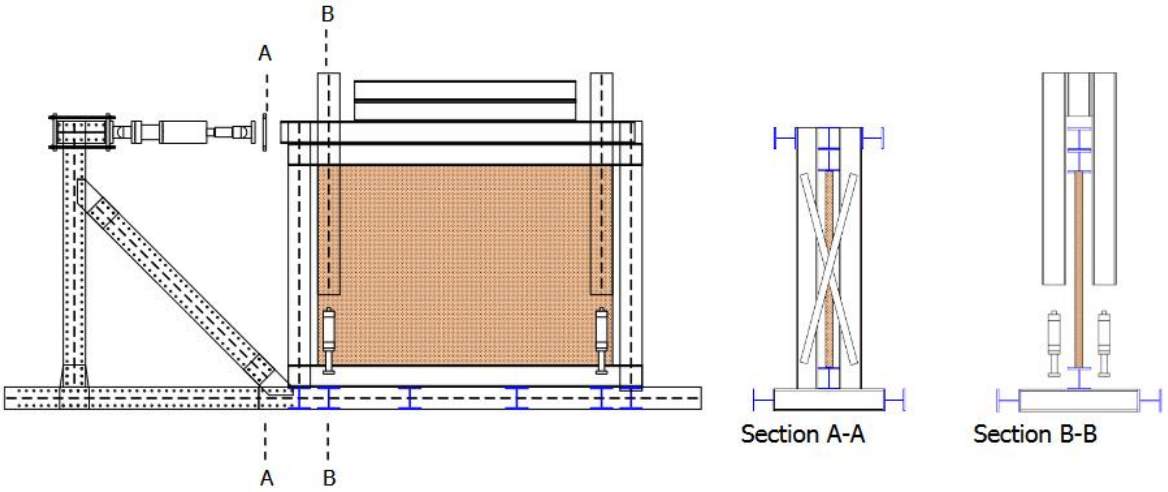

Figure 24. Sketch of the test set-up used for the IP tests

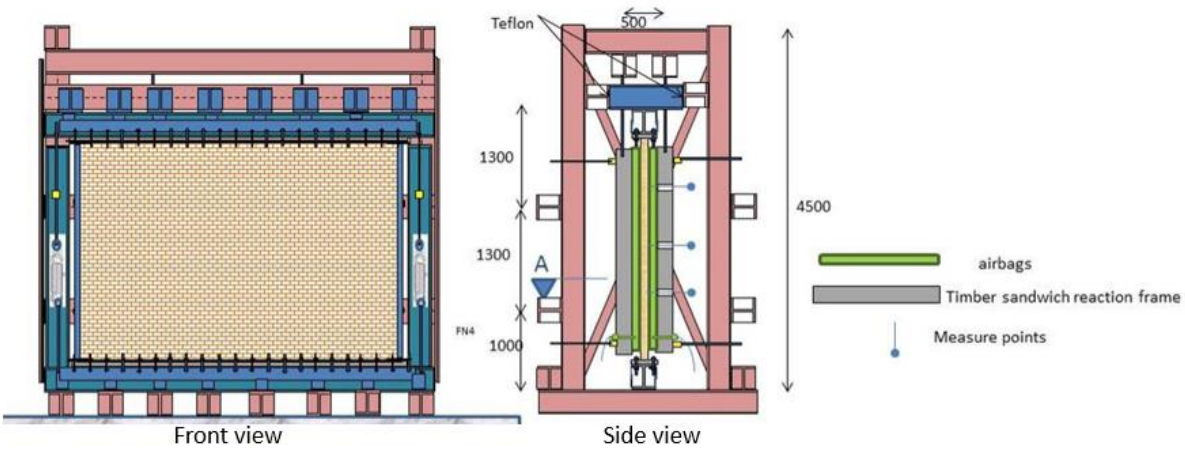

Figure 25. Sketch of the test set-up used for the OOP tests

Chapter 4 Calibration of the model input parameters

In this chapter, the mechanical input parameters for the numerical model are calibrated based on small scale tests. The list of the input parameters can be observed in Table 2. The bricks-related parameters are calibrated from a three-point bending test on CS brick. The interface related parameters representing the mortar joints are calibrated based on four-point bending test on masonry wallets (tensile properties), shear tests on masonry triplets (shear properties) and compression test on masonry wallets (compressive properties). The stiffness properties of the interface elements are determined using the formulas available in the literature brought in Equations 1 and 2. The stiffness properties related to the tensile cracking of the blocks should be such that the initial deformation of the interface is negligible compared to the deformation of the blocks due to highly brittle nature of this failure mode. The {Eq.1} is used to calculate the normal and shear stiffness related to the cracking of the blocks. For the interface element representing the mortar joints, the stiffness properties are determined using {Eq.2}, as proposed by Lourenco and Rots (1997). The calibration process is explained shortly for each test in the following paragraphs.

$$Normal\ stiffness\ (k_{nn}) = 1000 * \frac{E_{unit}}{l_e}\ ;\ Shear\ stiffness(k_{ss}) = \frac{k_{nn}}{2(1+\nu)} \qquad \{Eq.1\}$$

$$Normal\ stiffness\ (k_{nn}) = \frac{E_{unit} * E_{mortar}}{t_{mortar} * (E_{unit} - E_{mortar})}\ ;\ Shear\ stiffness(k_{ss}) = \frac{k_{nn}}{2(1+\nu)} \qquad \{Eq.2\}$$

In the above equations E is the elastic modulus, l_e is the characteristic length of the finite element, ν is the Poisson's ratio and t is the mortar thickness.

Table 2: Input parameters of the numerical model

	Parameter	Symbol	Unit
Bricks	Density	ρ	*kg/m³*
	Poisson's ratio	ν	
	Elastic modulus	E_b	*MPa*
Interface representing vertical tensile cracks in bricks	Normal stiffness	k_{nn}	*N/mm³*
	Shear stiffness	k_{ss}	*N/mm³*
	Tensile strength	$f_{t,b}$	*MPa*
	Fracture energy	$G_{f,b}^{I}$	*N/mm*
Interface representing the mortar joints	Normal stiffness	k_{nn}	*N/mm³*
	Shear stiffness	k_{ss}	*N/mm³*
	Tensile strength	f_t	*MPa*
	Mode-I fracture energy	G_f^I	*N/mm*
	Initial shear strength	$f_{v,0}$	*MPa*
	Internal friction angle	φ	*degree*
	Residual friction angle	φ_r	*degree*
	Mode-II fracture energy	G_f^{II}	*N/mm*
	Compressive strength	f_c	*MPa*
	Compressive fracture energy	$G_{f,c}$	*N/mm*

4.1 Tensile properties of CS bricks

A displacement-controlled three-point bending test is considered for the calibration of the tensile properties of CS bricks. The dimensions of the brick (identical for every other test) and the finite element model with boundary conditions can be observed in Figure 26(a). In the model the brick is

assembled using two half bricks connected by a vertical line interface element in the middle of the brick. The experimentally determined elastic modulus and tensile strength (generally taken as 2/3 of the flexural strength) are directly implemented in the numerical model. Fracture energy is considered to be 3.8% of the tensile strength, as suggested by Jafari (2021). It can be observed in Figure 26(b) that the peak force is in good agreement with the experimental results. However, the stiffness of the force-displacement diagram is arguable. This can be rectified by a large variation in elastic modulus of the CS bricks, Table 3. Further, the bricks showed brittle failure mechanism after reaching the maximum tensile strength during experiments. However, in the numerical solution there is no instant drop of the force after reaching the peak, since softening is assumed in the interface model. Table 4 shows the experimental and numerical values of the parameters associated to the tensile behaviour of CS bricks.

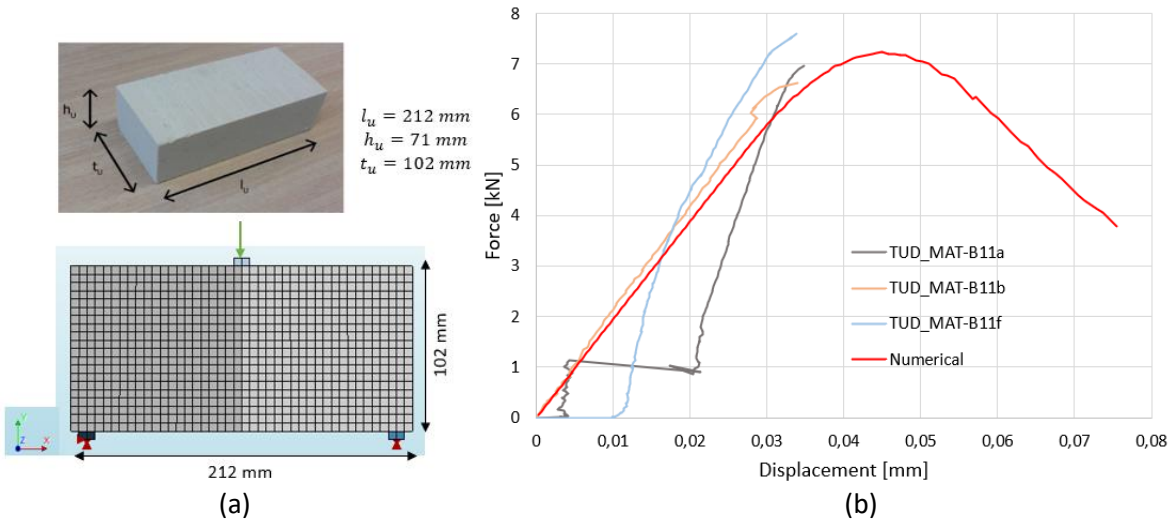

Figure 26. Three-point bending test on CS brick (a) brick dimensions and finite element model; (b) experimental-numerical force-displacement curve

Table 3: Elastic modulus [in MPa] from the experiments

TUD_MAT-B11a	TUD_MAT-B11b	TUD_MAT-B11c	TUD_MAT-B11d	TUD_MAT-B11e	TUD_MAT-B11f	Average
14080	5184	8397	9921	6137	10221	8990

Table 4. Experimental and numerical values of the parameters for the tensile behaviour of CS brick

Parameters	Experimental	Numerical
Elastic modulus (MPa)	8990	9000
Flexural strength (MPa)	2.74	-
Tensile strength (MPa)	-	1.83
Fracture energy (N/mm)	-	0.07

4.2 Interface shear properties

The shear properties of the interface elements are calibrated based on displacement-controlled shear tests of CS masonry triplets, Figure 27(a). An impression of the finite element model showing boundary conditions and the loading scheme of the specimen is depicted in Figure 27(b). Steel plates are tied to the specimen to apply a uniform distribution of the load. Further, the out-of-plane deformations are restrained at the edges. Multiple experiments considering three different levels of lateral pre-compression (0.2 MPa, 0.6 MPa & 1.0 MPa) were conducted to characterize the shear related mechanical properties of CS masonry. The average values of these properties from the experiments

are directly implemented in the numerical model and the response is reported in terms of shear stress-displacement curves of Figure 27(e). In order to better fit the response of the numerical simulation to the experimental tests, the parameters internal friction angle and residual friction angle were increased by 2°. Moreover, the Mode-II fracture energy is calibrated to better approximate the post-peak behaviour. A summary of the calibrated parameters and the experimental values is depicted in Table 5.

Figure 27(e) shows a good agreement between the numerical and experimental shear stress-displacement curve, especially for the case of 0.2 MPa pre-compression. The initial stiffness and the peak shear stress is approximated remarkably by the numerical model. Also, the post-peak behaviour is in good agreement with the experiment. However, with increasing levels of pre-compression the accuracy of the approximation slightly decreases. Moreover, it can be observed from both the experimental and numerical curves that the friction dominates over the cohesion for high levels of pre-compression. This could be because of the premature crushing of the particles (in the experiment) at high pre-compression. Further, the shear displacements and tractions in the interfaces for 0.6 MPa vertical pre-compression are shown in Figure 27(c) and Figure 27(d), respectively. It is observed that the shear displacements and tractions are uniformly distributed over the thickness of the element, which shows that the response is purely in-plane.

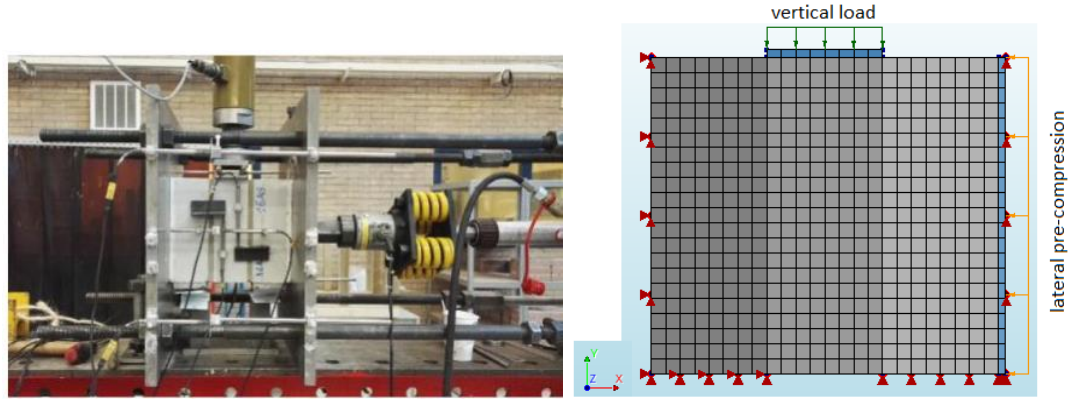

(a) (b)

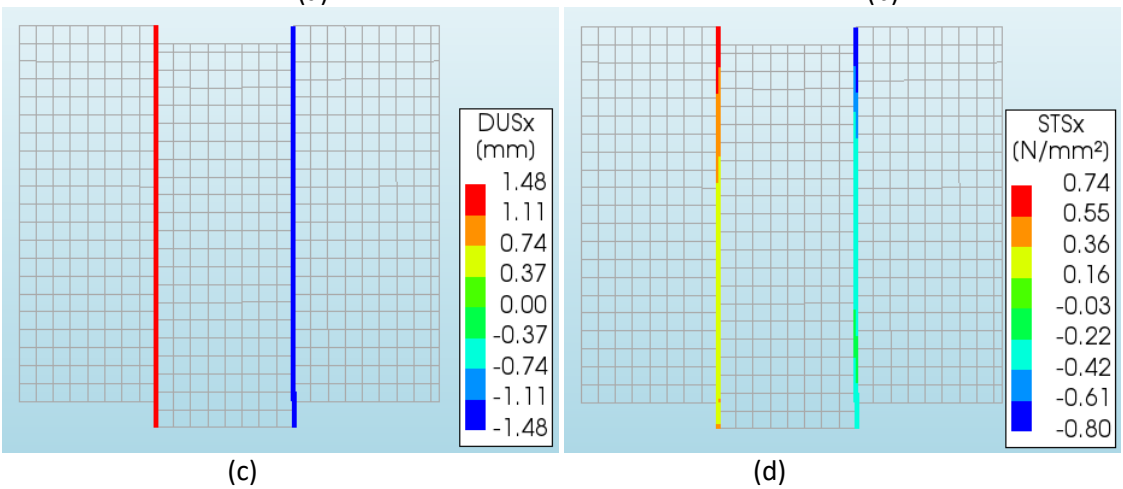

(c) (d)

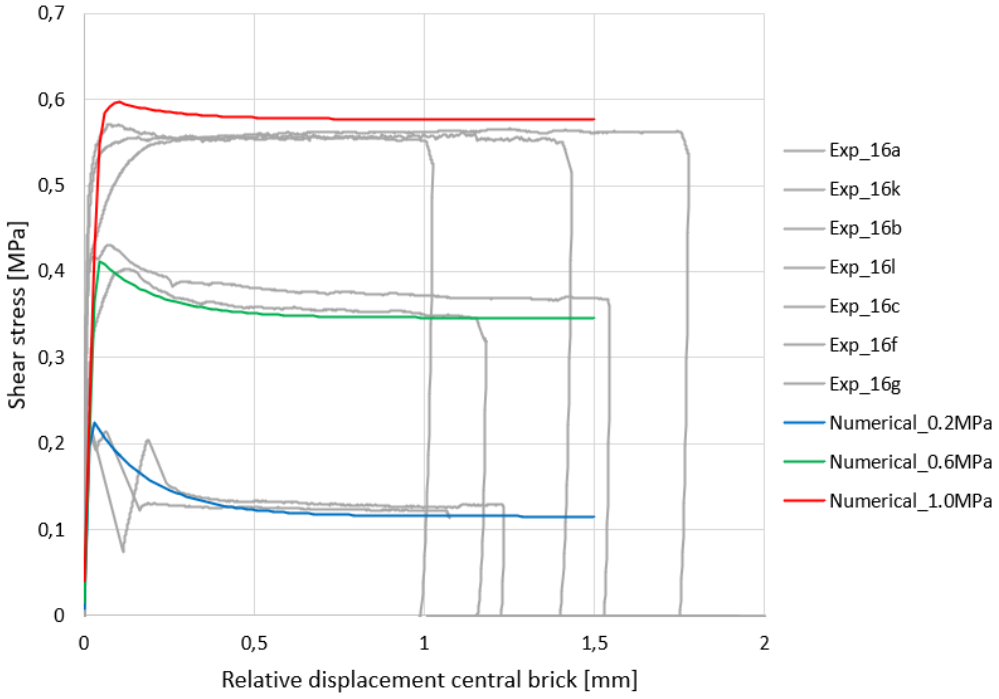

(e)

Figure 27: Shear test on CS masonry triplets (a) Experimental set-up; (b) Finite element model;(c)-(d) Shear displacements and tractions in each layer along the thickness of the interfaces for 0.6 MPa vertical pre-compression taken at the end of the analysis (deformation scaling factor = 10); (e) Experimental-numerical shear stress-displacement curve for three different levels of pre-compression

Table 5: Experimental and numerical values of the parameters for the shear behaviour of CS masonry

Parameters	**Experimental**	**Numerical**
Initial shear strength (MPa)	0.14	0.14
Internal friction angle	23°	25°
Residual friction angle	28°	30°
Mode-II fracture energy (N/mm)	-	0.025

4.3 Interface compression properties

Displacement controlled compression tests on masonry wallets (434x476x102-mm), where the loading is perpendicular to the bed joints, are used to calibrate the compressive properties of the interface element. Particularly, the parameters compressive strength and fracture energy are of importance. The experimentally obtained values of the compressive strength and the fracture energy are directly implemented in the model. It should be noted that the fracture energy determined in the experiment is the total compressive fracture energy and is calculated as the area underneath the stress-strain diagram, taking the height of the specimen into account. However, in the numerical model the fracture energy is characterized by the characteristic length of the element i.e., mesh size. So, the compressive fracture energy for the numerical model is determined as follows.

$$G_c = G_c^T * \frac{l_e}{l_s}$$

Where, G_c is the compressive fracture energy of a finite element, $G_c^T (= 20 N/mm)$ is the total fracture energy derived from the experiment, $l_s (= 434\ mm)$ is the total length of the specimen and $l_e (= 55\ mm)$ is the characteristic length of the element. The finite element model with the meshing and

the boundary conditions can be observed in Figure 29(a). For the mesh size of $55mm \times 40mm$, as considered in this model, G_c is equal to $2.5\ N/mm$. This value is adjusted to $3.0\ N/mm$ to obtain numerical results close to the experiment.

Figure 28 shows an excellent agreement between the numerical and experimental normal stress-strain curve. During the experiment it could be observed that cracks started at the brick-mortar interface in the bed joints and developed further in the formation of vertical cracks in the bricks, Figure 29(b). Since no compressive failure of the shell elements is assumed in the numerical model, the failure of the specimen occurs due to crushing of the interfaces distributed uniformly over all bed joints, as can be observed in Figure 29(c). When weakening one of the bed joints, for instance by reducing 20% of the maximum compressive strength, the failure is then localized particularly to that bed joint. Further, the response is uniformly distributed along the thickness of the specimen, as shown in Figure 29(c), where the interface normal relative displacements are equal for every layer. The calibrated numerical and experimental parameters describing the compressive behaviour of the CS masonry are presented in Table 6.

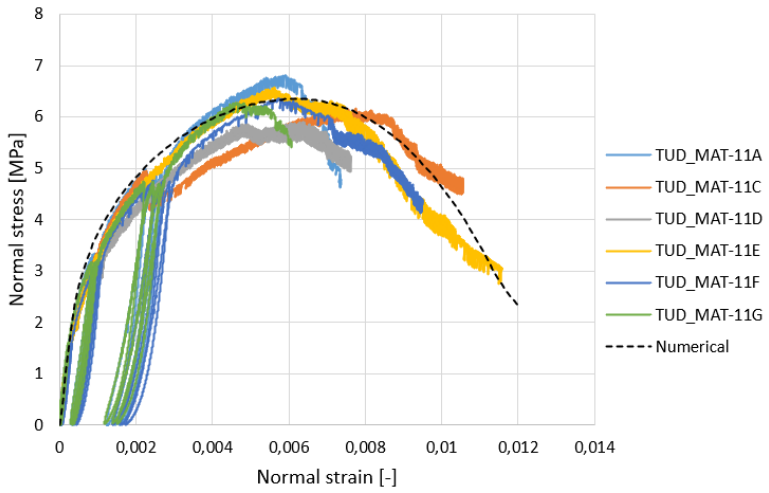

Figure 28: Experimental-numerical stress-strain curve of vertical compression test

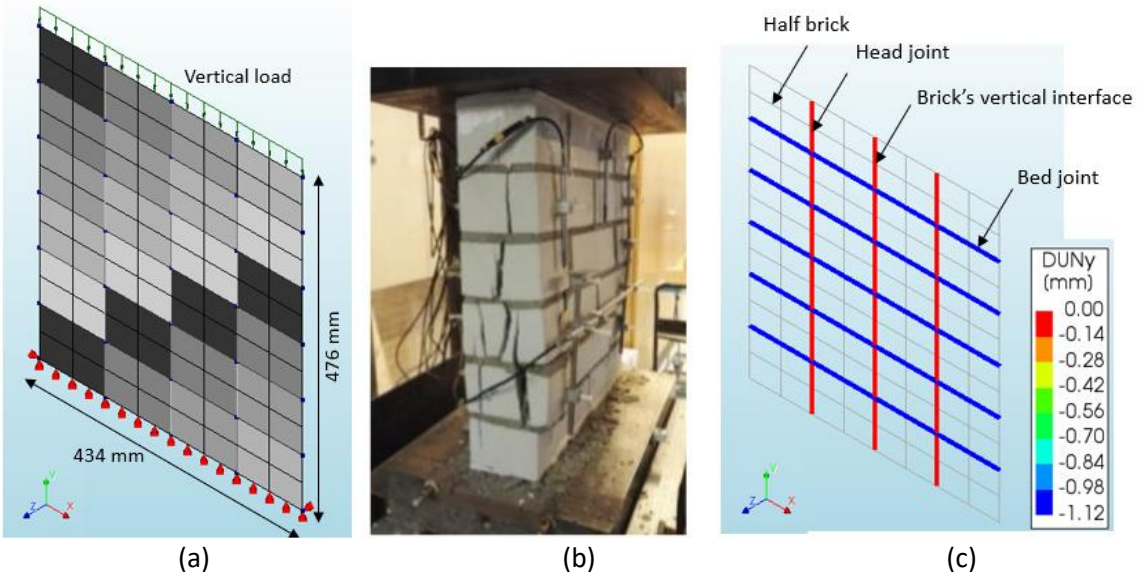

Figure 29: Vertical compression test on CS masonry wallet (a) finite element model; (b) crack pattern observed during the experiment; (c) interface relative normal displacements in each layer at the end of the numerical analysis.

Table 6: Experimental and numerical values of the parameters for the compressive behaviour of CS masonry

Parameters	**Experimental**	**Numerical**
Compressive strength (MPa)	6.35	6.35
Fracture energy (N/mm)	20	3.0

4.4 Interface tensile properties

The interface tensile properties, namely the tensile strength and the fracture energy, are derived from the bending tests on CS masonry wallets in displacement control. For this purpose, the four-point bending test with the moment vector parallel to the bed joints and in the plane of the wall, which generates a plane of failure parallel to the bed joints, is considered. The test set-up and the finite element model with boundary conditions can be visualized in Figure 30(a) and Figure 30(b), respectively. The results from the tests in terms of load-displacement curves are presented in Figure 30(c). It follows from the experiment that the average flexural strength, calculated as the ratio of maximum bending moment divided by the section modulus, is equal to 0.21 MPa with the variation coefficient of 0.25. However, the interface model requires the tensile strength of the masonry as input parameter. Therefore, initially the interface tensile strength is assumed to be 2/3 of the flexural strength and the fracture energy is equal to 5% of the interface tensile strength, as suggested by Jafari (2021). Figure 30 shows that these initial values overestimate the peak force compared to the experimental results. Hence, the interface tensile strength is calibrated to 0.10 MPa which provides peak force close to the average of the experiment. Further, it can be observed that the initial stiffness of the force-displacement curve is within the range of the experiment. The experimental and numerical parameters associated with the tensile behaviour of the CS masonry are presented in Table 7.

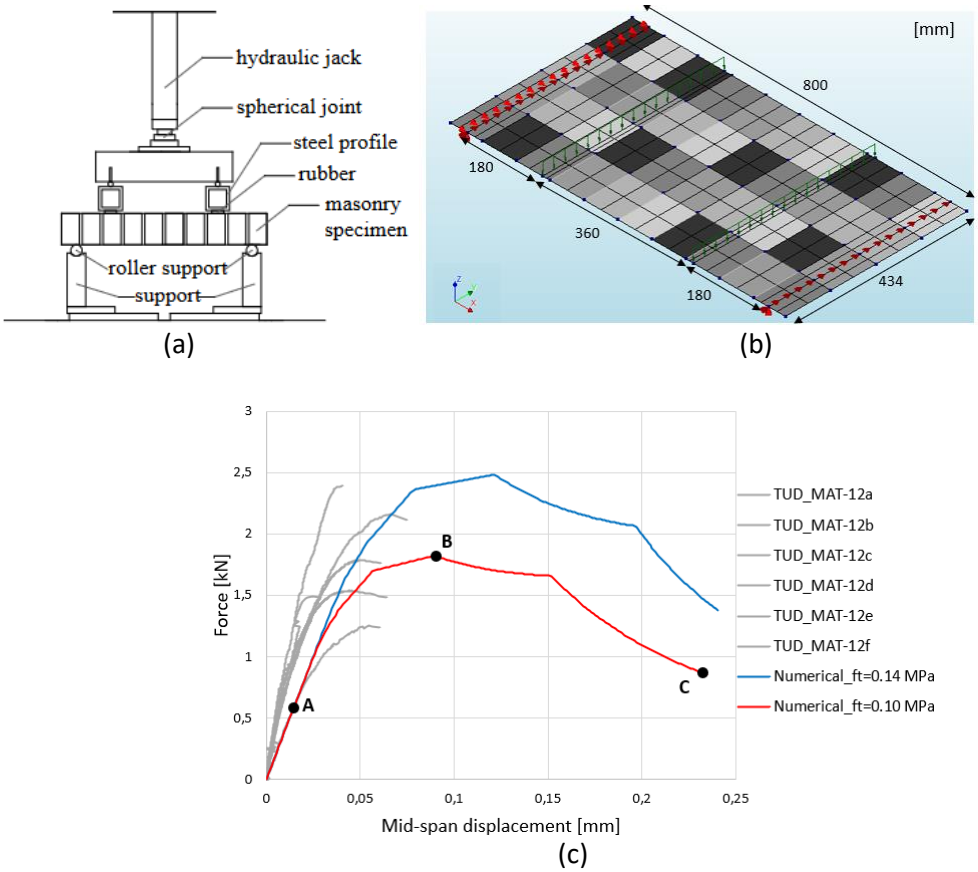

Figure 30: Four-point bending test on CS masonry with a plane of failure parallel to the bed joints (a) test set-up; (b) finite element model with dimensions; (c) experimental-numerical force-displacement curve

Table 7: Experimental and numerical values of the parameters for the tensile behaviour of the CS masonry

Parameters	Experimental	Numerical
Flexural strength (MPa)	0.21	-
Tensile strength (MPa)	-	0.10
Fracture energy (N/mm)	-	0.005

Regarding the failure pattern of the specimens, all of them showed brittle failure mechanisms during the experiment. The specimens cracked in bed joints located in constant moment zone, as observed in Figure 31(a). This is also the case for the numerical model. The failure of the specimen is localized in two bed joints, near to the location where the load is applied, Figure 31(b). Further, how the stresses and displacements in these bed joints are distributed in seven different layers along the thickness of the element can be observed in Figure 32. This is done for three different load levels from the force-displacement curve, as shown in Figure 30(c). Load level A represents the elastic state by considering 1/3 of the peak load. Load level B is at the peak load, whereas Load level C represents the end of the analysis. Layer 1 is the outer layer in tension and has the maximum interface opening as expected. A linear distribution of the stresses is observed for load level A. For load level B, the first five layers have reached the maximum interface tensile strength, whereas layer 6 and layer 7 are in compression. Since tensile softening of the interface is considered in the numerical model, in load level C, layer 6 is in the softening regime and has not yet reached the tail of its exponential tensile response curve. Hence, tensile tractions at this layer are observed.

In this report, shell elements are used to simulate the bending behaviour of the masonry. Therefore, it is of interest to see how the number of integration points over the thickness of the element influences the force-displacement curve. Generally, the 7-point integration scheme is sufficient to capture bending, when using shell elements. This is also observed in Figure 33, where increasing the number of integration points only smoothens the curve in the post-peak regime and has no influence on the magnitude of the load capacity. Therefore, this report also uses the 7-point integration scheme.

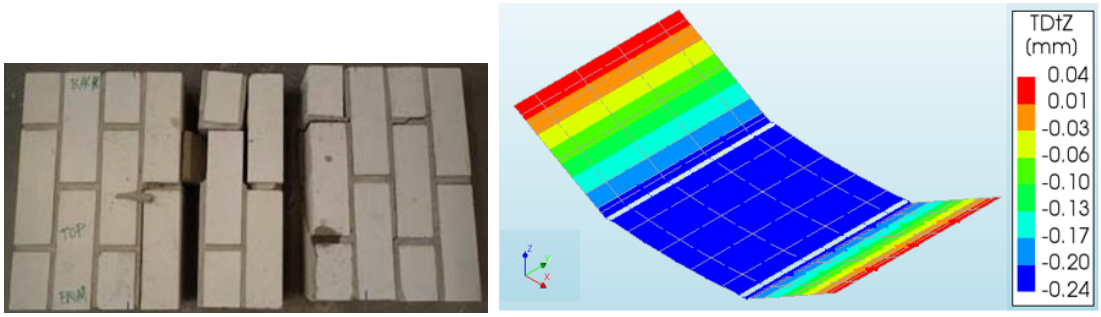

(a) (b)

Figure 31: Failure pattern from the 4-point bending test with a plane of failure parallel to the bed joints (a) top-view of the specimen showing experimental crack pattern; (b) the OOP deformation of the specimen at the end of the numerical analysis (scaling factor = 500)

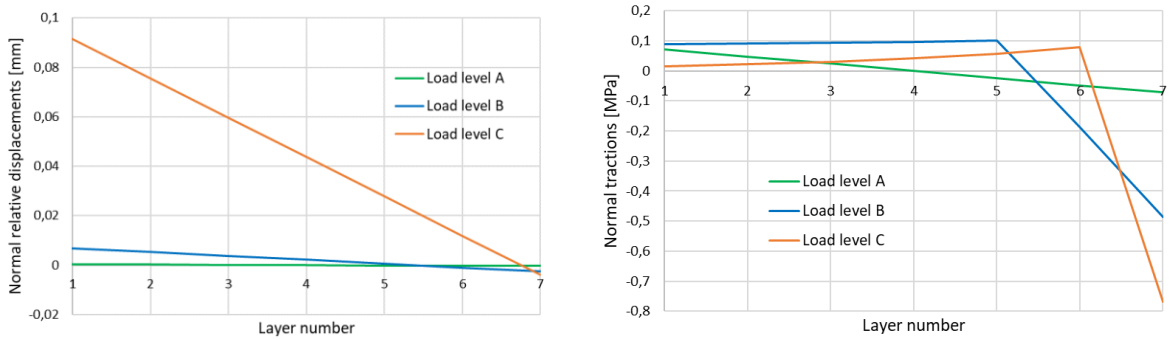

Figure 32: Interface opening (left) and stresses (right) along the thickness of the element in the cracked bed joints

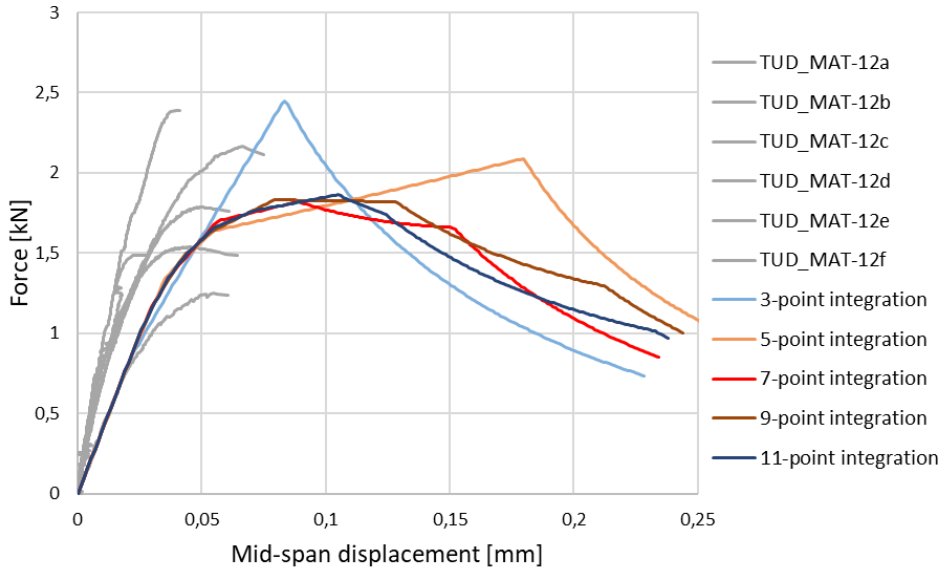

Figure 33: Influence of integration scheme along the thickness of the element

During this experimental campaign, two other bending tests on CS masonry wallets were also conducted to consider the orthotropic behaviour of the masonry. The four-point OOP bending test with a plane of failure perpendicular to the bed joints and the in-plane vertical bending test are illustrated in Figure 34. The calibrated parameters from the previous bending test are used in the numerical simulation of these two tests and the results are compared with the experiment. Figure 35 shows a good agreement between the numerical results and the experiment. The predicted peak force and the stiffness of the curve lies in between the experimental results. Both in the experimental and numerical outcomes, typical stepwise crack pattern for the masonry (cracking in both bed and head joints) could be observed. The deformation behaviour of these tests is shown in Figure 36 and Figure 37.

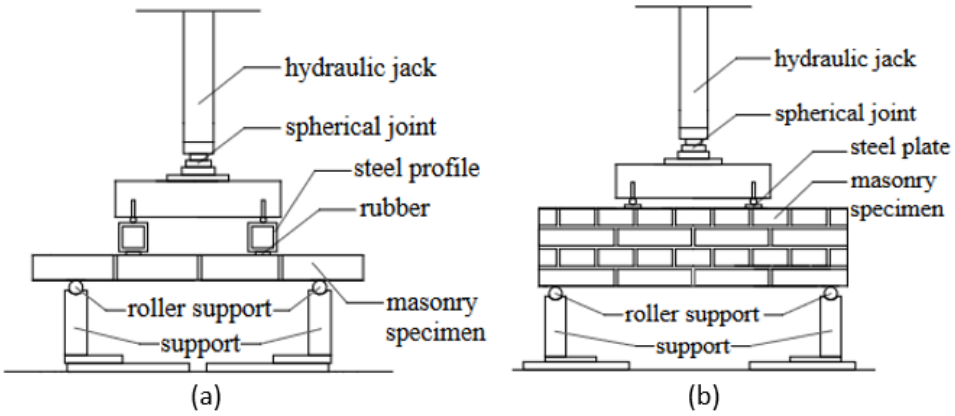

Figure 34: Four-point bending tests on CS masonry (a) OOP bending test with a plane of failure perpendicular to the bed joints (b) in-plane bending test (Esposito et al., 2016)

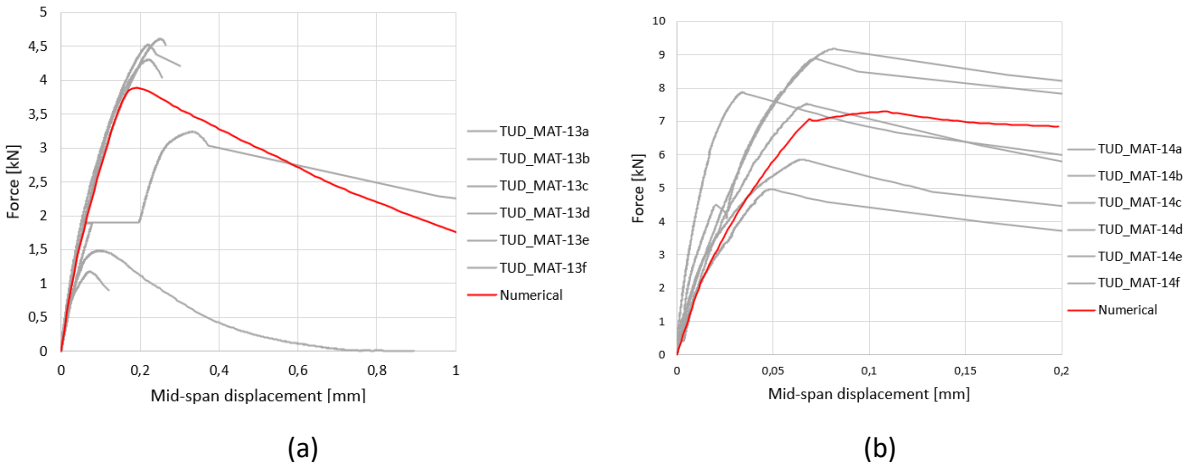

Figure 35: Experimental-numerical force-displacement curve of CS masonry from (a) OOP bending test with a plane of failure perpendicular to the bed joints (b) in-plane bending test

Figure 36: Crack patterns observed in the experiment for (a) OOP bending test with a plane of failure perpendicular to the bed joints (b) in-plane bending test (Esposito et al., 2016)

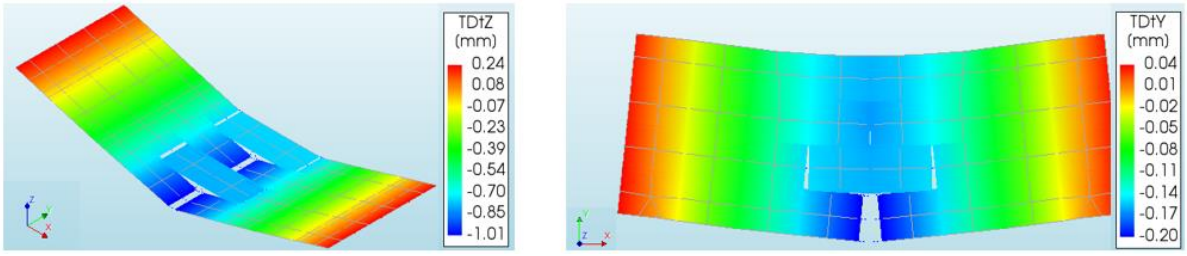

(a) (b)

Figure 37: Deformation of the tests at the end of the numerical analysis (a) OOP bending test with a plane of failure perpendicular to the bed joints (scaling factor 100); (b) in-plane bending test (scaling factor 200)

4.5 Overview of the calibrated input parameters from small-scale tests

Table 8 gives an overview of the calibrated input parameters that can be directly used in the validation of IP and OOP walls. Referring to the previous sections, the input parameters, namely the E-modulus and tensile strength of the bricks, and the initial shear strength and compressive strength for the interface representing the mortar joints are directly derived from the experiments, while the tensile strength and internal and residual friction angle for the interface representing the mortar joints are slightly calibrated for better matching the experiments.

Table 8: Overview of the calibrated input parameters for CS masonry based on small-scale tests

	Parameter	**Symbol**	**Unit**	**Value**
Bricks	Density	ρ	*kg/m³*	1700
	Poisson's ratio	ν		0.14
	Elastic modulus	E_b	*MPa*	9000
Interface representing the vertical tensile crack in bricks	Normal stiffness	k_{nn}	*N/mm³*	136000
	Shear stiffness	k_{ss}	*N/mm³*	59000
	Tensile strength	$f_{t,b}$	*MPa*	1.83
	Fracture energy	$G_{f,b}^{I}$	*N/mm*	0.07
Interface representing the mortar joints	Normal stiffness	k_{nn}	*N/mm³*	191
	Shear stiffness	k_{ss}	*N/mm³*	84
	Tensile strength	f_t	*MPa*	0.10
	Mode-I fracture energy	G_f^I	*N/mm*	0.005
	Initial shear strength	$f_{v,0}$	*MPa*	0.14
	Internal friction angle	φ	*degree*	25
	Residual friction angle	φ_r	*degree*	30
	Mode-II fracture energy	G_f^{II}	*N/mm*	0.025
	Compressive strength	f_c	*MPa*	6.35
	Compressive fracture energy	$G_{f,c}$	*N/mm*	3.0

Chapter 5 Model validation against full-scale wall tests

5.1 Introduction

In this chapter, the numerical model is validated against full-scale wall tests using previously calibrated mechanical parameters based on small-scale tests. The validation is done separately for the IP and OOP loading. Referring to section 3.3.2, three IP tests and two OOP tests, performed at the TU Delft are selected for the validation. It should be noted that the numerical simulation of the walls in this report is limited to monotonic pushover analysis, although the tests performed in the experiment are cyclic. This is because the adopted CCSC material model does not perform well under cyclic load, as explained in section 3.2.2.

5.2 Validation against in-plane loaded walls

Finite element model

A sketch of the finite element model for the IP loaded walls is shown in Figure 38. The wall is composed of half bricks (111x84-mm) connected with zero-thickness interface elements and has the mesh properties as illustrated in Figure 38. Further, the applied boundary conditions for three different IP loaded walls are given in Table 9. The walls TUD_COMP-4 and TUD_COMP-5 are loaded in double clamped configuration, whereas the wall TUD_COMP-6 is loaded in cantilever configuration. Note that the vertical displacement of the wall at the top is set free to apply the initial vertical pressure.

The load is applied in displacement control, similar to the experiment. First, the self-weight and the vertical pressure are applied in two sequential steps. Then, a horizontal prescribed displacement is applied at the top left corner of the wall. For this purpose, a steel beam is embedded to the top edge of the wall that simulates the effect of the steel beam glued to the wall in the experiment. The L13BE element is used for the steel beam which is a 2-node, 3D class-II beam element and has three translational- and three rotational degrees of freedom in the nodes. Note that the vertical load is applied on the top of this beam and not directly to the wall. For the first two loading steps, regarding the self-weight and the vertical pressure, the Newton-Raphson iterative method is used, whereas in the case of horizontal loading the Quasi-Newton iterative method is applied. The maximum number of iterations for Quasi-Newton is set to 1000. Either the displacement or the force norm should be satisfied for the convergence. The tolerance norm is chosen to be 0.01 (default values in DIANA) for both norms. Both the physical and geometrical nonlinear effects are considered in the analysis.

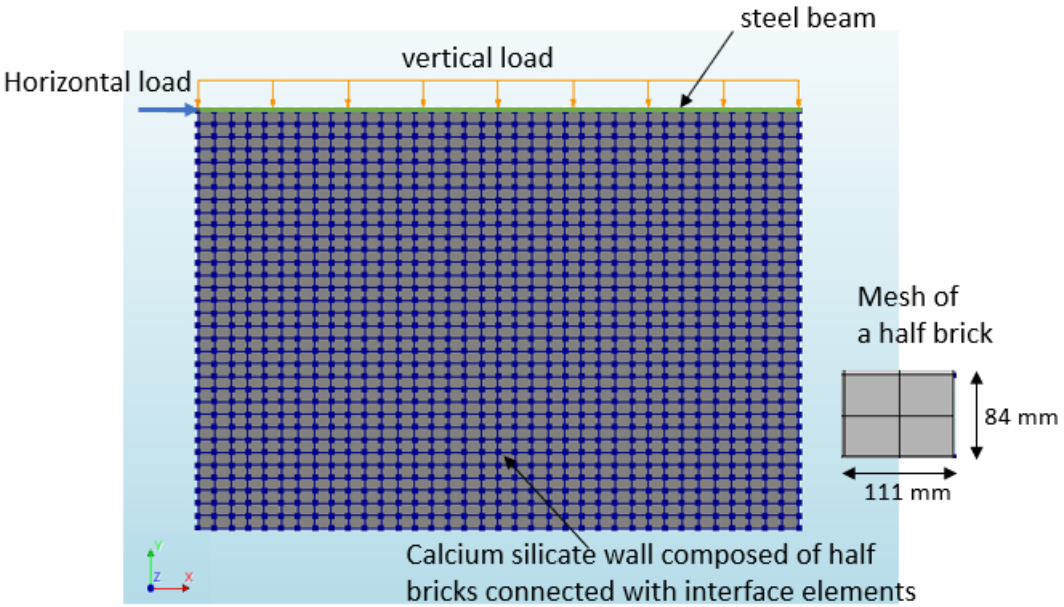

Figure 38. Finite element model for IP loaded walls

Table 9: Restrained degrees of freedom for three different IP loaded walls

Wall	Top edge	Bottom edge
TUD_COMP-4	$u_z, \varphi_x, \varphi_y, \varphi_z$	$u_x, u_y, u_z, \varphi_x, \varphi_y, \varphi_z$
TUD_COMP-5	$u_z, \varphi_x, \varphi_y, \varphi_z$	$u_x, u_y, u_z, \varphi_x, \varphi_y, \varphi_z$
TUD_COMP-6	$u_z, \varphi_x, \varphi_y$	$u_x, u_y, u_z, \varphi_x, \varphi_y, \varphi_z$

Numerical results and discussion

In this section, the numerical results are compared with the experimental results in terms of force-drift curve and the crack patterns. The force-drift curve contains the shear force on the vertical axis and the wall drift on the horizontal axis. The drift is the ratio of the horizontal displacement at the top of the wall to its height, expressed in percent. Further, the cyclic and the corresponding backbone curve from the experiment are shown in the force-drift diagram. The backbone curve is obtained by connecting the shear loads at the maximum displacement of each cycle. For the comparison of the crack patterns, the interface relative displacements (DUNy, DUSx and DUSz) are considered, since they represent the cracking, shearing and crushing of the masonry. DUNy, DUSx and DUSz are the normal displacement, the in-plane shear displacement and the out-of-plane shear displacement of the interfaces, respectively.

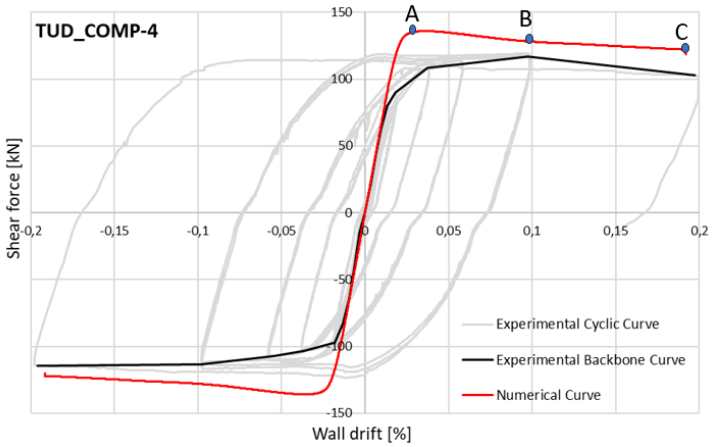

(a)

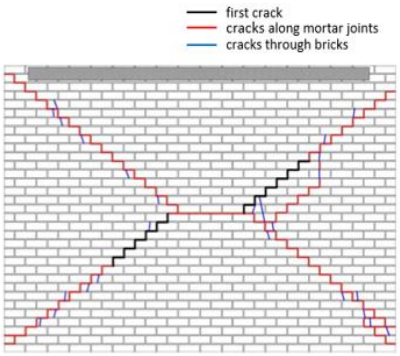

(b)

Load level	Crack opening of the interfaces	Shear sliding of the interfaces
A	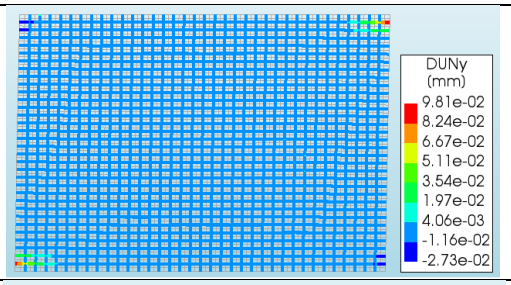	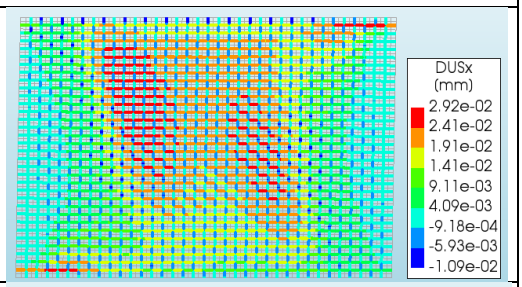
B	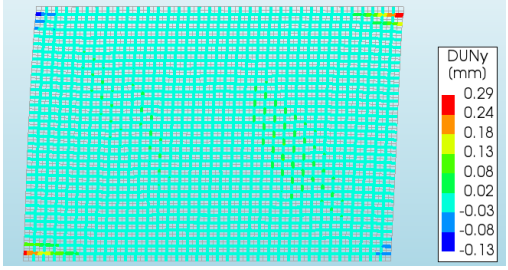	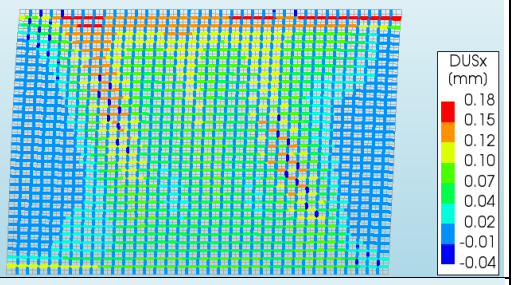
C	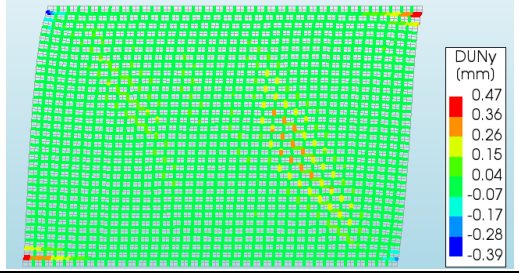	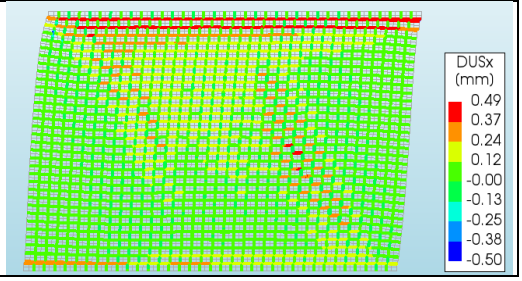

(c)

Figure 39. Numerical vs experimental comparison of TUD_COMP-4 (a) shear force vs wall-drift curve; (b) schematic view of the crack patterns observed at the end of the experiment; (c) numerical crack pattern at different load levels; deformation scaling factor=25

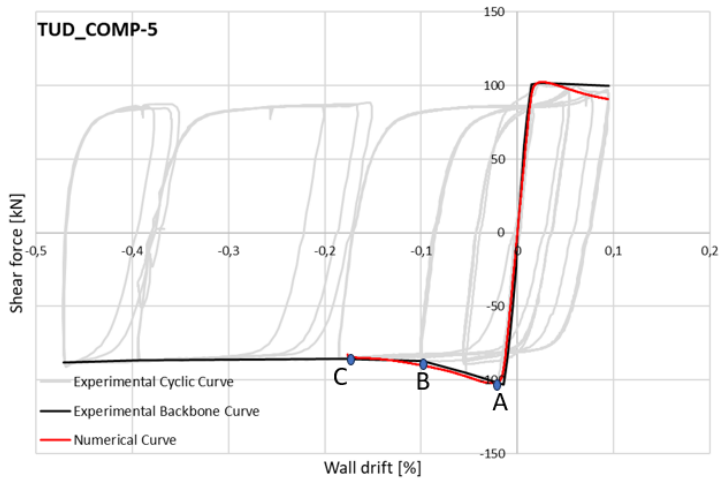

(a)

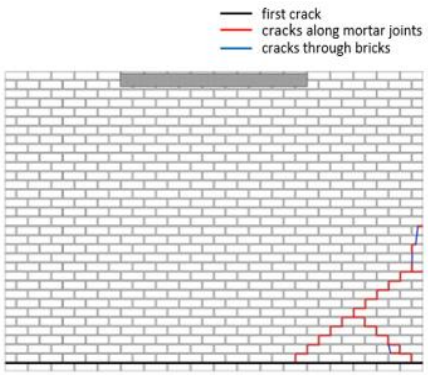

(b)

Load level	Crack opening of the interfaces	Shear sliding of the interfaces
A	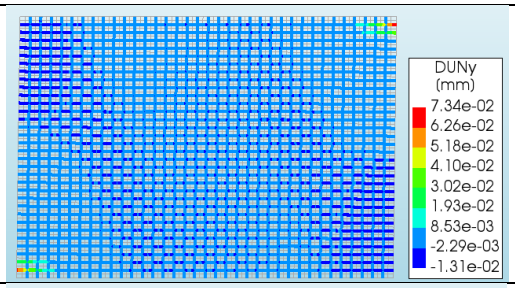	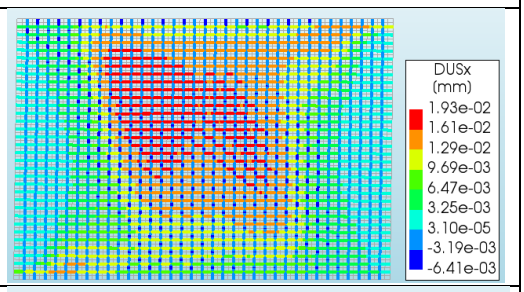
B	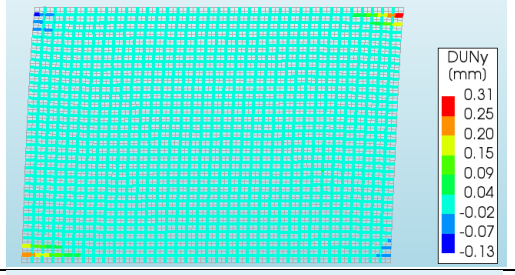	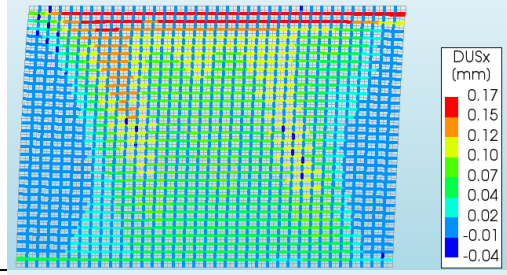
C	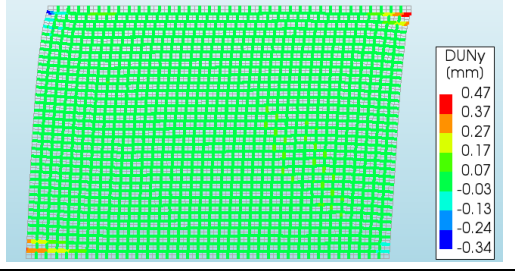	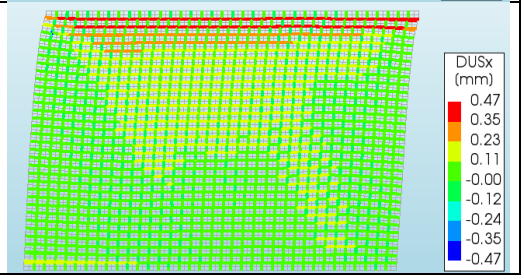

(c)

Figure 40. Numerical vs experimental comparison of TUD_COMP-5 (a) shear force vs wall-drift curve; (b) schematic view of the crack patterns observed at the end of the experiment; (c) numerical crack pattern at different load levels; deformation scaling factor=25

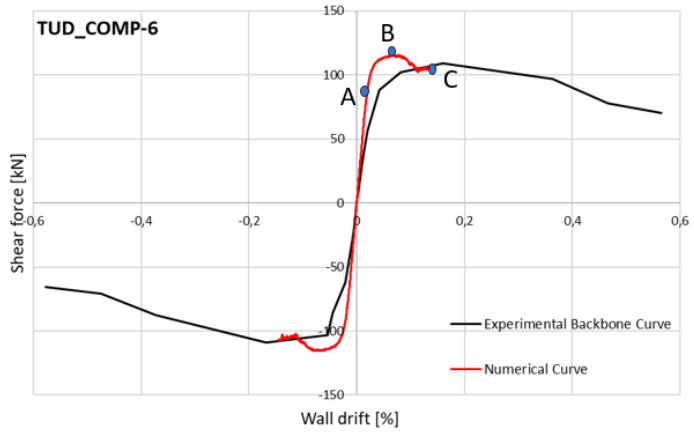

(a)

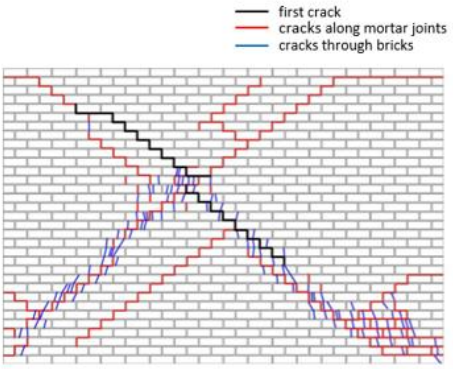

(b)

Load level	Crack opening of the interfaces	Shear sliding of the interfaces
A	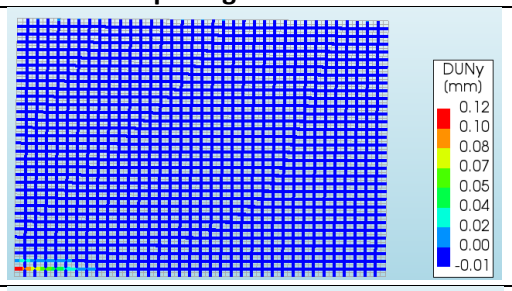	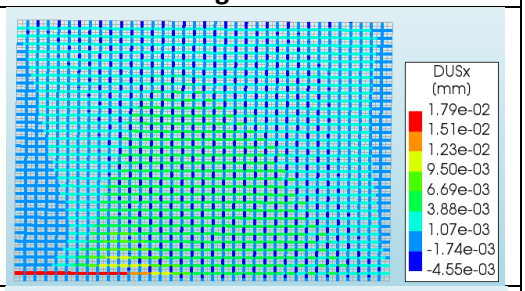
B	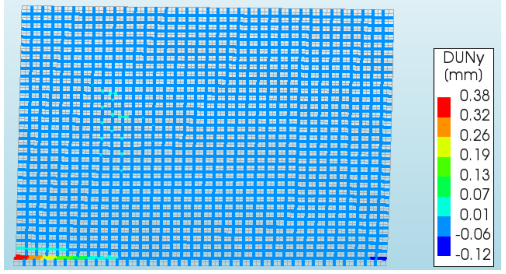	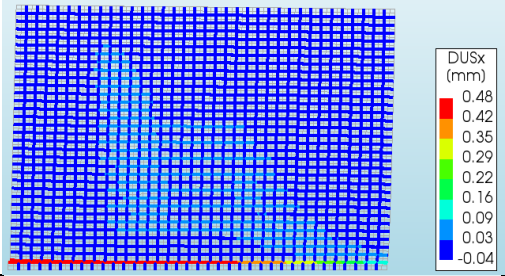
C	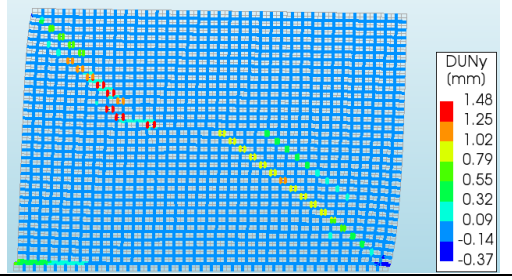	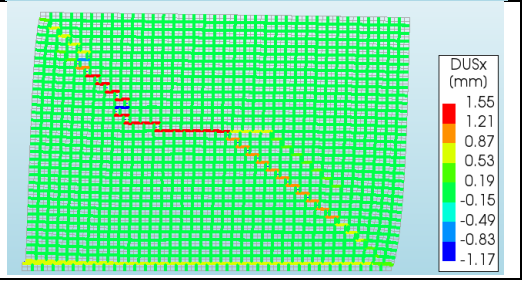

(c)

Figure 41. Numerical vs experimental comparison of TUD_COMP-6 (a) shear force vs wall-drift curve; (b) schematic view of the crack patterns observed at the end of the experiment; (c) numerical crack pattern at different load levels; deformation scaling factor=25

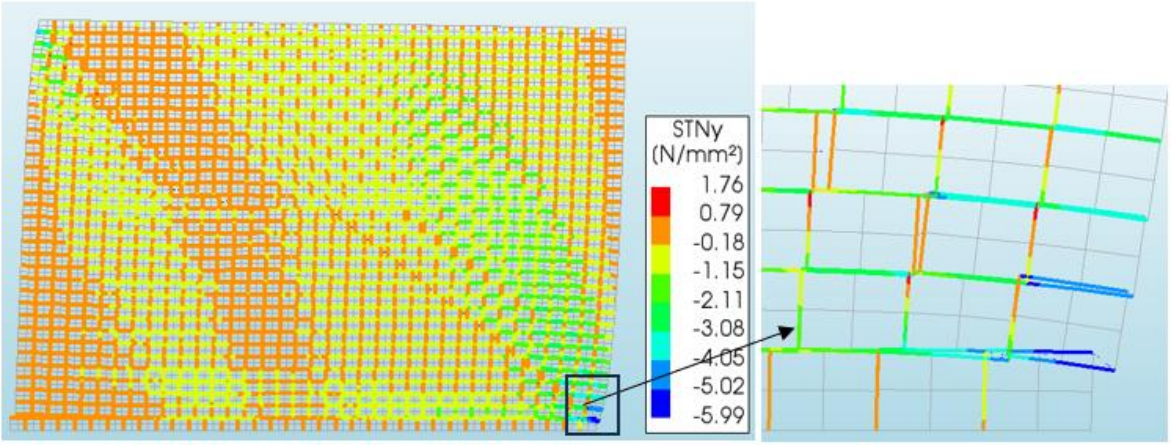

Figure 42. Interface normal tractions of TUD_COMP-6 right before the divergence

TUD_COMP-4

For TUD_COMP-4, the initial stiffness of the wall is estimated with high accuracy and the peak force is slightly overestimated, Figure 39(a). The overestimation is 12% when compared to the average of the experimental results. This can be related to the cyclic loading in the experiment and the difference in strength parameters between the experiment and the numerical model. The cyclic loading reduces the load-bearing capacity by weakening the wall gradually with each cycle. Hence, in the subsequent cycle the wall will not have the strength of an intact specimen. During the experiment, the wall failed in shear and had mostly the shear diagonal cracks along the mortar joints, Figure 39(b). The diagonal cracks developed first at the centre of the wall and then quickly expanded to the corners. The numerical results with respect to the crack evolution considering three different load levels can be observed in Figure 39(c). Similar crack pattern, mainly diagonal shear cracks, as in the experiment is also observed in the numerical simulation, especially at the end of the analysis. Further, the shear sliding behaviour is observed near to the top edge of the wall. Similar residual shear sliding behaviour was also observed at the end of the experiment. However, this type of sliding occurred in the middle part of the wall. The change of position might be due to the concentration of compressive nonlinearity in the interfaces and the use of elastic shell elements.

TUD_COMP-5

Figure 40(a) shows an excellent agreement between the experiment and the numerical results when comparing the stiffness and the maximum shear force. The predicted maximum shear force is equal to the experiment, Table 10. During the experiment, the horizontal bed joint sliding at the bottom followed by the diagonal shear cracks at the right bottom corner could be observed,Figure 40 (b). The crack patterns from the numerical simulation are shown in Figure 40(c). It is observed that the bed joint sliding occurs near to the top edge of the wall indicating towards the shear dominated behaviour. At load level C, also few openings of the bed joints at the corners of the wall can be observed, Figure 40(c).

TUD_COMP-6

For TUD_COMP-6, the predicted maximum shear force is in good agreement with the experiment, as shown in Figure 41(a) and Table 10. However, the initial stiffness of the force-drift curve is overestimated. This can be related to the change of stiffness due to some unexpected minor

movement in the test frame during the experiment, as mentioned in Ravenshorst & Messali (2016a). Further it is observed that the full analysis could not be achieved because of the divergence in the numerical simulation. This can be associated to the high compressive stresses (close to failure) in the right corner of the wall, as observed in Figure 42, which resulted in numerical instability. Besides, the numerical instability could also be due to failure of the bricks, since the stress in the brick interfaces is close to its maximum. Nevertheless, the crack patterns could be identified and compared to the experiment. Primarily, the diagonal shear cracks are observed both in the experiment and the numerical simulation, Figure 41(b) & Figure 41(c). It could be said that the numerical simulation also identifies crushing of the mortar joints and cracking of the bricks at the right corner of the wall, similar to the experiment, since stresses close to failure are observed, Figure 42.

Table 10: Experimental vs numerical shear strength

Wall	Experiment		Numerical	Difference (%)	
	V^+ (kN)	V^- (kN)	V_{num} (kN)	V^+	V^-
TUD_COMP-4	119	-123	136	14	11
TUD_COMP-5	102	-103	102	0	-1
TUD_COMP-6	110	-109	115	5	5
V^+ = positive shear strength; V^- = negative shear strength; V_{num} = predicted shear strength					

For double clamped walls, although the numerical crack patterns are slightly different from the experiment, the results are considered acceptable because the capacity of the two failure mechanisms, namely diagonal cracking and shear sliding, are close to one another. For cantilever wall, the peak force and the crack patterns are predicted well. However, the model fails to capture the response to large IP displacements, since crushing of the mortar joints and cracking in the brick interfaces cause numerical instability.

5.3 Validation against out-of-plane loaded walls

Finite element model

Two types of walls, a solid wall (TUD_COMP-11) and a wall with an opening (TUD_COMP-12 with opening area= 1790x1620 mm^2) are considered for the validation of the model for the OOP loading. The model properties regarding the composition of the wall and the mesh size are similar to that of IP loaded walls. The sketches of the two models can be observed in Figure 43 and Figure 44. A steel beam at the top is placed to avoid stress concentrations and distribute the vertical load uniformly over the wall. Further, the lintel is modelled as elastic continuum shell element with standard properties of concrete ($E = 30000\ MPa$, $\mu = 0.2$ & $\rho = 2400\ kg/m^3$).

Figure 43 and Figure 44 show the boundary and the loading conditions of TUD_COMP-11 and TUD_COMP-12, respectively. Regarding the boundary conditions of the vertical sides, the use of wooden wedges between steel and masonry, to prevent local damage to masonry, make it unclear whether the sides are fully restrained or not for the horizontal in-plane displacements. The lateral support system for the OOP walls applied in the experiments can be observed in Figure 45. Figure 46 shows that restraining the vertical sides in x-direction results in inaccurate prediction of the numerical results, high peak force compared to the experiment. Therefore, the vertical sides are only restrained in the OOP direction, as observed in Figure 43.

The analysis is performed in load control with arc length method, contrary to the experiment which was performed with an approach close to displacement-controlled method with the help of airbags on

both sides of the wall. The OOP displacement in the middle of the wall (red dots in Figure 43 and Figure 44) is considered as control point for the arc-length method. First, the self-weight and the vertical pressure are applied in two sequential steps. Then the OOP load is applied in terms of uniform pressure on the face of the wall. Note that for the wall with opening, the masonry above and below the opening are not loaded, as shown in Figure 44. Similar to the IP walls, the Newton-Raphson iterative method is used for the first two loading steps and the Quasi-Newton iterative method is applied for the OOP loading. The maximum number of iterations for Quasi-Newton is set to 1000. Either the displacement or the force norm should be satisfied for the convergence. The tolerance norm is chosen to be 0.01 (default values in DIANA) for both norms. Both the physical and geometrical nonlinear effects are considered in the analysis.

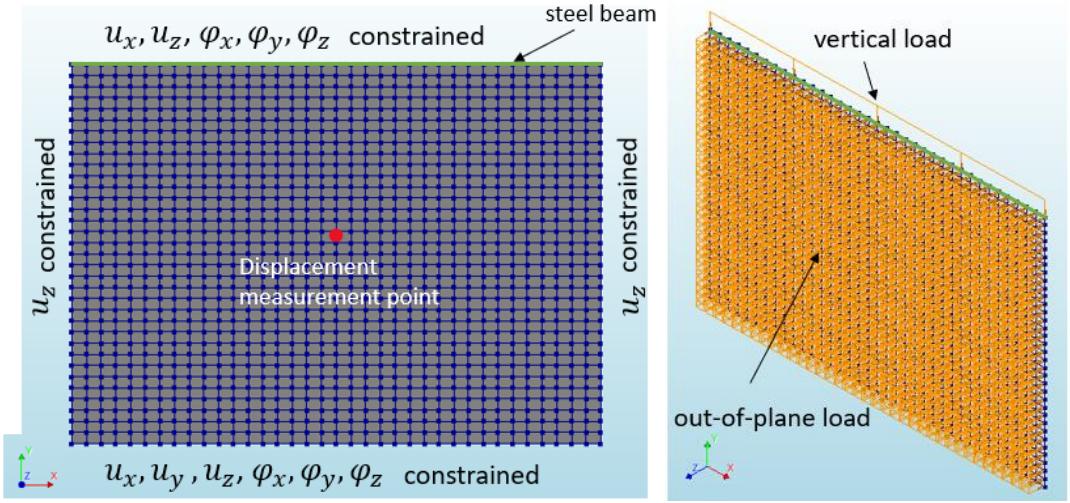

Figure 43. Finite element model of TUD_COMP-11 with boundary- and loading conditions

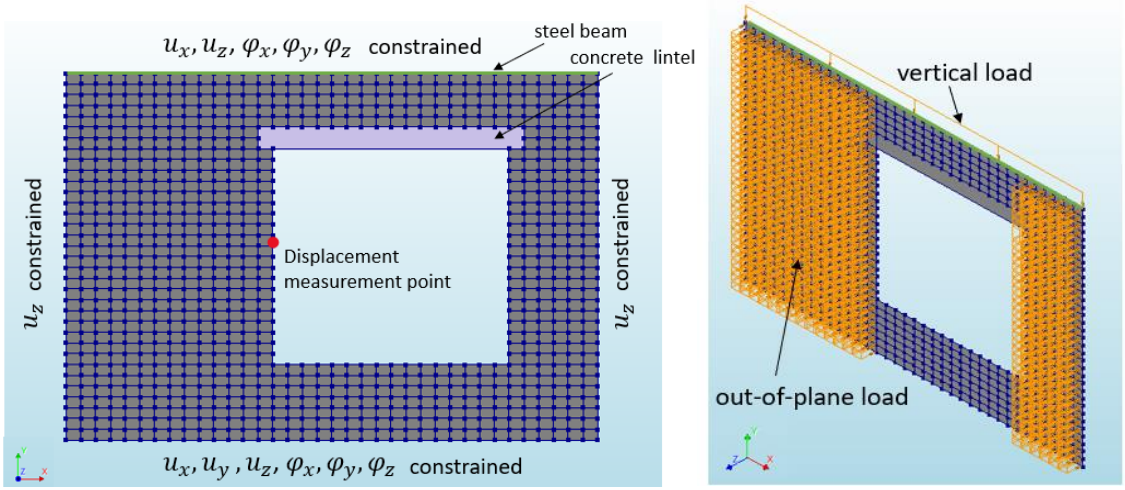

Figure 44: Finite element model of TUD_COMP-12 with boundary- and loading conditions

Figure 45: Lateral support system for OOP tests with detail of the applied wooden wedges (Ravenshorst & Messali, 2016b)

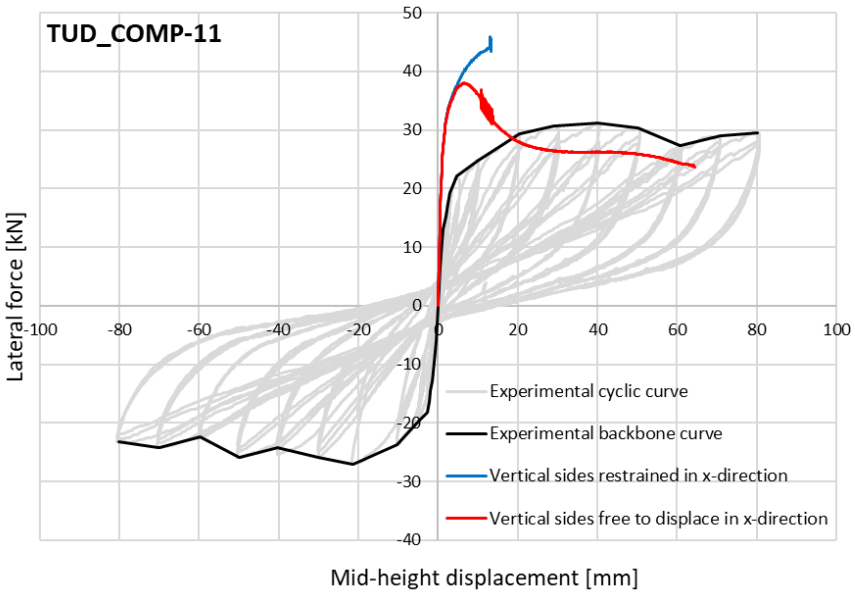

Figure 46. Numerical vs experimental force-displacement curve of TUD_COMP-11 with modified boundary conditions

Numerical results and discussion

This section compares the numerical results with the experimental results in terms of force-displacement curve and the crack patterns. The lateral force, calculated as the product of the applied lateral pressure and the loaded area of the wall, is plotted against the OOP displacement at the mid-height of the wall (red dots in Figure 43 and Figure 44). Further, the cyclic and the corresponding backbone curve from the experiment are shown in the force-displacement diagram. The backbone curve is obtained by connecting the OOP loads at the maximum displacement of each cycle. Similar to

the IP loaded walls, the interface relative displacements (DUNy, DUSx and DUSz) at the end of the analysis are considered for the comparison of the crack patterns.

TUD_COMP-11

In Figure 47(a), it can be observed that the numerical model overestimates the initial stiffness and the peak force. This can be associated to the finite rotational supports used in the experiments, which allowed some rotations, while in the numerical model the rotations are completely restrained. Furthermore, the experiment is cyclic, and this affects the magnitude of the peak force, as can be observed in Figure 47. There is a considerable difference between the peak loads from the experiment at the negative and the positive side, as brought in Table 11. In addition to the effect of cyclic loading, the difference in numerical and experimental peak force could be the result of different loading protocols. The test is conducted in displacement-controlled environment, whereas the numerical simulation is force-controlled analysis.

Figure 47(a) also shows the difference in the post-peak behaviour of the wall. The numerical curve reaches its capacity already at small displacement and drops sharply after reaching the peak, while the experiment showed more ductile post-peak response. This type of behaviour was also observed in the numerical reports of Karimi Ghaleh Jough & Golhashem (2020) and Chang (2022), where the two-way bending capacity of URM walls was determined using 3D simplified brick-to-brick modelling approach. It is found that this post-peak drop is insensitive to material parameters and boundary conditions, Chang (2022). Moreover, the shake-table tests by Graziotti et al. (2019), and monotonic static tests by Lawrence (1983) on OOP behaviour of URM walls also confirmed this phenomenon of sharp drop in the bending capacity of URM walls after reaching the peak. Hence, it can be said that the behaviour observed in the experiment might have been caused by the unknown special conditions of the specimen.

Regarding the crack patterns of the wall there is a good agreement between the numerical and experimental outcomes. The crack opening of the interfaces at the end of the analysis for three different layers i.e., front layer, middle layer and back layer are shown in Figure 47(d)-(f). The well-known envelope failure pattern can be identified from the figures. Contrary to the experiment, multiple horizontal cracks in the middle and multiple diagonal cracks occurred in the numerical solution. Further, the in-plane and out-of-plane shear sliding along the diagonal cracks of the wall can be observed in Figure 47(g) and Figure 47(h), respectively.

TUD_COMP-12

Compared to the solid wall TUD_COMP-11, TUD_COMP-12 has an eccentric large opening that reduces the OOP bending capacity in both experimental and numerical results, as can be observed in Table 11. Figure 48(a) shows the overestimation of the peak force and a lower stiffness degradation in the pre-peak phase, compared to the experiment which can be associated to the similar reasons previously explained for the solid wall. The analysis diverged quickly after reaching the peak load, which could be related to the high normal tractions in the brick interfaces at the left pier of the wall, Figure 48(e). However, at that same location the cracking of the bricks was also observed during the experiment, Figure 48(c).

The deformation and the cracking of the wall are illustrated in Figure 48(b) and Figure 48(d), respectively. Full crack pattern could not be achieved due to the divergence in the numerical simulation. However, the horizontal cracks at the top and bottom layer of the wall, and multiple horizontal cracks in the middle of the left pier can be observed. Further diagonal crack at the top right corner of the opening is also observed, similar to the experiment.

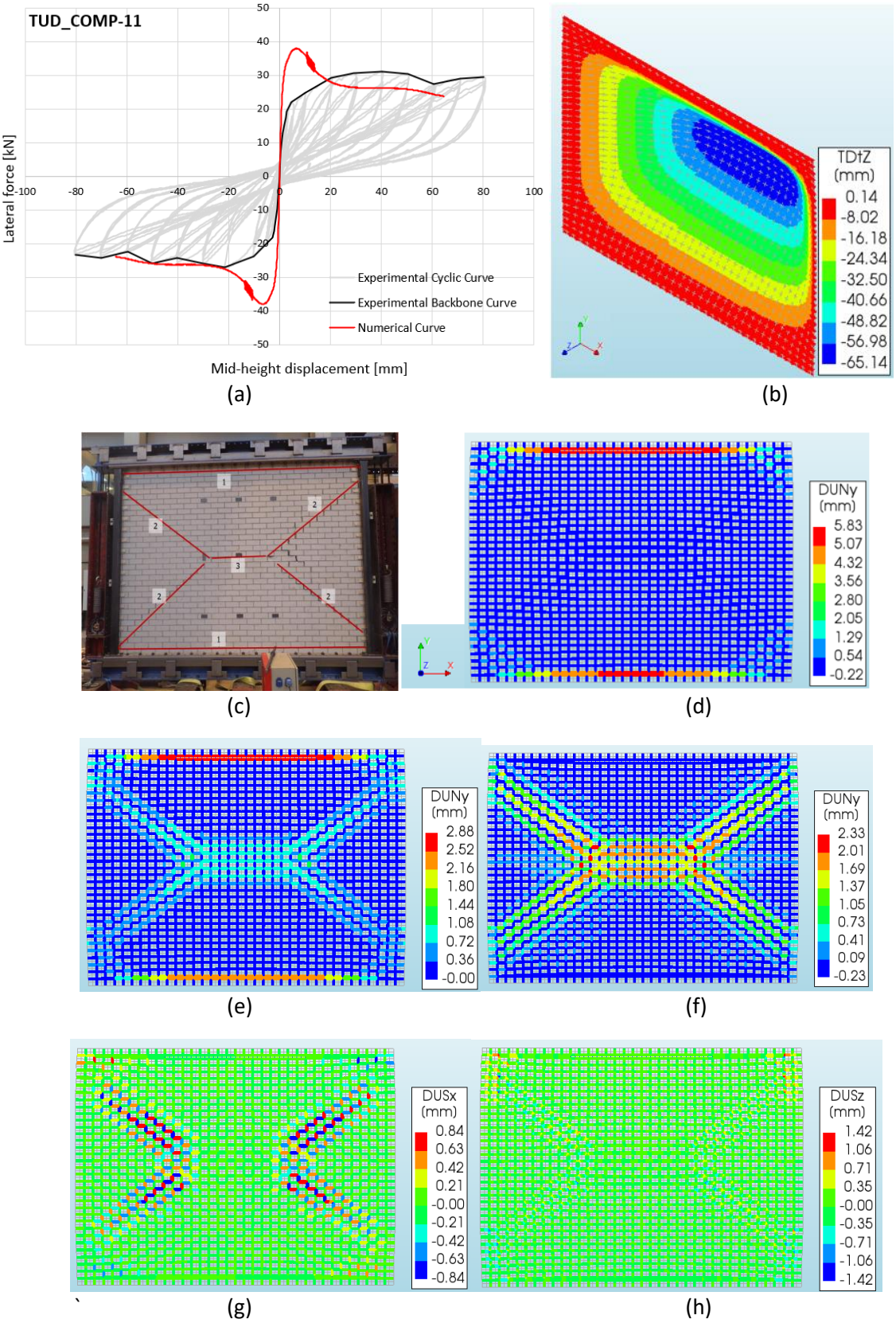

Figure 47: Numerical vs experimental comparison of TUD_COMP-11 (a) force-displacement curve; (b) out-of-plane deformation of the wall; (c) crack pattern observed at the end of the test; (d)-(e)-(f) crack interface opening of the front, middle and back layer at the end of the analysis; (g)-(h) in-plane and out-of-plane shear sliding of the interfaces at the end of the analysis; Deformation scaling factor = 15

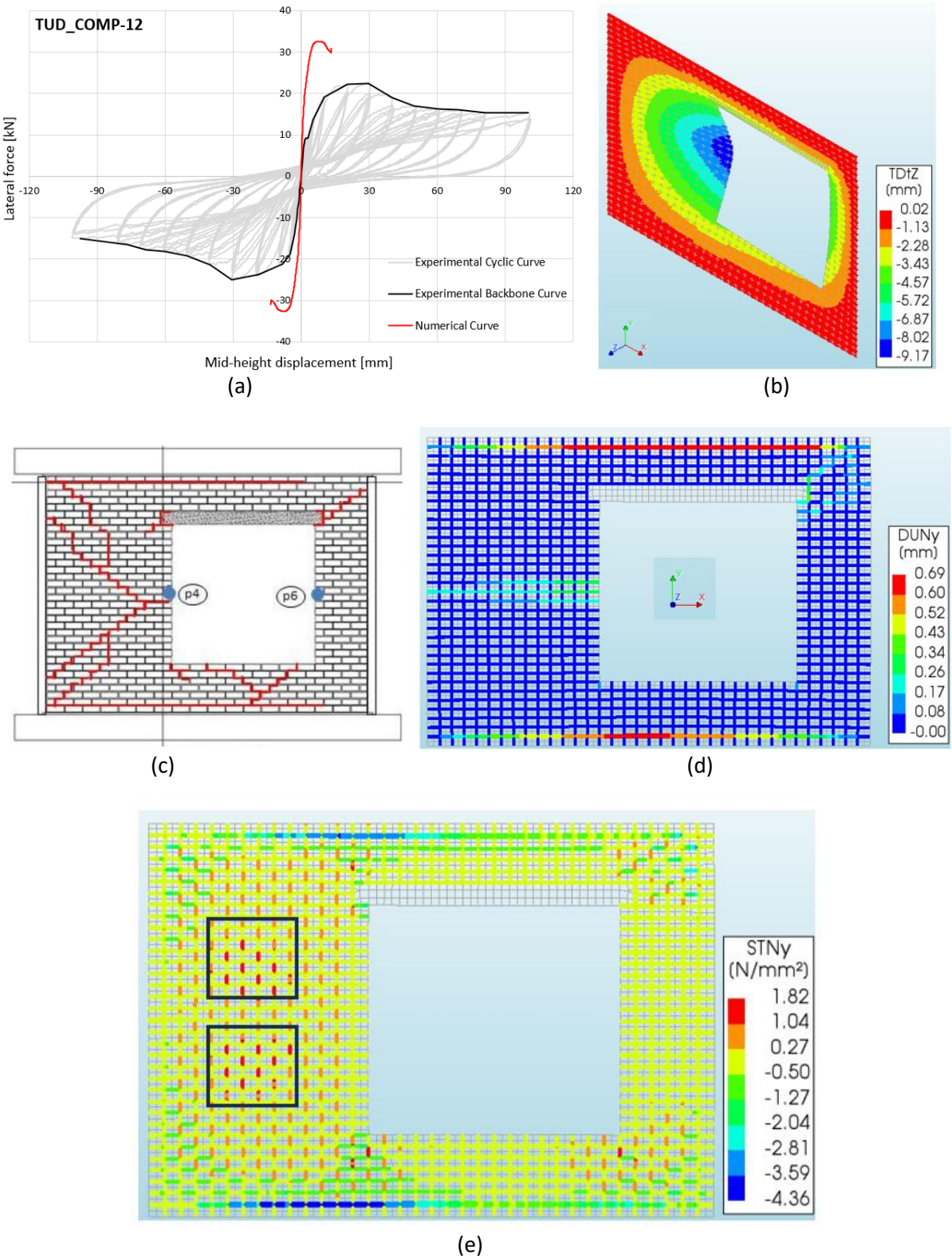

Figure 48: Numerical vs experimental comparison of TUD_COMP-12 (a) force-displacement curve; (b) out-of-plane deformation of the wall; (c) crack pattern observed at the end of the test; (d) crack interface opening with the maximum of the seven layers at the end of the analysis; (e) interface normal tractions of the back layer right before the divergence; Deformation scaling factor = 50

Table 11: Numerical vs experimental out-of-plane bending capacity of calcium silicate URM wall

Wall	Experiment		Numerical	Difference (%)	
	F^+ (kN)	F^- (kN)	F_{num} (kN)	F^+	F^-
TUD_COMP-11	31	-27	37.5	21	39
TUD_COMP-12	22	-25	32.5	47	30
F^+ = positive OOP capacity; F^- = negative OOP capacity; F_{num} = predicted OOP capacity					

5.4 Conclusion

The adopted numerical modelling approach with the calibrated parameters based on small scale tests predicted good results for the IP walls. Both the shear force capacity and the crack patterns are in good agreement with the experimental test. However, the model is not suitable for walls subjected to large IP displacements, such as cantilever walls, since numerical instability arises due to the crushing of mortar joints and cracking in brick interfaces. The accuracy of the modelling approach for the OOP walls is reasonable. Only the OOP bending capacity is overestimated, as shown in Table 11, which could have been caused due to differences in boundary condition (full or partial rotation restriction), type of test (cyclic or monotonic) and loading condition (displacement control or load control) between numerical simulation and experimental tests. However, the cracking pattern of the solid wall is correctly estimated by the numerical model. For the wall with opening, the post-peak behaviour could not be achieved since the model could not capture the failure of the bricks and resulted in brittle failure. Nevertheless, this report focuses more on the determination of the strength reduction because of IP damages, rather than the post peak response. Overall, the numerical results are in acceptable range and do not deviate much from the experiments. Besides this thesis is not aimed to be a detailed extensive investigation of the topic. Therefore, the numerical model is considered to be reliable for this report.

Chapter 6 Numerical simulations of pre-damaged URM walls

6.1 Introduction

The objective of this thesis is to investigate the OOP behaviour of the walls in the pre-damaged condition. For this purpose, it is important to damage the wall initially before applying the OOP load. It should be reminded that this report is limited to pre-damage that could arise from the IP seismic load and other pre-damages from sources such as settlement are not considered. Two different approaches, explained in the following paragraphs, are considered to apply the pre-damage to the wall. Furthermore, the study is performed for four different damage states that are classified based on the damage observed during the experimental test. TUD_COMP-4 (solid wall) and TUD_COMP-12 (wall with an opening) are selected for the case study with the same material properties as the ones considered in the validation of the numerical model.

Reduced-parameters approach: In this approach, the material input parameters such as strength & stiffness properties of the interface elements at the pre-defined cracked regions (weak spots) are reduced to produce similar response as observed during the IP test. For each damage state, the numerical response is compared to the test results of the cycle corresponding to that damage state. The comparison is done in terms of force-displacement curve, emphasizing on the initial stiffness and the peak shear force. Subsequently, the OOP analysis is performed for the weakened wall.

Sequential loading approach: This approach is characterized by the sequential loading process, as can be observed in Figure 49. First the wall is loaded in IP direction to a certain drift that represents the damage state corresponding to the one observed in the experiment. Then the OOP load is applied under the IP pre-deformation until the wall fails. Agnihotri et al. (2013) also applied this type of approach to numerically investigate the effect of IP-damage on OOP strength of URM walls. Note that this approach works with per-deforming the wall, while reduced-parameters approach works with pre-damaging the wall.

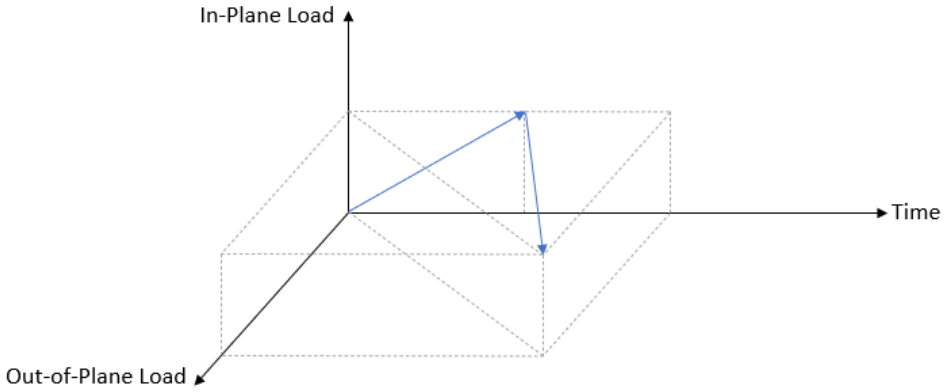

Figure 49. Schematic view for the sequential loading process

6.2 OOP analysis of pre-damaged solid wall

6.2.1 Classification of the damage states

The damage states are usually classified based on the evolution of the crack patterns observed during the experiment and they are associated to the normalized base shear force and drift ratios of the walls or buildings, Esposito et al. (2019). In this thesis report, the four damage states A, B, C and D are identified based on the progress of crack propagation observed during the IP cyclic test of TUD_COMP-4, Figure 50. Table 12 shows the description of the different damage states and the corresponding drift at which the damage is observed. Similar description of the damage states could also be observed in

the experimental test of Esposito et al. (2019) on a building-scale masonry assemblage, where opening of head joints and sliding along bed joints in the masonry piers were considered as minor damages and the stepwise crack pattern as moderate damage. However, the associated inter-storey drift at the ground floor, related to these damage levels were high (minor damage=0.2% and moderate damage=0.5%) compared to TUD_COMP-4. It should be mentioned that the cited seismic assessment test was performed on two-storey house, while this thesis report focuses only on walls.

Table 12: Characteristics of the damage states

Damage state		Wall drift (%)
A	No damage observed	0.01
B	First visible diagonal shear cracks close to the centre of the wall, connected by a short horizontal crack in the middle of the panel	0.057
C	Opening and expansion of the diagonal cracks to the corners	0.10
D	Further opening of the cracks & bed joint sliding in the middle	0.20

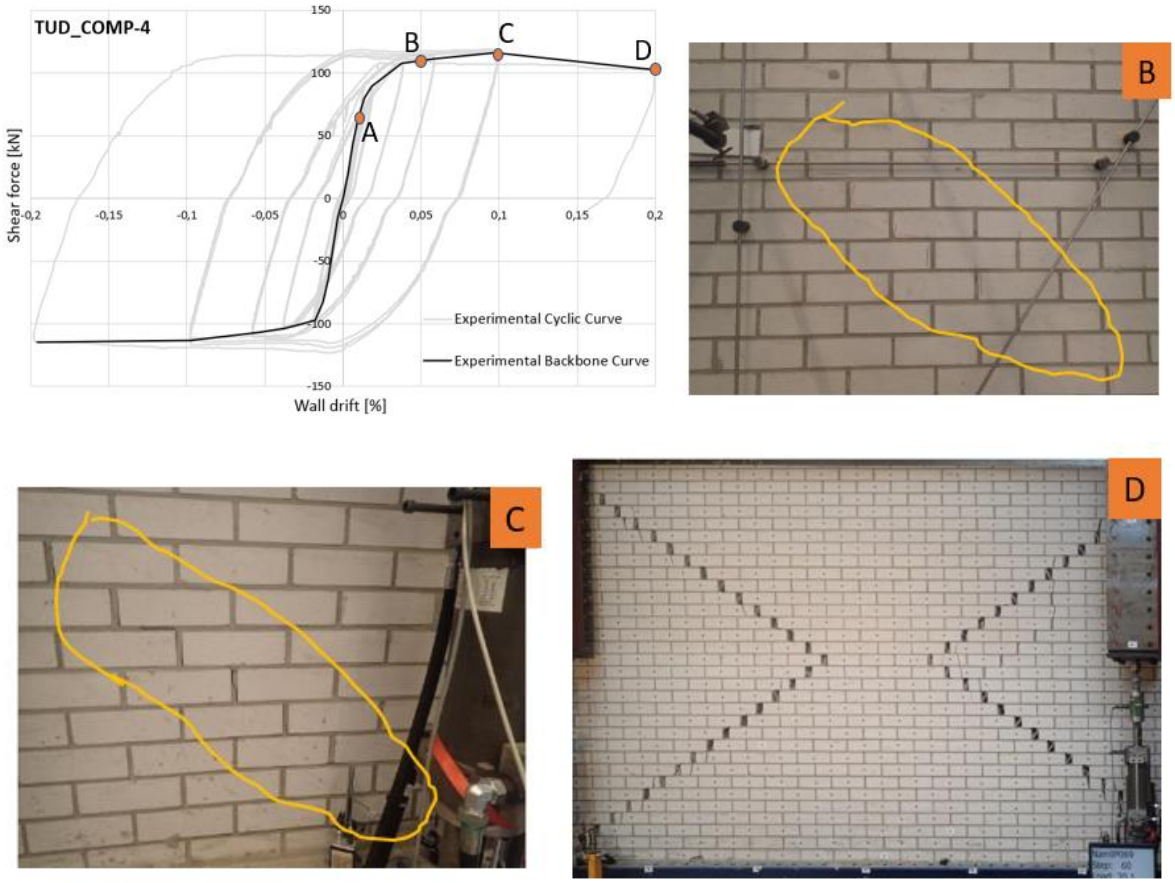

Figure 50. Classification of the damage states (a) damage states in the force-drift curve; (b)-(c)-(d) damage observed during the experiment for damage states B, C and D (Ravenshorst & Messali, 2016a)

6.2.2 OOP analysis applying reduced parameters

This method is performed in two different ways. In variant 1, the damaged properties (reduced parameters) are fixed, as given in Table 13, and are assigned to different cracked (weakened interface)

regions for each damage state. The different weakened interface regions can be observed in Table 14. Variant 2 is characterized by the fixed weakened interface region, as shown in Figure 51, assigned with different damaged properties for each damage state. The different damaged properties are given in Table 15. The pre-damage is applied only in the mortar joints since no cracking of the bricks was observed during the experiment. Table 13 shows the virgin and the pre-damaged material properties of the interface elements. Note that only the cracking and shearing parameters are reduced. The crushing is neglected in the pre-damage, since the experiment showed a shear failure in the wall. Furter, it should be noted that the IP analyses are performed with 0.5 MPa initial vertical pre-compression, while in the OOP analyses of the pre-damaged walls this is decreased to 0.05 MPa.

IP results

Both variants predicted good results for each damage state compared to the results of the IP test, as can be observed in Table 14 and Table 15. The initial stiffness and the peak force of the force-drift curves are in good agreement with the experiment. Hence, the OOP analysis of pre-damaged wall can be performed considering both variants.

OOP results

In this section, the OOP results obtained through the method of using reduced parameters are presented and discussed. Figure 52 shows the OOP force-displacement curves of variant 1 and variant 2. The OOP displacement is taken at the mid-height of the wall. For both variants, it can be observed that the peak force is further reduced with the increase of the pre-damage. However, the reduction of the OOP capacity is more consistent in variant 1 than variant 2. In variant 2, there is a large drop in force capacity already at the early damage state (damage state B) indicating that the extension of the damage is more important than reducing the mechanical properties. Further, it can be observed that under severe pre-damaged condition of the wall (damage state D) the force capacity reduces by 40% of its undamaged capacity. It is noteworthy that the pre-damage has no significant influence on the residual capacity of the wall, as it only reduces the role of cohesion and tensile resistance (both influencing the two-way bending response) and has minor effect in the residual load-bearing strength caused by friction. Table 16 shows the crack patterns of the pre-damaged wall at different damage states. The crack patterns are similar to that of the undamaged wall, the envelope failure pattern is obtained for each damage state. The only difference in the crack pattern between the undamaged and pre-damaged wall is that the OOP damage gets localized in the pre-defined weakened interface region of the pre-damaged wall, mainly in the middle of the wall (horizontal crack). Besides, the crack width also increases in the case of pre-damaged condition.

Table 13: Virgin vs pre-damaged input parameters for the weakened interface regions

Parameter	**Symbol**	**Unit**	**Virgin**	**Pre-damaged**
Normal stiffness	k_{nn}	*N/mm³*	191	10
Shear stiffness	k_{ss}	*N/mm³*	84	3
Tensile strength	f_t	*MPa*	0.10	0.01
Mode-I fracture energy	G_f^I	*N/mm*	0.005	0.0005
Initial shear strength	$f_{v,0}$	*MPa*	0.14	0.014
Internal friction angle	φ	*degree*	25	20
Residual friction angle	φ_r	*degree*	30	30

Mode-II fracture energy	G_f^{II}	*N/mm*	0.025	0.0025
Compressive strength	f_c	*MPa*	6.35	6.35
Compressive fracture energy	$G_{f,c}$	*N/mm*	3.0	3.0

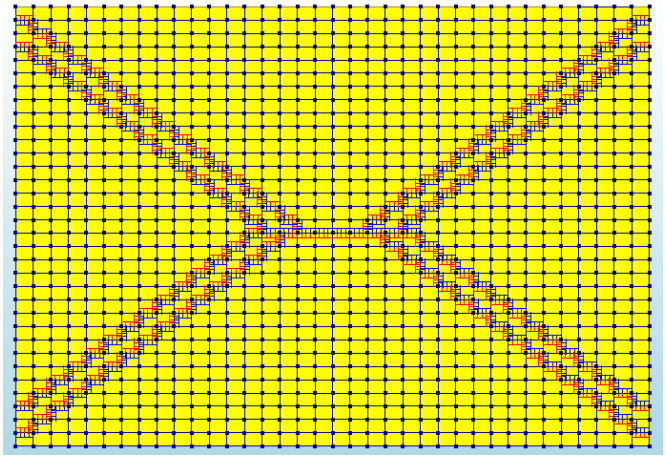

Figure 51. Fixed weakened interface region for each damage state of variant 2

Table 14: Numerical vs experimental shear force-drift curve of the solid wall considering fixed damaged properties and different weakened interface region for each damage state

Damage state	Weak spot	Numerical vs experimental shear force-drift diagram
A	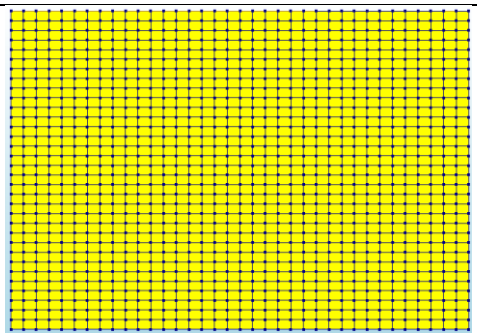	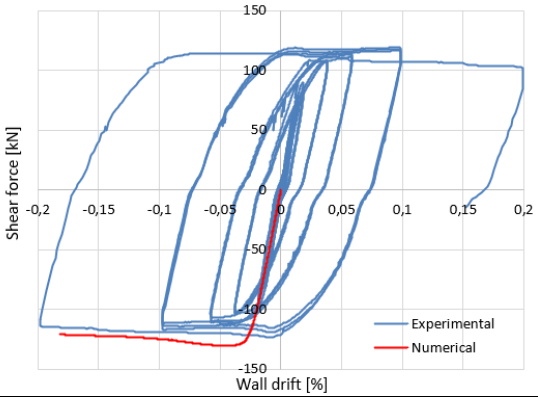
B	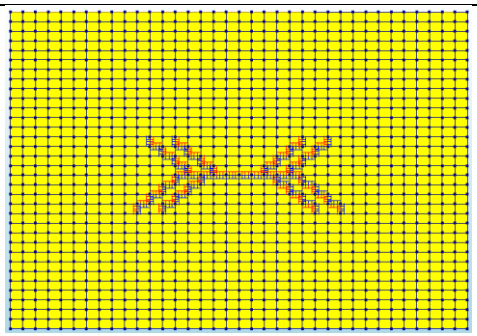	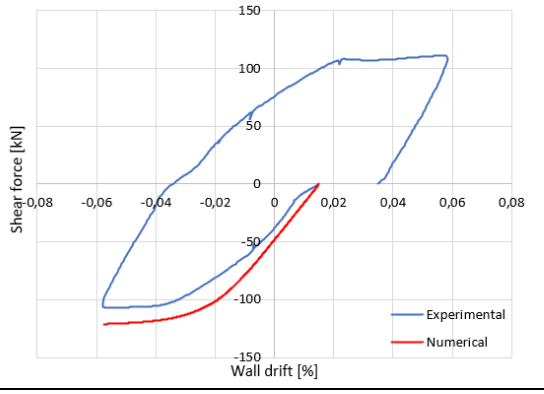

C	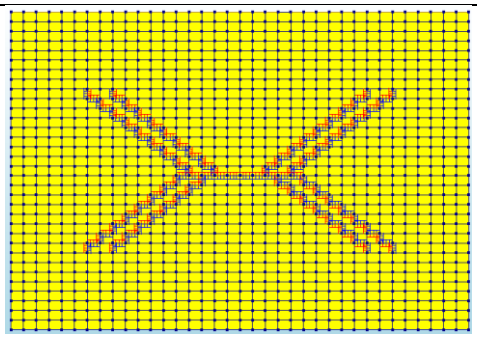	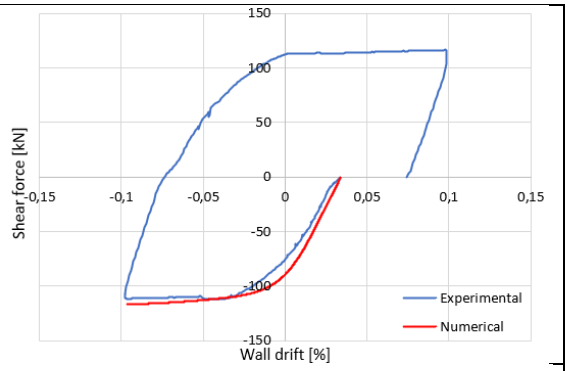
D	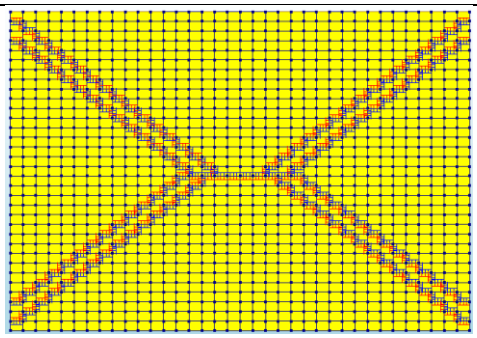	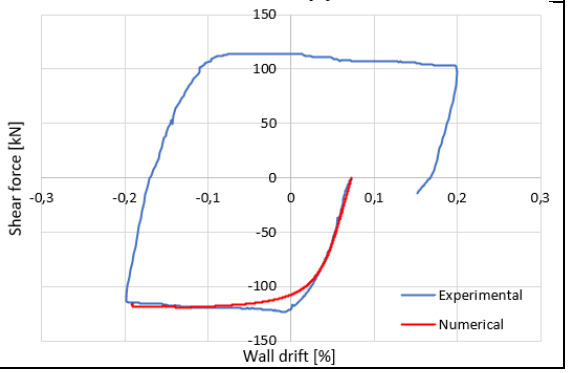

Table 15: Numerical vs experimental shear force-drift curve of the solid wall considering fixed weakened interface region and different damaged properties for each damage state

Damage state	Damaged interface properties		Numerical vs experimental shear force-drift diagram
A	**Parameter**	**Virgin**	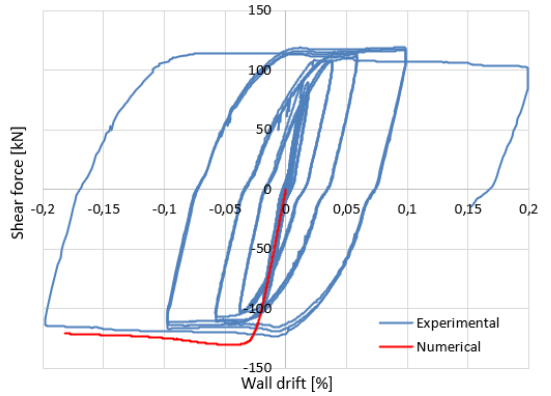
	k_{nn} (N/mm^3)	191	
	k_{ss} (N/mm^3)	84	
	f_t (MPa)	0.10	
	G_f^I (N/mm)	0.005	
	$f_{v,0}$ (MPa)	0.14	
	φ (degree)	25	
	φ_r (degree)	30	
	G_f^{II} (N/mm)	0.025	
	f_c (MPa)	6.35	
	$G_{f,c}$ (N/mm)	3.0	
B	**Parameter**	**Pre-damaged**	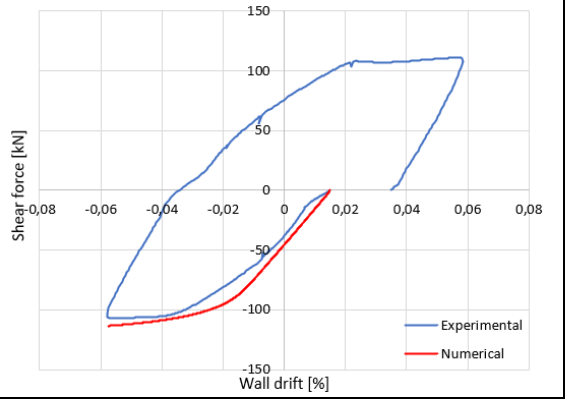
	k_{nn} (N/mm^3)	20	
	k_{ss} (N/mm^3)	6	
	f_t (MPa)	0.05	
	G_f^I (N/mm)	0.0025	
	$f_{v,0}$ (MPa)	0.07	
	φ (degree)	20	
	φ_r (degree)	30	
	G_f^{II} (N/mm)	0.0125	
	f_c (MPa)	6.35	
	$G_{f,c}$ (N/mm)	3.0	

C	**Parameter**	**Pre-damaged**	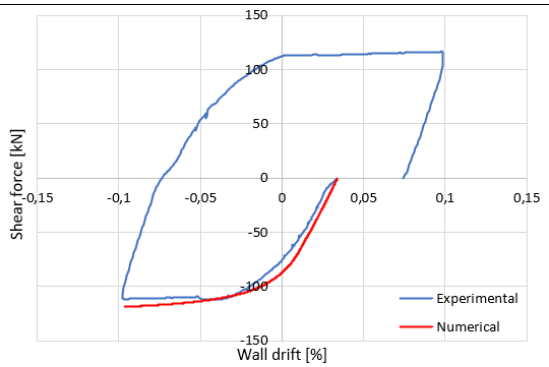
	k_{nn} (N/mm^3)	15	
	k_{ss} (N/mm^3)	5	
	f_t (MPa)	0.025	
	G_f^I (N/mm)	0.00125	
	$f_{v,0}$ (MPa)	0.035	
	φ (degree)	20	
	φ_r (degree)	30	
	G_f^{II} (N/mm)	0.00625	
	f_c (MPa)	6.35	
	$G_{f,c}$ (N/mm)	3.0	
D	**Parameter**	**Pre-damaged**	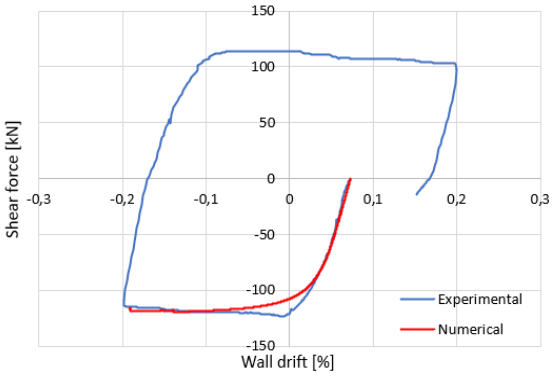
	k_{nn} (N/mm^3)	10	
	k_{ss} (N/mm^3)	3	
	f_t (MPa)	0.01	
	G_f^I (N/mm)	0.0005	
	$f_{v,0}$ (MPa)	0.014	
	φ (degree)	20	
	φ_r (degree)	30	
	G_f^{II} (N/mm)	0.0025	
	f_c (MPa)	6.35	
	$G_{f,c}$ (N/mm)	3.0	

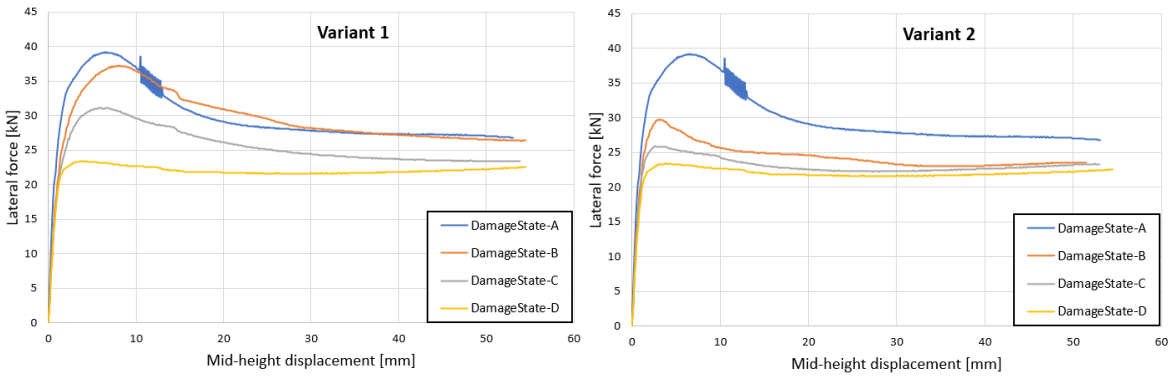

Figure 52. OOP force-displacement curves of the pre-damaged solid wall obtained through reduced-parameters approach

Table 16. Interface crack opening of the pre-damaged solid wall with reduced-parameters approach, taken at the mid-height OOP displacement of 50 mm (deformation scaling factor = 10)

Damage state	Variant 1	Variant 2
A	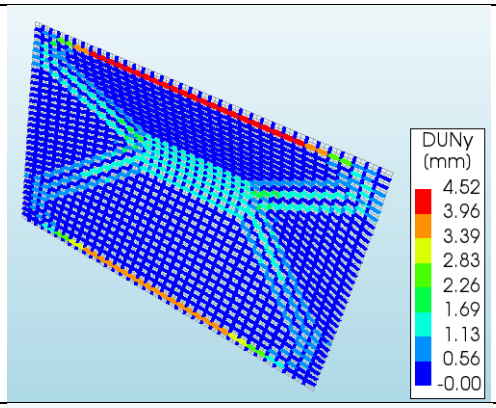	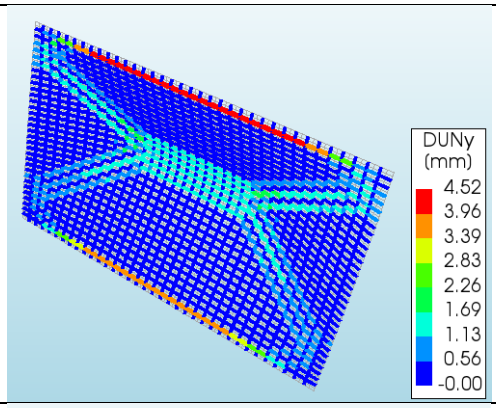
B	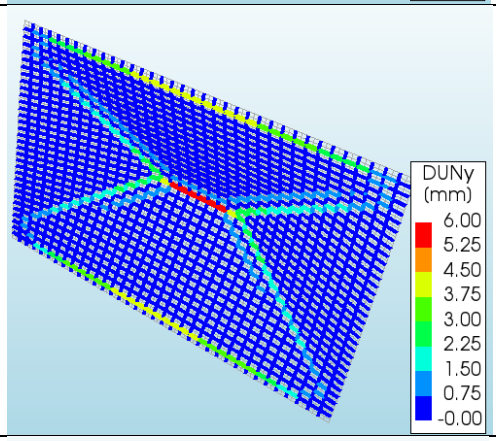	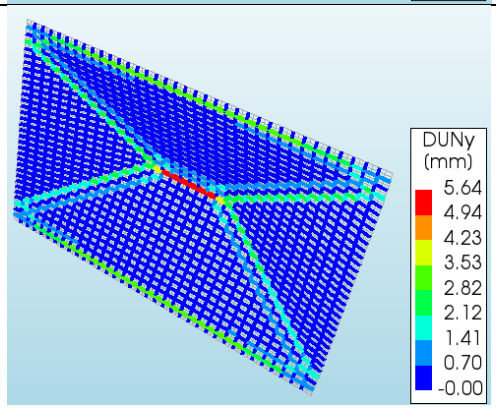
C	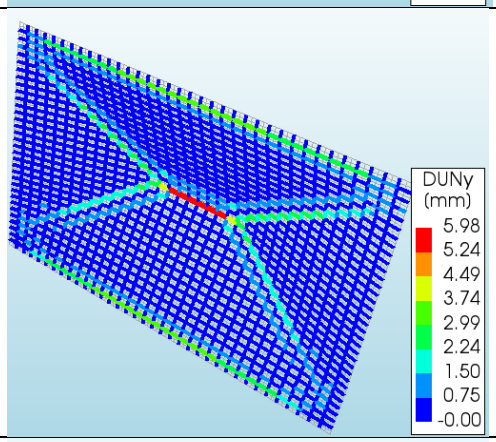	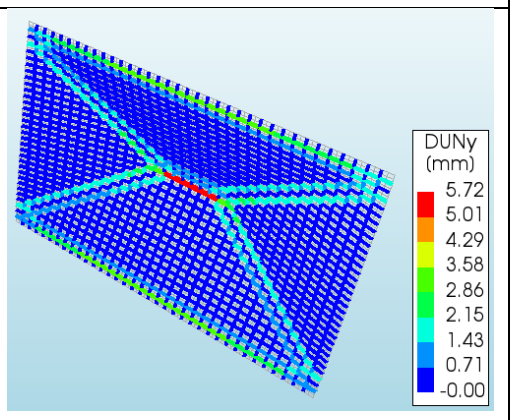
D	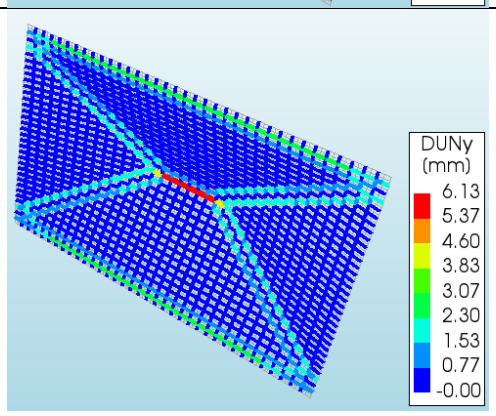 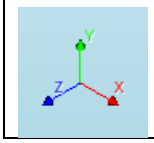	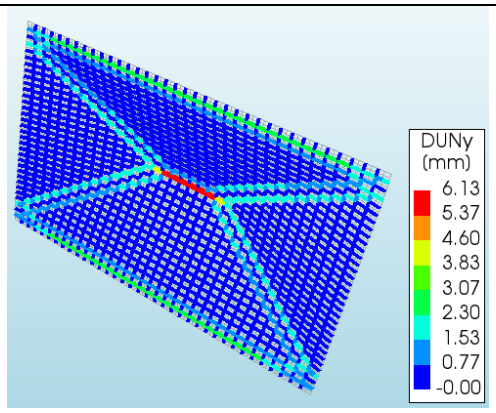

6.2.3 OOP analysis applying sequential loading

As previously stated, this approach is characterized by the IP loading of the wall up to the corresponding drift of the damage state followed by the OOP analysis until the wall fails. Figure 53 shows the lateral force-displacement curve of the pre-deformed wall. It is observed that in this approach the effect of the pre-damage on the peak force is less compared to the other approach. The reason for this could be linked to the fact that the reduced-parameter approach considers a damaged region under cyclic load and separates the wall into four intact blocks connected via those damaged interfaces. This allows for easier rigid body motion. But, in sequential loading approach, the pre-damage is simulated through the IP monotonic analysis, causing damages to accumulate in a smaller region, while most parts of the wall remain interconnected. Further, as expected for a pre-damaged wall, the pre-peak stiffness is reduced with an increasing level of damage. However, this reduction is not observed in the reduced-parameters approach, as it only considers pre-damage at specific locations. It should be noted that for the damage state D (with IP drift of 0.2%), the OOP analysis diverges at early stage resulting in a large difference in the OOP capacity between damage state C and damage state D. This suggests that the pre-damage with 0.2% IP drift is such that the wall immediately becomes unstable and fails at early stage of the OOP analysis. This can be explained by the diagonal cracking and shearing of the mortar joints in the middle and shear sliding near to the top edge of the wall due to IP loading as observed in Figure 54. In other words, the wall is separated into two rigid bodies that can easily collapse in OOP because of the very weakened interface region between them. Similar to the previous approach, the pre-damage has no significant influence on the residual load-bearing strength of the wall. As regards the crack opening of the interfaces, Figure 55 shows that there is no noticeable difference in the OOP response between the undeformed and pre-deformed wall. The envelope-shape failure pattern is achieved at the end of the analysis for both undeformed and pre-deformed conditions.

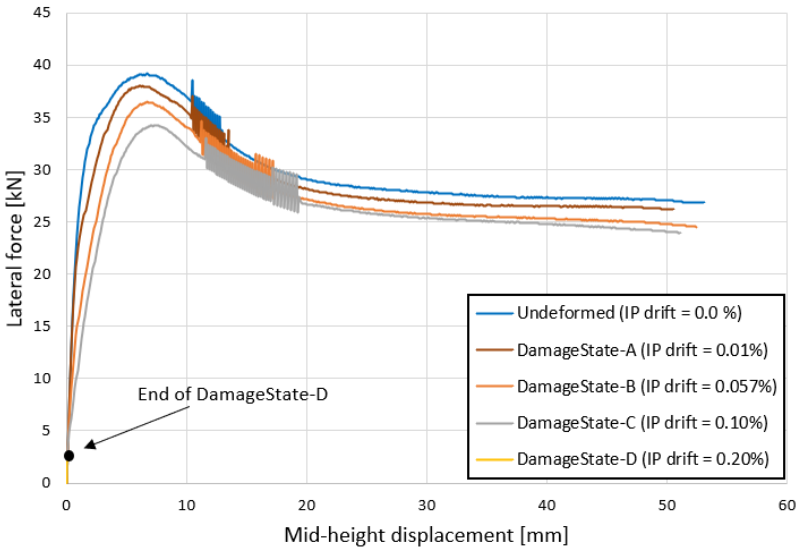

Figure 53. OOP force-displacement curve of the pre-deformed solid wall obtained through sequential loading approach

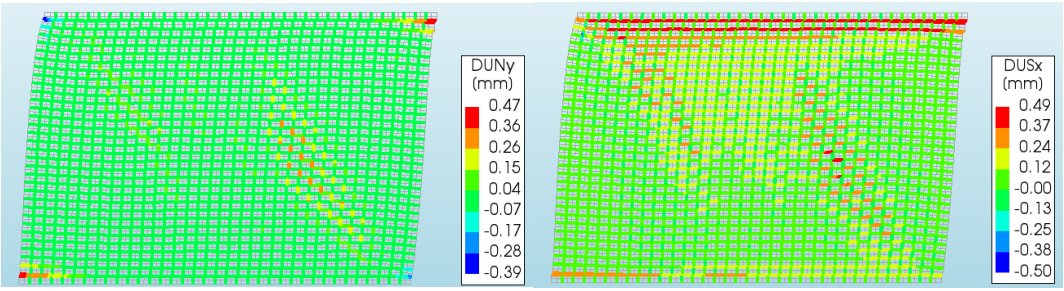

Figure 54. Damage observed prior to the OOP loading (a) crack interface opening (b) in-plane shear sliding

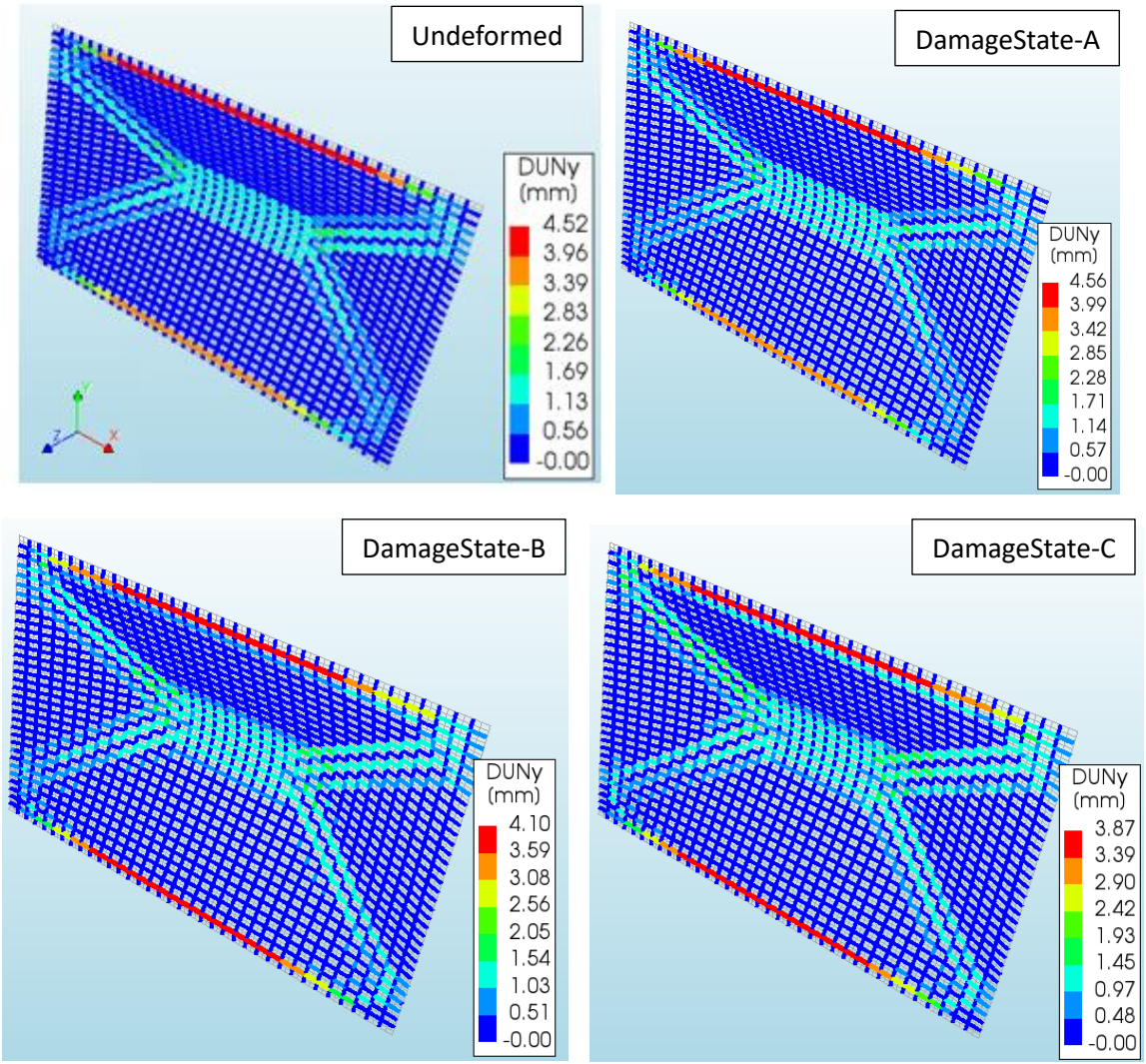

Figure 55. Interface crack opening of the pre-deformed solid wall obtained through sequential loading approach, taken at the mid-height OOP displacement of 50 mm (deformation scaling factor = 10)

6.2.4 Summary

The effect of IP damages on the OOP load-bearing strength for the solid wall is summarized in Figure 56. The normalized OOP capacity, which is the ratio between OOP force capacity of the pre-damaged wall to that of the undamaged wall, is plotted against the pre-applied IP wall drift.

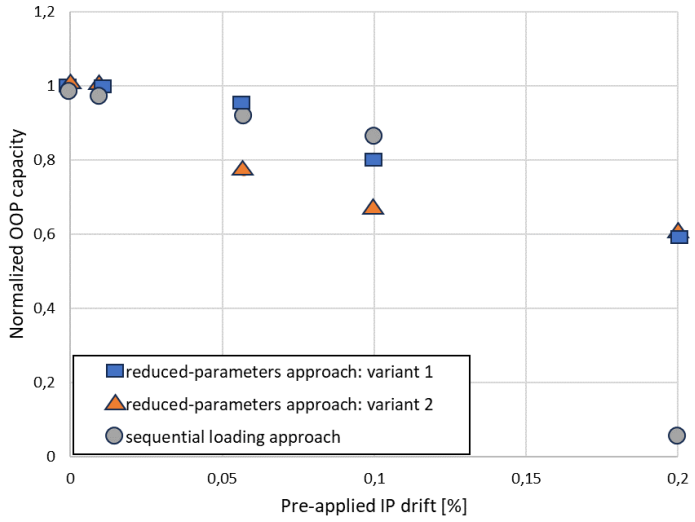

Figure 56. Effect of IP damage on the OOP force capacity of the solid wall

6.3 OOP analysis of pre-damaged wall with an opening

6.3.1 Classification of the damage states

Since no IP tests on walls with openings were conducted during the series of tests on CS walls, the identification of the pre-damage is done based on the numerical IP analysis of TUD_COMP-12. Note that the characteristiscs of the wall such as boundary conditions and vertical pre-compression are identical to that of solid wall i.e. double clamped with 0.5 MPa vertical pre-compression. Figure 57(a) shows the force-drift diagram from the IP analysis. As expected, the presence of the opening reduces the shear force capacity compared to the capacity of the solid wall (= 136 kN). The maximum wall drift, which is 0.14%, is also less compared to the solid wall (=0.20% drift). The wall is analyzed in both directions, considering the asymmetric position of the opening. The deformation behaviour of the wall in the positve and the negative direction is illustrated in Figure 57(b) and Figure 57(c), respectively. Both loading directions provide similar crack patterns of the wall. It can be seen that the cracking starts at the corners of the opening. Futher increasing of the drift results in multiple diagonal shear cracks in the left pier of the wall. Some horizontal flexural cracks in the bed joints are also observed at the top and bottom left corner of the left pier. Based on these observations the three damage states are classified for the wall with opening, as illustrated in Figure 57(a) and Table 17. Damage state A represents the start of the cracking at the corners of the opening. Damage state B is defined by expansion of the cracks at the corners of the openig and some horizontal flexural cracks. The multiple shear diagonal cracks are added to the left pier of the wall in damage state C. Note that this approach is similar to variant 1 of solid wall i.e. the fixed damaged properties are assigned to different weakened interface regions for each damage state. The same damaged properties as considered for the solid wall, see Table 13, are also used for the wall with opening. The variant 2 is not adopted for the wall with opening, since this method did not provide good results for the solid wall. Moreover, there is no cyclic experiment on the wall with opening to be used for calibrating the material properties in variant 2.

6.3.2 OOP analysis applying reduced parameters

Figure 58 shows the OOP force-displacement curve of the pre-damaged wall with opening for different damage states. It is observed that the considered damage states A and B do not have any influence on the OOP capacity of the wall. The damage state C reduces the peak force by 14%. It is clear that the shear diagonal cracks from the IP damage are more influential in reduction of the OOP strength than

other cracks such as in the corners of the opening. The residual load-bearing strength of the wall is almost same for all damage states. Compared to the undamaged wall, where the failure occurs due to high stresses in the brick interfaces and the analysis diverges, the pre-damaged walls show the post-peak behaviour. In other words, the stress concentration in the brick interfaces is prevented because the load follows its path through the pre-defined weakened interfaces, resulting in more stable and ductile behaviour. For future research, it is suggested to exclude brick interfaces in the model when no considerable cracking of the bricks is expected or observed in the experiment.

As regards the crack pattern, the two horizontal cracks at the top and bottom mortar layer of the wall are developed after the OOP loading of the pre-damaged walls, as shown in Table 17. Furthermore, two diagonal cracks connected by multiple horizontal cracks in the middle of the left pier and diagonal cracks in the right corners of the opening can be observed. In the pre-damaged condition, for instance for damage state C, the cracks get localized at the weak interfaces such as in the middle of the left pier and at the right corner of the opening.

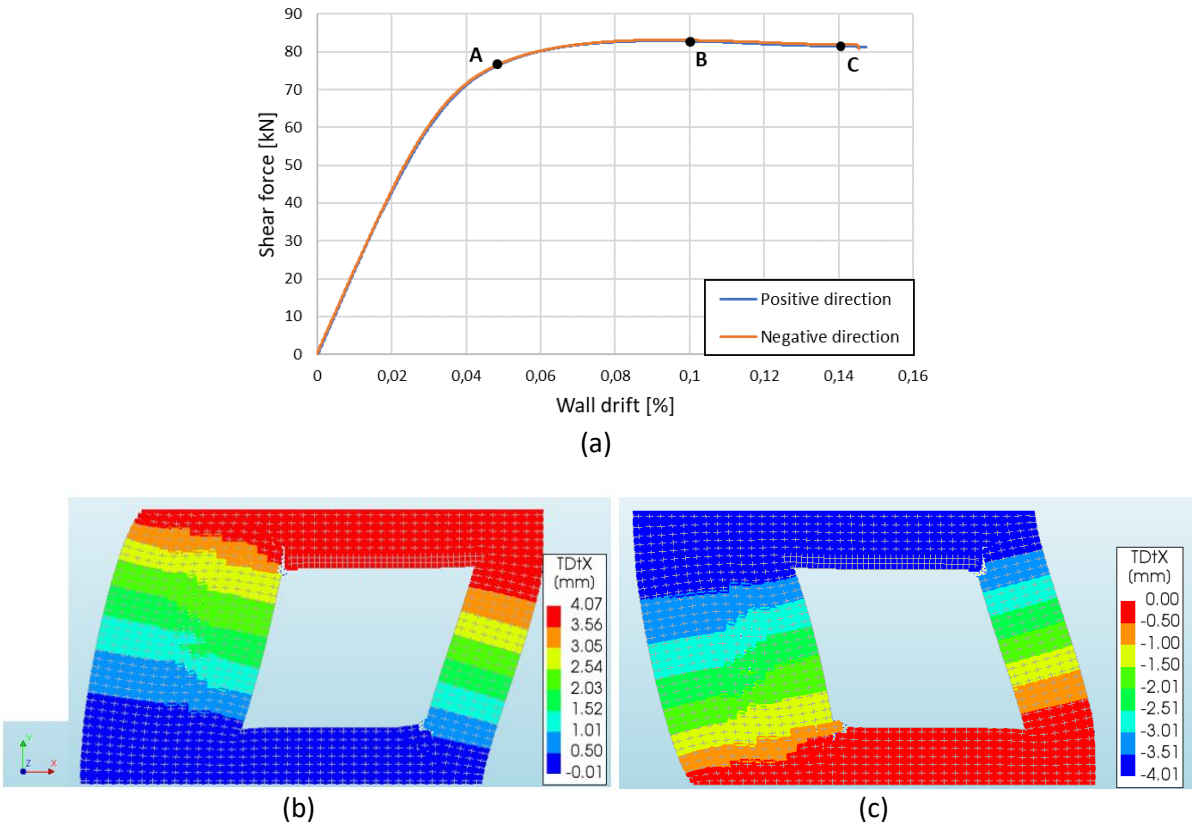

Figure 57. IP analysis of TUD_COMP-12 (a) Shear force vs wall drift curve; (b) Deformation at the end of the analysis in the positive direction; (c) Deformation at the end of the analysis in the negative direction (scaling factor = 150)

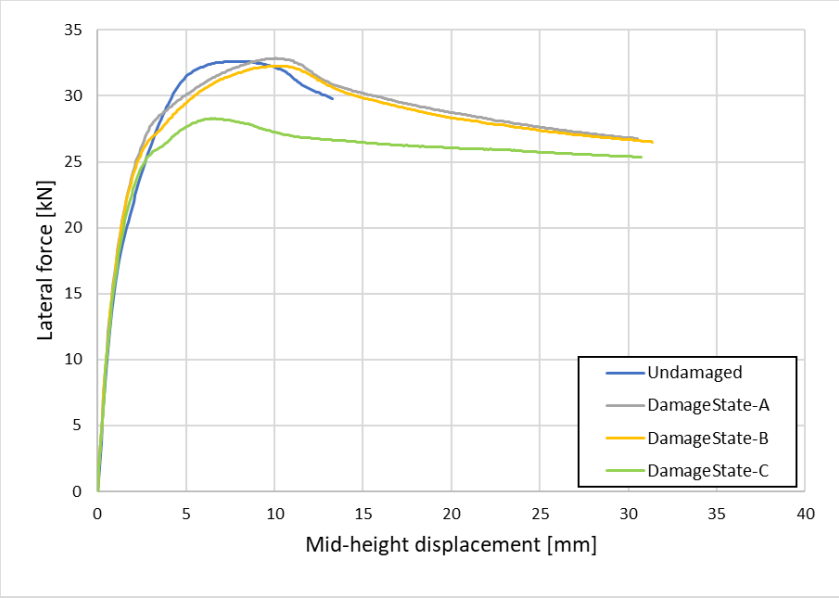

Figure 58. OOP force-displacement curve of the pre-damaged wall with opening obtained through reduced-parameters approach

Table 17. OOP analysis of pre-damaged wall with opening showing weakened interface regions and deformation behaviour for different damage states. The interface crack opening is taken at the mid-height (left pier) of the wall at the end of the analysis (deformation scaling factor = 20)

Damage state	Weak spot	OOP deformation showing interface crack opening DUNy
Undamaged	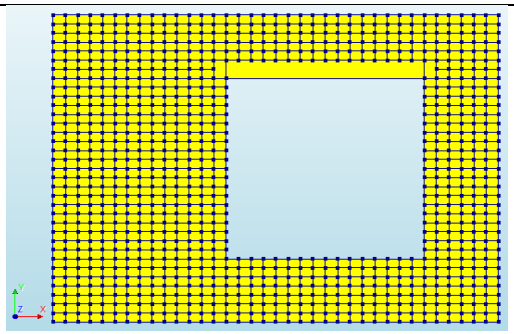	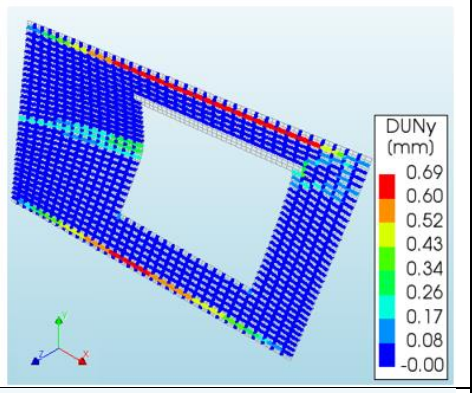
A	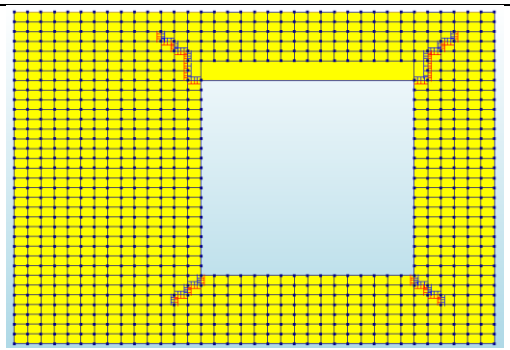	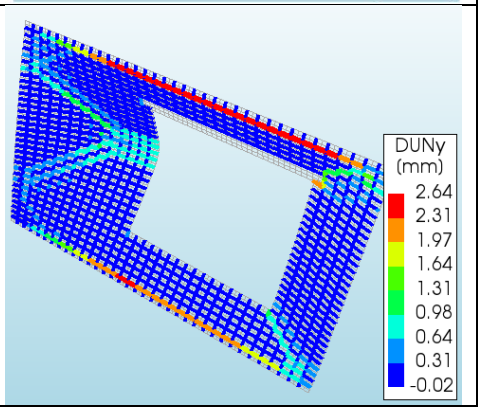

B	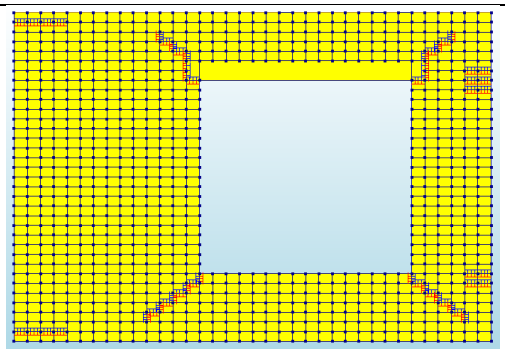	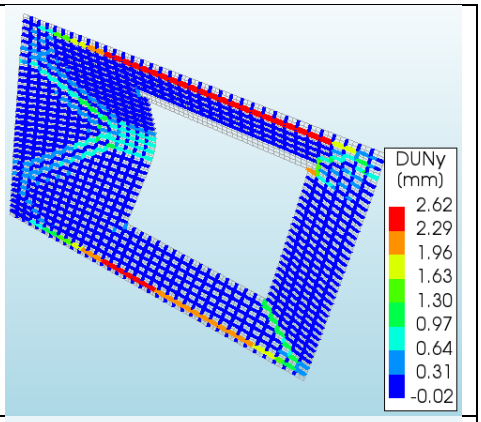
C	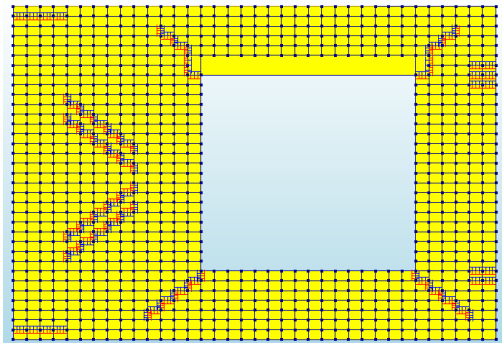	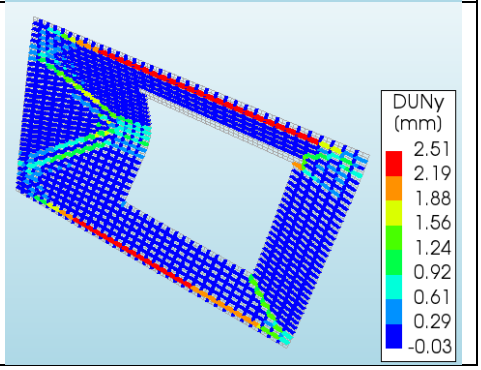

6.3.3 OOP analysis applying sequential loading

In this approach, the OOP analysis of the wall is performed considering four levels of IP drift that represents the pre-deformation of the wall. The OOP force-displacement curve obtained from the numerical analysis is illustrated in Figure 59. It shows some reduction in the pre-peak stiffness for increasing drift, as expected in a pre-damaged wall. Similar to the previous approach, the influence of the pre-deformation on the OOP maximum force is small. For IP drift of 0.14%, the OOP capacity of the wall is reduced by 11% only. Contrary to the other approach, the numerical analysis diverges immediately after reaching the peak force resulting in no post-peak response and therefore no full crack pattern could be developed for the pre-deformed wall. This is similar to the undeformed wall, where due to high stresses (close to the failure) in the brick interfaces the analysis diverged. This is also the case for the pre-deformed wall, Figure 60(a). The cracking pattern at the end of the analysis can be observed in Figure 60(b) for 0.10% pre-applied IP drift.

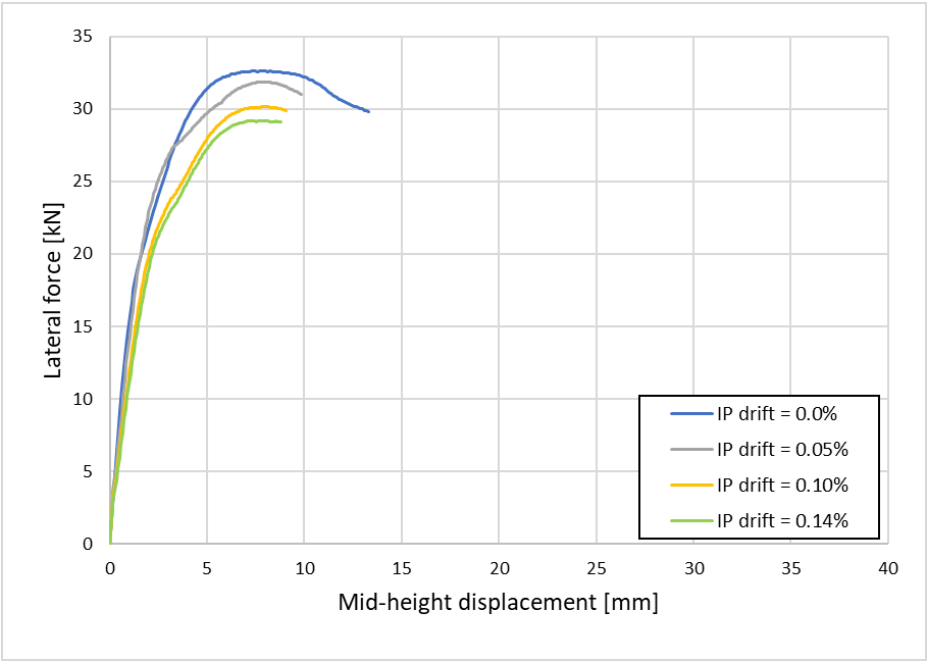

Figure 59. OOP force-displacement curve of the pre-deformed wall with opening obtained through sequential loading approach

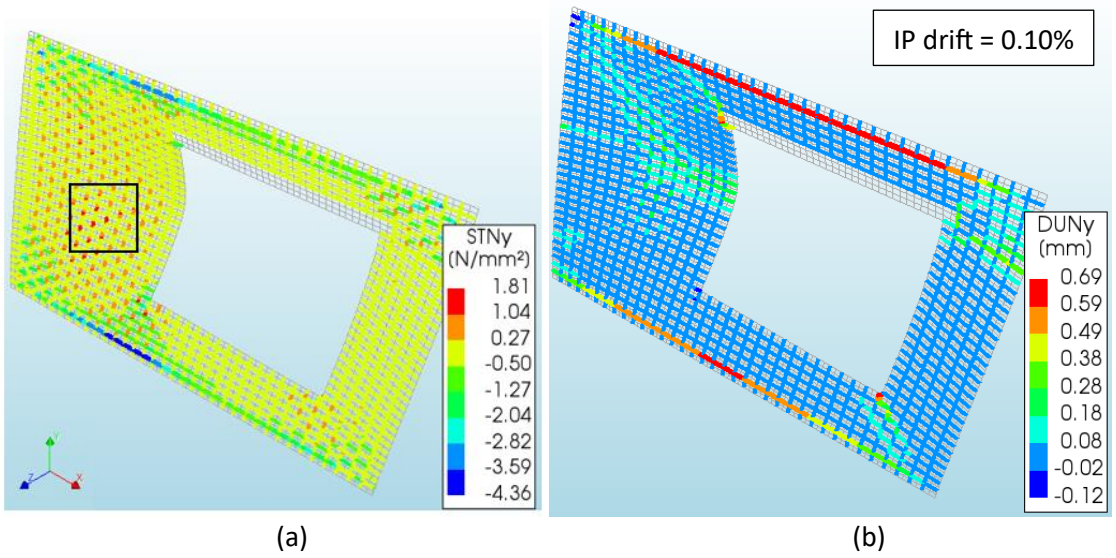

Figure 60. (a) Interface normal tractions of the back layer right before the divergence for IP drift of 0.10%; (b) maximum crack interface opening of the 7 layers at the end of the analysis for IP drift of 0.10%. (deformation scaling factor= 50)

6.3.4 Summary

The effect of IP damages on the OOP force capacity for the wall with opening is summarized in Figure 61. The normalized OOP capacity, which is the ratio between the OOP force capacity of the damaged specimen to that of the intact specimen, is plotted against the pre-applied IP wall drift.

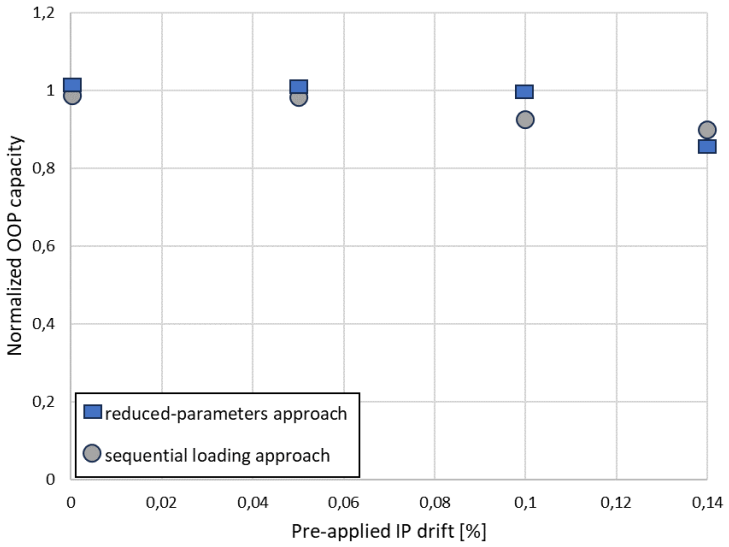

Figure 61. Effect of IP damage on the OOP force capacity of the wall with opening

6.4 Conclusion

This chapter investigated the effect of IP pre-damage on the OOP performance of both walls, without and with an opening. Two different approaches were considered to apply pre-damage to the wall. Reduced-parameters approach used the method of reducing the mechanical parameters at the cracked regions that could be identified from the experiment, whereas in the sequential loading approach the monotonic IP pre-deformation of the wall represented the pre-damage. The outcomes of the investigation in terms of reduction in force capacity due to the IP damages can be observed in Figure 62.

For the solid wall, it is found that both approaches give same results for small pre-applied IP drifts, up to 0.057% drift. The reduction in the OOP capacity is almost negligible until this drift level. As the damage increases, the reduction of the peak force also sharply increases. At 0.2% IP-drift, 40% reduction of the OOP peak force is observed with reduced-parameters approach, while in sequential loading approach, the wall immediately failed showing negligible OOP strength because of the severe IP damage. This is in consistent with IP tests of double-clamped walls where the tests were stopped around 0.2% drift level. As regards the crack pattern, in both undamaged and pre-damaged walls the well-known envelope crack pattern is obtained. Further, it is observed that the OOP damage gets localized in the weakened interfaces of the pre-damaged wall and the crack width becomes larger than those of the intact wall.

For the wall with opening, the considered damage states do not show much reduction of the OOP capacity. The pre-defined weakened interface region starting with damages at the corners of the opening results in negligible effect on the OOP strength. This also applies for the sequential loading approach, where for 0.1% IP drift the reduction in OOP peak force is only 8%. The maximum strength reduction observed is approximately 15% at maximum of 0.14% pre-applied IP drift. It should be noted that the wall with opening under no damage fails after reaching the peak due to high stresses in brick interfaces, resulting in no post-peak behaviour. However, under pre-damaged condition the post-peak response is achieved with reduced-parameter approach. This suggests that the stresses cannot concentrate in brick interfaces because of the pre-defined weakened interfaces, which represents the

pre-damage of the wall. Further, no significant difference in cracking pattern is observed between the undamaged and pre-damaged walls.

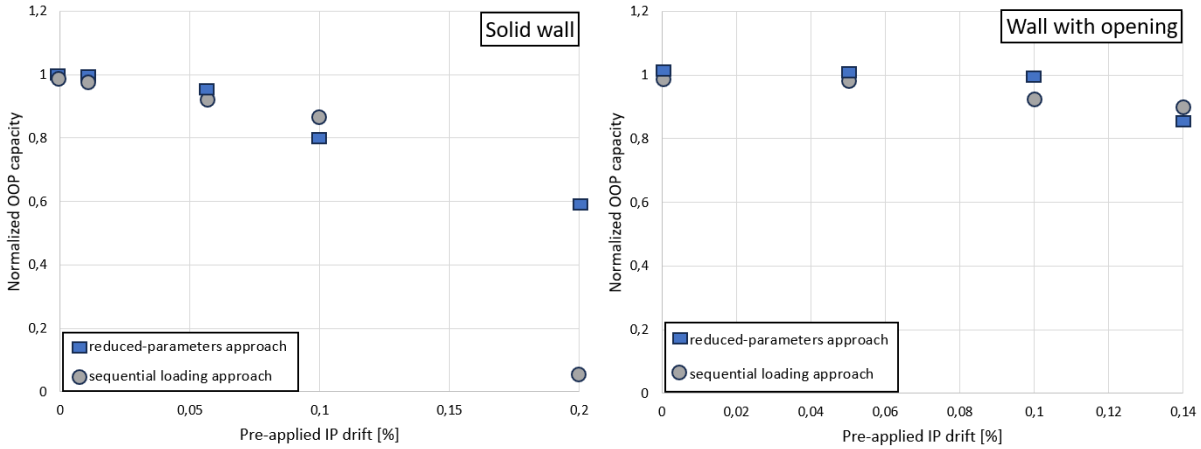

Figure 62. Effect of in-plane damage on OOP force capacity of solid wall and wall with opening

Chapter 7 Conclusions and Recommendations

7.1 Conclusions

Past earthquake observations have highlighted the significance of out-of-plane (OOP) local failure mechanisms as the main causes of collapse in unreinforced masonry (URM) structures. The OOP walls in such structures can exhibit considerable weakness and flexibility, especially when they are slender and have large openings. This vulnerability further increases when the walls are already in a pre-damaged state due to previous low-intensity earthquakes and settlements. For instance, the houses in Groningen have repeatedly been exposed to low-magnitude seismic loading, potentially leading to pre-damage of the walls before the next earthquake occurs. However, there is limited research on how these pre-damages affect the seismic behaviour of walls and structures, with only a few studies conducted so far. Hence, this thesis aims to conduct a preliminary investigation on how much the presence of pre-damage, caused by in-plane (IP) loading, reduces the OOP resistance of URM walls with and without openings.

Since experimental study is out of the scope of this thesis, a numerical modelling approach is employed to determine the OOP performance of pre-damaged walls. For this purpose, the research started with literature review on different modelling strategies used to simulate the behaviour of masonry under seismic loading. Four distinct modelling strategies were identified, including:

1. Block-based model: This approach involves simulating the actual texture of masonry, considering individual blocks (units) and mortar joints separately. This modelling technique is also known as micro modelling. There is a simplified version of this modelling approach, known as simplified micro modelling, where the blocks are enlarged, and zero-thickness interface elements represent the mortar joints (mortar and block-mortar interface).
2. Continuum model: In this strategy, no distinction is made between individual blocks and mortar joints, treating the masonry as a homogenized continuum deformable body.
3. Macroelement model: The structure is divided into deformable panel-scale structural components (macro-elements), typically representing piers and spandrels.
4. Geometry-based model: The structure is represented as a rigid body defined by its geometry.

It is found that the simplified micro modelling using shell elements is suitable for this thesis work for the following reasons:

- For the inclusion of the pre-damage, the micro modelling approach is more suitable than the continuum model. The pre-damage, resulting from the IP loading, typically appears as diagonal stepwise cracks and can be implemented in a detailed manner by reducing the mechanical parameters for the interfaces at certain locations. However, this is challenging in the continuum or macroelement models since they require extensive trial and error procedures to give close-to-reality results.
- For the scope of this thesis, which is a preliminary investigation, the simplified micro modelling finds an acceptable balance between the desired level of result accuracy and the required computational effort.
- It is observed that, in general, plane stress elements are used for the IP loading and solid elements for the OOP and/or combined loading. However, Alex and Menon (2017) showed that the simplified micro modelling with shell element is also able to capture the interaction between IP and OOP responses in URM walls under seismic loads. The main advantage of using shell element is the reduction in the computational time, as it contains fewer degrees of freedom and integration points than solid elements.

In the adopted simplified micro modelling approach, bricks are modelled with continuum shell elements and the mortar joints are modelled with zero-thickness interface elements. Tensile cracking of the bricks is also considered by introducing vertical line interface element in the middle of the brick. The constitutive behaviour of the interface elements is described by combined cracking-shearing-crushing (CCSC) interface model, that consists of Coulomb friction model with tension cut-off and a compression cap.

Addressing the second research sub-question, the validation process for the numerical modelling approach is performed in two steps. Initially, the mechanical properties of the numerical model are calibrated based on small-scale material tests. In the subsequent phase, the calibrated parameters are directly used in the numerical monotonic analyses of the full-scale walls, and the numerical outcomes are then compared to the test results. The model is validated against three IP tests and two OOP tests. The benchmark for calibrating and validating the numerical model is established through calcium silicate (CS) brick masonry tests conducted at the Delft University of Technology, from material to structural level. The main conclusions regarding the validation of the numerical model are presented below.

- An overall good agreement between the numerical results and the test results is obtained for the IP walls. The initial stiffness and the maximum shear force are close to the experimental results. Both during the tests and the numerical simulations, the shear dominated behaviour of the walls could be observed. However, the model showed its limitation to large displacements. For instance, the full response of the cantilever wall could not be achieved due to divergence in the analysis. This could be related to the crushing observed in the right bottom corner of the wall, both in the experiment and numerical simulation. Further, it could also be related to the tensile stresses close to failure at the brick interfaces.
- Contrary to the performance of the model for the IP walls, the results for the OOP walls are significantly overestimated, especially the peak strength with an average of 35% observable difference between the experimental and numerical results. This could be the effect of differences in boundary conditions (full or partial rotation restriction), type of test (cyclic or monotonic) and loading conditions (displacement control or load control) between numerical simulation and experimental tests. Nevertheless, the cracking patterns of the OOP walls were correctly estimated by the numerical model. It should be noted that the wall with opening showed brittle failure mechanism, while in the experiment ductile behaviour could be observed. The tensile stresses (close to failure) in the interfaces of the bricks caused brittle failure of the wall. However, the cracking of the bricks at the same location could also be observed in the experiment.

The validated model is applied for the numerical simulations of pre-damaged URM walls with and without opening. In answer to the third research sub-question, the study is performed considering four different states of pre-damage, from minor to extensive damage. For the solid wall (wall without opening), the damage levels are based on the damage observed during the IP tests with maximum drift of 0.2%. The damage levels for the wall with opening are based on damage observed from the numerical simulation with maximum drift of 0.14%. Two different approaches are adopted to simulate the response of the pre-damaged walls. In reduced- parameters approach, first a model is created with unequal properties: reduced values of stiffness and strengths where cracks are observed from IP tests, and regular properties in the other locations. Subsequently, the model is used to perform the OOP analyses. In sequential loading approach, first the wall is monotonically loaded in IP direction that represents the pre-damage of the wall. Then, the OOP load is applied while maintaining the IP pre-

deformation until the wall ultimately fails. Addressing to the last research sub-question, the main conclusions obtained from the simulations of the considered pre-damaged walls are presented below.

Solid wall:

- Both approaches showed almost negligible reduction in OOP strength for small pre-applied IP drifts, up to 0.057% drift.
- At 0.2% IP-drift, 40% reduction of the maximum OOP force was observed in reduced-parameters approach, while in sequential loading approach, the wall immediately failed showing negligible OOP strength because of the severe IP damage.
- In the sequential loading approach, as the level of pre-damage increased, the pre-peak stiffness of the force-displacement curve decreased, as expected for a pre-damaged wall. However, the reduced-parameters approach did not exhibit this reduction, which could be attributed to the pre-damage applied only at specific locations.
- There is no significant effect of pre-damage on the crack pattern of the wall. In both undamaged and pre-damaged walls, the well-known envelope crack pattern is obtained.

Wall with opening:

- Both approaches provided similar response in terms of maximum OOP force reduction due to IP pre-damages. The maximum reduction that could be observed is approximately 15% at maximum of 0.14% pre-applied IP drift.
- The sequential loading approach resulted in brittle failure of the pre-damaged wall for each damage state because of the failure in the bricks. The tensile stresses at the interfaces in the bricks were close to failure that caused divergence. However, this issue was not visible in the reduced-parameter approach and the post-peak could be achieved. This could be attributed to the pre-defined weakened interfaces that effectively prevented stress concentration in the brick interfaces, resulting in a stable response.
- Contrary to reduced-parameters approach, the sequential loading approach showed reduction of the pre-peak stiffness with an increasing level of damage.
- Due to the premature failure of the wall, a complete crack pattern could not be achieved with the sequential loading approach. However, using the reduced-parameters approach, a crack pattern similar to the one observed in the experiment (undamaged wall) could be achieved. This crack pattern consisted of two horizontal cracks at the top and bottom mortar layers of the wall, two diagonal cracks connected by multiple horizontal cracks in the middle of the left pier, and diagonal cracks in the right corners of the opening.

The general conclusions of this thesis work with respect to the main research question are:

- The OOP capacity of URM walls is significantly affected by the presence of in-plane damages. It is observed that under severe in-plane damages (0.2% pre-applied IP drift) the OOP capacity of the wall could reduce by 40 to 100% of its undamaged capacity. However, for light damages (below 0.06% pre-applied IP drift) the effect of pre-damage is almost negligible (below 5%).
- The effect of pre-damage becomes more pronounced as the in-plane damage increases.
- The pre-damage does not have a significant impact on the failure pattern of the wall when compared to an undamaged wall.

7.2 Recommendations for future research

- There is no evidence of any experimental tests on the OOP capacity of pre-damaged URM walls. Hence, it is recommended to carry out tests in order to verify numerical studies performed on this topic, including this report.
- The numerical model predicted good results for the IP response of the wall. However, for the OOP analysis, there was a considerable difference in the numerical and experimental peak force. This could be further verified by comparing the results with other available OOP tests on masonry walls.
- It is suggested to extend this study by considering different boundary conditions for the OOP loading. For instance, a wall that is simply supported on three sides or four sides in the OOP direction.
- Research on this topic could be extended to walls subjected to one-way bending OOP failure, since they are more susceptible to the OOP loading.
- This thesis limits the numerical analyses to monotonic loading. For future research, it is of interest to perform the analyses under cyclic or even dynamic load, since they better represent the reality of seismic loading.
- Considering other types of pre-damage such as damage due to settlement of the building could be of interest in the research of OOP analysis of the walls.
- Comparison study can be performed with different modelling strategies such as macro modelling and detailed micro modelling.

References

Agnihotri, Pawan & Singhal, Vaibhav & Rai, Durgesh. (2013). Effect of in-plane damage on out-of-plane strength of unreinforced masonry walls. Engineering Structures. 57. 1–11. 10.1016/j.engstruct.2013.09.004.

Alejo, L., Mendes, N., & Lourenco, P. (2017). The effect of morphology on the structural behaviour of masonry walls. Espana: Congreso de Metodos Numericos en Ingenieria.

Alex, Jacob & Menon, Arun. (2017). Interaction of In-Plane and Out-of-Plane Responses in Unreinforced Masonry Walls under Seismic Loads. Journal of Structural Engineering (Madras). 44.

Atkinson, R.H., Amadel, B.P., Saeb, S. and Sture, S. (1989) - Response of masonry bed joints in direct shear. J. Struc. Engrg., ASCE, 115(9) , p. 2276-2296.

Backes, H.P. (1985). On the behaviour of masonry under tension in the direction of the bed joints (in German). Dissertation, Aachen University of Technology, Aachen, Germany.

Binda, L., Fontana, A. and Frigerio, G. (1988) - Mechanical behavior of brick masonries derived from unit and mortar characteristics, in: Proc. 8th Int. Brick and Block Masonry Conf., eds. J.W. de Courcy, Elsevier Applied Science, London, UK, p. 205-216.

Chang, L., Rots, J. G., & Esposito, R. (2022). Influence of openings on two-way bending capacity of unreinforced masonry walls. Journal of Building Engineering, 51, [104222].

Chang, L. (2022). Parametric numerical study on two-way bending capacity of unreinforced masonry walls. PhD thesis, Delft University of Technology.

D'Altri, A. M., de Miranda, S., Castellazzi, G., & Sarhosis, V. (2018). A 3D detailed micro-model for the in-plane and out-of-plane numerical analysis of masonry panels. Computers & Structures, 206, 18-30.

D'Altri, A. M., Messali, F., Rots, J., Castellazzi, G., & de Miranda, S. (2019). A damaging block-based model for the analysis of the cyclic behaviour of full-scale masonry structures. Engineering Fracture Mechanics, 209, 423-448.

D'Altri, A. M., Sarhosis, V., Milani, G., Rots, J., Cattari, S., Lagomarsino, S., Sacco, E., Tralli, A., Castellazzi, G., & de Miranda, S. (2019). Modeling Strategies for the Computational Analysis of Unreinforced Masonry Structures: Review and Classification. Archives of Computational Methods in Engineering, 27(4), 1153-1185

D'Ayala, D., & Speranza, E. (2003). Definition of collapse mechanisms and seismic vulnerability of historic masonry buildings. Earthquake Spectra 19(3): 479-509.

Dhanasekar, M., Page, A.W. and Kleeman, P.W. (1985). The failure of brick masonry under biaxial stresses. Proc. Intsn. Civ. Engrs., Part 2, 79, p. 295-313.

DIANA FEA BV. (2021). DIANA user's manual - Release 10.5. Delft, The Netherlands.

Dizhur, Dmytro & Dhakal, Rajesh & Bothara, Jitendra & Ingham, Jason. (2016). Building typologies and failure modes observed in the 2015 Gorkha (Nepal) earthquake. Bulletin of the New Zealand Society for Earthquake Engineering. 49. 211-232.

Dolatshahi, Kiarash & Aref, Amjad & Yekrangnia, Mohammad. (2014). Bidirectional behavior of unreinforced masonry walls. Earthquake Engineering & Structural Dynamics. 43. 10.1002/eqe.2455.

Dolatshahi, Kiarash & Yekrangnia, Mohammad. (2015). Out-of-Plane Strength Reduction of Unreinforced Masonry Walls Due to In-plane Damages. Earthquake Engineering & Structural Dynamics. 10.1002/eqe.2574.

Dolatshahi, K. M., Aref, A. J., and Whittaker, A. S. (2015). “Interaction curves for in-plane and out-of-plane behaviors of URM walls.” J. Earthquake Eng., 19(1), 60–84. Lourenco, Paulo & Rots, Jan. (1997). Multisurface Interface Model for Analysis of Masonry Structures. Journal of Engineering Mechanics. 123. 660-668. 10.1061/(ASCE)0733-9399(1997)123:7(660).

Esposito, R., Messali, F. & Rots, J. (2016). Tests for the characterization of replicated masonry and wall ties. Delft University of Technology.

Esposito, R. & Ravenshorst, G. (2017). Quasi-static cyclic in-plane tests on masonry components 2016/ 2017. Delft University of Technology.

Esposito, R. (2019). CIE5148 Lecture 9 - Seismic Analysis. Computational Modelling of Structures. Delft University of Technology.

Esposito, Rita & Messali, Francesco & Ravenshorst, Geert & Schipper, Roel & Rots, Jan. (2019). Seismic assessment of a lab-tested two-storey unreinforced masonry Dutch terraced house. Bulletin of Earthquake Engineering. 17. 10.1007/s10518-019-00572-w.

Graziotti, F., Tomassetti, U., Sharma, S., Grottoli, L., & Magenes, G. (2019). Experimental response of URM single leaf and cavity walls in out-of-plane two-way bending generated by seismic excitation. Construction and Building Materials, 195, 650-670.

Hoffmann, G. and Schubert, P. (1994). Compressive strength of masonry parallel to the bed joints. in: Proc. 10th Int. Brick and Block Masonry Conf., eds. N.G. Shrive and A. Huizer, University of Calgary, Calgary, Alberta, Canada, p. 1453-1462.

Jafari, S. & Esposito, R. (2016). Material tests for the characterisation of replicated calcium silicate brick masonry. Delft University of Technology.

Jafari, S. (2021). Material characterisation of existing masonry: A strategy to determine strength, stiffness and toughness properties for structural analysis. PhD thesis, Delft University of Technology.

Kaiser, Anna & Francois-Holden, Caroline & Beavan, J & Beetham, D & Benites, Rafael & Celentano, A & Collett, D & Cousins, J & Cubrinovski, Misko & Dellow, G.D. & Denys, Paul & Fielding, Eric & Fry, Bill & MC, Gerstenberger & Langridge, Rob & CI, Massey & Motagh, Mahdi & Pondard, Nicolas & Mcverry, Graeme & JX, Zhao. (2012). The Mw 6.2 Christchurch earthquake of February 2011: Preliminary report. New Zealand Journal of Geology and Geophysics. 55. 67-90. 10.1080/00288306.2011.641182.

Karimi Ghaleh Jough, F., & Golhashem, M. (2020). Assessment of out-of-plane behavior of non-structural masonry walls using FE simulations. Bulletin of Earthquake Engineering, 18(14), 6405-6427.

Korswagen Eguren, P., Longo, M., Meulman, E., & Rots, J. (2019). Experimental and computational study of the influence of pre-damage patterns in unreinforced masonry crack propagation due to induced, repeated earthquakes. In P. B. Dillon, & F. S. Fonseca (Eds.), Proceedings of the Thirteenth North American Masonry Conference : June 16-19, 2019, Salt Lake City, UT, USA (pp. 1628-1645). TMS.

Lawrence, S. J. (1983). Behavior of brick masonry walls under lateral loading (Publication Number 1) (PhD thesis), University of New South Wales. Sydney, Australia.

Lee, K.H. (2022). A comparison study of numerical modeling approaches for simulating the in-plane seismic response of masonry walls. MSc thesis, Delft University of Technology.

Lourenco, Paulo. (1996). Computational Strategy for Masonry Structures. Delft University of Technology.

Najafgholipour, M., Maheri, M. R., and Lourenço, P. B. (2013). "Capacity interaction in brick masonry under simultaneous in-plane and out-of-plane loads." Constr. Build. Mater., 38, 619–626.

Najafgholipour, Mohammadamir & Maheri, Mahmoud & Lourenco, Paulo. (2014). Definition of interaction curves for the in-plane and out-of-plane capacity in brick masonry walls. Construction and Building Materials. 55. 168–182. 10.1016/j.conbuildmat.2014.01.028.

Najafgholipour, M. (2018). An Equivalent Truss Model for In-Plane Nonlinear Analysis of Unreinforced Masonry Walls. Civil Engineering Journal. 4. 828. 10.28991/cej-0309136.

Noor-E-Khuda, Sarkar & Dhanasekar, Manicka. (2018). Masonry Walls under Combined In-Plane and Out-of-Plane Loadings. Journal of Structural Engineering. 144. 10.1061/(ASCE)ST.1943-541X.0001930.

Noor-E-Khuda, Sarkar & Dhanasekar, Manicka. (2018). Three sides supported unreinforced masonry walls under multi-directional loading. Construction and Building Materials, Volume 188, Pages 1207-1220. ISSN 0950-0618.

Oliveira D.V. & Lourenço, P.B. (2004). Implementation and validation of a constitutive model for the cyclic behaviour of interface elements. Computers & Structures, Volume 82, Issues 17–19, Pages 1451-1461, ISSN 0045-7949.

Oyguc, Resat & Oyguc, Evrim. (2017). The 2011 Van Earthquakes: Lessons from Damaged Masonry Structures. Journal of Performance of Constructed Facilities. 31. 10.1061/(ASCE)CF.1943-5509.0001057.

Padalu, P. K. V. R., Singh, Y., & Das, S. (2020b). Cyclic two-way out-of-plane testing of unreinforced masonry walls retrofitted using composite materials. Construction and Building Materials, 238.

Patel, K. & Dubey, R. (2022). Effect of flanges on the in-plane behavior of the masonry walls. Engineering Structures, Volume 273. 115059. ISSN 0141-0296.

Penna, A., Morandi, P., Rota, M., Manzini, C. F., da Porto, F., & Magenes, G. (2014). Performance of masonry buildings during the Emilia 2012 earthquake. Bulletin of Earthquake Engineering, 12(5), 2255-2273.

Pluijm, R. Van der (1992) - Material properties of masonry and its components under tension and shear, in: Proc. 6th Canadian Masonry Symposium, eds. V.V. Neis, Saskatoon, Saskatchewan, Canada, p. 675-686.

Pluijm, R. Van der (1993) - Shear behavior of bed joints, in: Proc. 6th North American Masonry Conf., eds. A.A. Hamid and H.G. Harris, Drexel University, Philadelphia, Pennsylvania, USA, p. 125-136.

Ravenshorst, G. J. P., & Messali, F. (2016a). In-plane tests on replicated masonry walls. Delft University of Technology.

Ravenshorst, G. J. P., Messali, F. (2016b). Out-of-plane tests on replicated masonry walls. Report No. C31B60-6, 30 May 2016. Delft University of Technology.

Sacco E., Addessi D., Sab K. (2018). New trends in mechanics of masonry. Meccanica 53(7):1565–1569.

SAHC (2019). Investigation on the strength of spandrels in masonry façades. University of Minho, Portugal.

Schubert, P. (1988a) - The influence of mortar on the strength of masonry, in: Proc. 8th Int. Brick and Block Masonry Conf., eds. J.W. de Courcy, Elsevier Applied Science, London, UK, p. 162-174.

Shell (2016). Measuring the impact of earthquakes in Groningen. Shell Sustainability Report 2016.

Staatstoezicht op de Mijnen (2022). Jaarverslag SodM 2021. Ministerie van Economische Zaken en Klimaat.

Vaculik, J. (2012). Unreinforced masonry walls subject to out-of-plane seismic actions. PhD Thesis, The University of Adelaide, Adelaide (AU).

Yi, W., Oh, S. & Lee, J. (2004). Shear Capacity Assessment of Unreinforced Masonry Wall. 13th World Conference on Earthquake Engineering. Vancouver, B.C., Canada. Paper No. 1698.